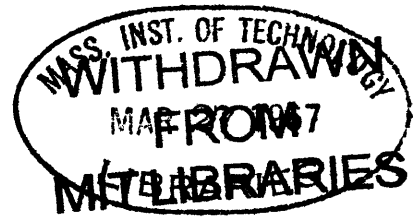


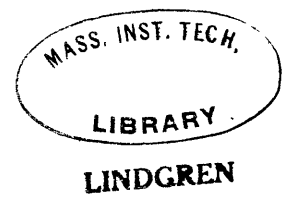
D



AN EXPERIMENTAL STUDY OF AXISYMMETRIC INERTIAL OSCILLATIONS  
OF A ROTATING LIQUID SPHERE

by

Keith D. Aldridge  
B.A.Sc., University of Toronto  
(1962)



SUBMITTED IN PARTIAL FULFILLMENT  
OF THE REQUIREMENTS FOR THE  
DEGREE OF DOCTOR OF  
PHILOSOPHY  
at the  
MASSACHUSETTS INSTITUTE OF  
TECHNOLOGY  
January 1967

Signature of Author \_\_\_\_\_  
Department of Geology, and Geophysics

Certified by \_\_\_\_\_ Thesis Supervisor

Accepted by \_\_\_\_\_  
Chairman, Departmental Committee  
on Graduate Students  
*Clay Mencher*

11/11/11

11/11/11

Problems worthy  
of attack  
Prove their worth  
by hitting back.

--Piet Hein,  
Grooks.

-

1

-

-

-

-

## TABLE OF CONTENTS

	<u>Page</u>
Preface	i
Abstract	iii
List of figures	v
List of tables	vii
List of plates	viii
Range of parameters covered by experiments	ix
I      Introduction	1
II     Modes of the sphere	6
III    Modes of spherical shells	63
IV     Discussion of errors	79
V      Summary	83
VI     Apparatus and methods	86
References	106
Appendices	
I      Polynomial representation of the stream function.	108
II     Response at resonance for the sphere.	111
III    Superposition of modes - an analogy.	118
IV     Variational formulation of the eigenvalue problem.	121
Biographical Note	128

-

1

-

-

-

-

PREFACE

This work began as an experiment, suggested by Alar Toomre, to excite inertial oscillations in a rotating sphere of fluid by means of Ekman suction. The results of initial experiments were presented by the author at the oral part of his general examination. These first experiments were successful but unsatisfying because there were some significant departures of the results from linear theory. This thesis is the report of a more precise investigation designed to measure these non-linear effects and extend the work to spherical shells of fluid.

Professor Toomre has provided most of the theory for the sphere. References to these contributions appear throughout the text.

Extension of the work to spherical shells of fluid was suggested by Professor Raymond Hide; the analysis associated with these experiments is the work of the author.

Although the experimental results have not yet been published, the amplitude spectrum (figure 3a of this report) has appeared in a review article of the I.U.T.A.M. symposium on rotating fluid systems which took place in April 1966 (J.F.M., 26, part 2, p. 406). A joint paper by the author and Alar Toomre entitled "Axisymmetric inertial oscillations of a rotating sphere of fluid" is about to be submitted to the Journal of Fluid Mechanics.

I am indebted to Professor Alar Toomre for suggesting this experiment and continuing to assist me in his ebullient manner.

I wish to thank Professor Raymond Hide for his patience in supporting this prolonged experiment and providing me with full use of the facilities of the Geophysical Fluid Dynamics Laboratory.

I am grateful to Professor A. F. Gangi for several helpful and invariably lively discussions.

I wish to thank Dr. H. T. Rossby for providing the power spectrum program and assisting me with the data conversions for its operation.

For the construction of the apparatus, which was actually built several times during its evolution from a complex design to a simple one, I am grateful to Mr. T. Cieri and Mr. K. Harper. I also wish to thank Mr. J. Burke and Mr. B. Gray for many valuable suggestions and aid in the building of this apparatus.

For typing the attractive final draft of this thesis, I am grateful to Mrs. P. Zahler and Miss L. Hebach.

Machine calculations of this report have been carried out on the I.B.M. 7094 of the M.I.T. Computation Center.



ABSTRACT

Certain axisymmetric inertial eigen-oscillations of an almost uniformly rotating fluid within a rigid spherical cavity were investigated experimentally. These modes were excited through a periodic, small-amplitude variation of the rotation speed of the container; the small viscosity of the fluid served to communicate this reciprocating container motion to the essentially inviscid interior through the slight pumping action of the oscillating, latitude-dependent Ekman boundary layer formed at the interface.

The response of the fluid, as determined with a pressure transducer and also visually, was found to be characterized by a spectrum of resonance peaks, each situated well within one percent of the corresponding critical ratio of the excitation to the mean rotation frequency predicted by linear theory. Somewhat less favorable theoretical comparisons were also made of the response amplitudes at these resonances, and of the rates of decay of certain of the modes upon switching off the excitation.

Several non-linear effects were observed at larger variations of rotation speed. Among these were a rectified zonal current, a boundary layer roll instability and an overshoot of the steady state response which occurred when the container oscillation was "turned on."

Amplitude spectra were obtained for various spherical shells of fluid and the critical frequency ratios for these modes were predicted from a variational formulation of the eigenvalue problem.

FIGURES

<u>Number</u>		<u>Page</u>
1	Nodal surfaces for (4,3) mode	14
2	Summary of modes	16
3a	Amplitude response of the sphere; $z=0; \epsilon=8.0^\circ$	20
4a	Phase response of the sphere; $z=0; \epsilon=8.0^\circ$	22
5	Complex amplitude response of the sphere; $z=0; \epsilon=8.0^\circ$	24
3b	Superposition of modes; amplitude response	28
4b	Superposition of modes; phase response	30
6	Amplitude response of the sphere; $z=0.5a; \epsilon=8.0^\circ$	34
7	Fine structure of the (1,1) and (3,2) peak; $z=0.5a; \epsilon=8.0^\circ$	36
8	Pressure profile; (1,1) mode; $z=0; \epsilon=8.1^\circ$	38
9	Zonal current; (1,1) mode.	40
10	Resonance "shift"; (1,1) mode	42
11	Response at resonance; (1,1) mode	44
12	Time histories; (1,1) mode	46
13	Power density spectra; (1,1) mode; $z=0; \epsilon=20.3^\circ$	48
14	Decay at resonance; (1,1) mode; $z=0; \epsilon=8.0^\circ$	50
15	Decay at resonance; multiple mass-spring oscillator	52
16	Boundary layer roll structure; (1,1) mode	64
17	Amplitude response of the spherical shell; $b/a=0.25; z=0.26a; \epsilon=8.0^\circ$	66
18	Amplitude response of the spherical shell; $b/a=0.35; z=0.36a; \epsilon=7.9^\circ$	68

<u>Number</u>		<u>Page</u>
19	Amplitude response of the spherical shell; $b/a=0.51$ ; $z=0.53a$ , $\epsilon=7.9^\circ$	70
20	Oscillating sphere	88
21	Oscillator linkage	90
22	Calibration schematic	98
23	Amplitude and phase calibration	100
24	Probe effect	102

TABLES

<u>Number</u>		<u>Page</u>
1	Summary of results at resonance for the sphere; $\kappa=0$ ; $\epsilon = \beta \cdot 0^\circ$	26
2	Superpositon of modes.	32
3	Decay rates and Q's for (1,1), (2,1), (3,1) and (4,1) modes.	54
4	Experimental modal frequency ratios; sphere and spherical shells.	72
5	Modal frequency ratios for the sphere from variational principle.	74
6	Modal frequency ratios for the spherical shell $b/a=0.51$ from the variational principle and experiments.	76

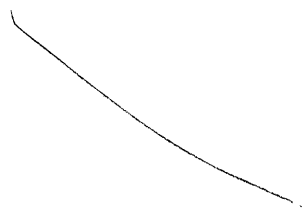
PLATES

<u>Number</u>		<u>Page</u>
1	Secondary flow; (1,1) mode; $\epsilon = 8.0^\circ$ ; $\epsilon = 11.3^\circ$	56
2	Secondary flow; (1,1) mode; $\epsilon = 14.0^\circ$	58
3	Large amplitude response; (1,1) mode; $\epsilon = 22.2^\circ$	60
4	Boundary layer rolls; (1,1) mode; $\epsilon = 14.8^\circ$	62
5	Secondary flow for spherical shell, $b/a=0.51$ ; "(2,2)" mode; $\epsilon = 14.0^\circ$ .	78

RANGE OF PARAMETERS COVERED BY EXPERIMENTS

<u>Parameter</u>	<u>Range</u>
Sphere radius, a	a=10cm.
Inner sphere radius, b	b=2.5, 3.5, 5.1cm.
Rotation speed, $\Omega$	$1/2 < \Omega/2\pi < 2$ cps
Oscillation frequency, $\omega$	$\omega/2\pi = 1$ cps
Oscillation frequency / 2. rotation speed	$1/4 < \omega/2\Omega < 1$
Half-amplitude of oscillation, $\epsilon$ (degrees)	$2^\circ < \epsilon < 22^\circ$
Quantitative work	$2^\circ < \epsilon < 14^\circ$
Qualitative work	$5^\circ < \epsilon < 22^\circ$
Kinematic viscosity, $\nu$	1cs, 5cs
Axial location of pressure probe, $z/a$	$-1 < z/a < 1$
Sphere (spectra)	$z/a=0, 0.5$
Sphere (profile)	$z/a=-0.9, -0.8, \dots, 0..$ $\dots, 0.8, 0.9$
Spherical shell (spectra)	$z/a=0.26, 0.36, 0.53$

6.28  
10<sup>4</sup> 22







CHAPTER I

Introduction

Studies of the oscillations of a rotating fluid naturally separate into two categories depending on whether or not the vertical (direction of  $g$ ) component of coriolis force is retained. This separation is determined by the ratio of the Brunt-Vaisala frequency  $N$ , to the inertia frequency  $2\Omega$ . The Brunt Vaisala frequency is proportional to the difference between the adiabatic and true density gradients in the vertical direction (Eckart, 1960) and hence is a measure of the restoring force per unit mass or stiffness of the fluid for vertical displacements. If  $N/2\Omega \gg 1$ , as would be the case in a relatively strongly stratified fluid, motions would be essentially two dimensional in the plane of the stratification. If  $N/2\Omega \ll 1$ , as for a weakly stratified or unstratified fluid, coriolis acceleration in the vertical direction must be retained, and the flow will, in general, be three dimensional.

In both categories, in this discussion, we limit ourselves to those cases where the only effects of density variations are in the bouyancy terms so that dynamically the fluid behaves as though the density were constant. Most of the analysis of tidal and atmospheric oscillations has assumed essentially two dimensional flow and a brief summary of this work will be given first. The development of interest in the somewhat more general case of relatively weak stratification, which is directly concerned with

the experiments discussed here since the density of the working fluid was constant, will be given second.

1.1  $N/2\Omega \gg 1$ ; "Strong" stratification.

In most places in the oceans and atmosphere the Brunt-Vaisala frequency does dominate the inertia frequency, and the analysis is essentially a two dimensional one in planes tangent to the spherical surface.

Many have made use of this fact in dealing with modes of oscillation of the oceans, Laplace's dynamical theory of the tides forming a classical example. Hough (1898) showed that the tidal oscillations naturally divide into two classes, as given by their period as the earth's rotation period is increased without limit. Class 1 oscillations tend to gravity waves; class 2 oscillations approach steady currents. More recently, Rossby (1939) found the fundamental features of a wave disturbance in a thin sheet (in this case the atmosphere) by retaining only the dynamical effects of the curvature of the earth's surface in the equations of motion. This so-called  $\beta$  plane, approximation greatly simplified the mathematical analysis and it has been subsequently used by many meteorologists and oceanographers. For example, Arons and Stommel (1956), in such a  $\beta$  plane analysis for the oceans, identified the waves Rossby found, called planetary waves, with the Laplace tidal oscillations of the second class. Longuet-Higgins (1965) has compared results of his full

treatment of curvature effects on planetary waves in a hemispherical basin with the  $\beta$  plane solution and found favorable agreement with the spatially simple modes. Thus, the  $\beta$  plane approximation, is quite reliable in its simplification of the equations of motion for two dimensional flow in the horizontal plane.

1.2.  $N/2\Omega \ll 1$ ; "Weak" stratification

We consider here the background of that class of oscillations of a uniform fluid in which both horizontal and vertical coriolis accelerations are important. The motion in shells of fluid are thought of here as a special case of the general class of oscillations of a body of fluid (a sphere).

Oscillations of this type were known to Kelvin (1880). He has given explicitly the modes for a right circular cylinder of fluid and described an experiment to excite axisymmetric modes in a rotating flask of water with an axial plunger and disk arrangement. The oscillations of a rotating mass of fluid were studied by Poincaré (1885). Cartan, a student of Poincaré, found (1922) that each mode could be expressed as a series of polynomials which always truncates.

Bjerknes (1933) has discussed, in considerable detail, what he calls elastoid-inertial oscillations of a rotating fluid. He has used the term elastoid to express the "elastic like" restoring force experienced by an axis-centered fluid ring which changes its radius while maintaining its circulation around its circumference constant, in consequence of Helmholtz' circulation

theorem. This process is, in fact, the underlying one to the oscillations studied in the present experiments.

Bjerknes (1933) has also given a physical interpretation of the periods of these elastoid-inertia oscillations for the axisymmetric case of a fluid between concentric cylinders, which is rotating around the common centre axis. He finds that the oscillation period  $T$  can be expressed in terms of the rotation period  $T_0$  and the ratio,  $L_c/L_a$ , of the breadth to the depth of an oscillation cell, as

$$T = T_0 \left[ 1 + (L_c/L_a)^2 \right]^{1/2} .$$

Since the elastoid restoring force is determined by the radial displacements, the very flat deep cells will experience this force the most and will have correspondingly short periods in contrast to the broad shallow cells which hardly experience it at all and hence have very long periods. If, then, we seek, as Bjerknes suggests, diurnal oscillations of this type in a uniform ocean, we find that  $L_c = \sqrt{3} L_a$ . For an ocean of mean depth 5 km, the extent in latitude of this axisymmetric cell will be 8.7 km. On an oceanic scale of 3000km this is a very localized disturbance; the conclusion is, therefore, that we can only expect to find diurnal oscillations of this type on a limited horizontal scale. He points out, however, that the length scale restriction is removed in the earth's core so that

oscillations of diurnal period are possible in a uniform core. Hide (1966) has discussed the "uniformity" of the core. He argues that even if the core is isothermal, the Brunt-Vaisala frequency associated with the estimated core adiabatic temperature gradient is much less than the inertia frequency, so that the core should behave as a uniform fluid, if we ignore the complication of strong magnetic fields.

The results of laboratory experiments on inertial oscillations were first reported by Fultz (1960). Several of the axisymmetric modes of a right circular cylinder were excited with an axial plunger, which could be made to oscillate at various frequencies. The experiments reported here extend the work of Fultz to a spherical geometry. In addition, here, modes are excited by a viscous stress applied to the boundary of the fluid. The details of the spatial structure of the inviscid modes and the excitation of their viscous counterparts are given in the next chapter.

CHAPTER II

Modes of the Sphere

<u>Section</u>		<u>Page</u>
2.1	Inviscid inertial modes of a sphere	6
2.2	Excitation of inertial modes	13
2.3	Response of the sphere; $Z = 0$	19
	2.3.1 Amplitude spectrum	
	2.3.2 Phase spectrum	
	2.3.3 Complex amplitude	
	2.3.4 Summary of spectral results	
2.4	Superposition of modes	25
2.5	Response of the sphere; $Z = 0.5a$	33
2.6	Details of the $(1,1)$ mode	35
	2.6.1 Pressure profile	
	2.6.2 Zonal current	
	2.6.3 Resonance shift	
	2.6.4 Response at resonance	
	2.6.5 Large amplitude results	
2.7	Transient response of the sphere	47
	2.7.1 Decay at resonance	
	2.7.2 Summary of decay rates and Q's for the sphere.	
2.8	Visual studies	53
	2.8.1 Interior regions	
	2.8.2 Boundary layers	

2.1 Inviscid inertial modes of a sphere.

Before developing the complete solution for the inviscid modes in a uniformly rotating fluid, we shall consider a simple

fluid ring model which displays the physics of these fluid oscillations. Imagine an axis-centred fluid ring in a fluid rotating with uniform rotation speed  $\Omega$  radians/second. The ring is in dynamical equilibrium because the centrifugal force exactly balances the radial pressure gradient. The centrifugal force per unit mass on a fluid ring of radius,  $r_1$ , is, in fact,  $\Omega^2 r_1$ .

If now we increase, say, the radius of the ring to  $r_2$  the absolute rotation speed of the ring must decrease in order to conserve angular momentum as given by Kelvin's circulation Theorem,

$$\frac{d}{dt} \oint v \cdot dl = 0,$$

where  $dl$  is an element of fluid ring and  $d/dt$  is the total derivative. The new absolute rotation speed of the ring is then

$$\Omega^* = (r_1 / r_2)^2 \Omega.$$

The net restoring force/unit mass,  $F$ , on the ring at the new radius  $r_2$  is the difference between the local pressure gradient at  $r_2$  and the centrifugal force on this ring with rotation speed  $\Omega^*$ . We let  $r_2 = r_1 + \Delta r$  and

$$F = \Omega^2 (r_1 + \Delta r) - \Omega^{*2} (r_1 + \Delta r)$$

$$F = \Omega^2(r_1 + \Delta r) - \Omega^2 r_1 \left(1 - 3 \frac{\Delta r}{r_1} + 6 \left(\frac{\Delta r}{r_1}\right)^2 - \dots\right)$$
$$= 4\Omega^2 \Delta r, \text{ ignoring higher order terms in } \Delta r.$$

Then the equation of motion of this simple oscillator is

$$\ddot{\Delta r} + 4\Omega^2 \Delta r = 0.$$

Elementary solutions of this equation are proportional to

$\text{Re}\{e^{i\omega t}\}$  where

$$\omega = 2\Omega.$$

In assuming, therefore, that all the fluid motion takes place in planes perpendicular to the axis of rotation, so that the restoring force due to the rotation has its maximum effect, we find an upper frequency limit for the inertial modes. Fluid motions parallel to the axis of rotation do not sense the restoring force at all and would, therefore, represent the lower frequency limit of zero for the inertial modes. For intermediate frequencies we expect that modes would be ordered from 0 to  $2\Omega$  in increasing proportion of some measure of the radial to vertical motion.



The structure and frequency ratios,  $\omega/2\Omega$ , for the inviscid modes of the sphere are obtained in the following manner. Since the flow has axial symmetry, it is natural to express the linearized inviscid momentum equations

$$\frac{\partial \bar{u}}{\partial t} + 2\bar{\Omega} \times \bar{u} = -\frac{1}{\rho} \bar{\nabla} P, \quad 2.1$$

which describe the fluid motion relative to the rotating frame of reference,  $\bar{\Omega}$ , in cylindrical coordinates  $(r, \phi, z)$ . The velocity  $\bar{u}$  has components  $(u, v, w)$  and the rotational velocity  $\bar{\Omega}$  is  $(0, 0, \Omega)$ ;  $\rho$  is the density and the pressure  $P$  includes the centrifugal and gravitational potentials.

In component form the momentum equations are:

$$\begin{aligned} \frac{\partial u}{\partial t} - 2\Omega v &= -\frac{1}{\rho} \frac{\partial P}{\partial r}, \\ \frac{\partial v}{\partial t} + 2\Omega u &= 0, \\ \frac{\partial w}{\partial t} &= -\frac{1}{\rho} \frac{\partial P}{\partial z}. \end{aligned} \quad 2.2$$

The continuity equation for axisymmetric flow,

$$\frac{1}{r} \frac{\partial}{\partial r} (ru) + \frac{\partial w}{\partial z} = 0, \quad 2.3$$

is satisfied by defining a stream function  $\psi$  as follows:

$$u(R, z) = \frac{1}{R} \frac{\partial \psi}{\partial z}$$

2.4

$$W(R, z) = -\frac{1}{R} \frac{\partial \psi}{\partial R}$$

where  $R=r/a$ ;  $z=z/a$  and the dimensionless velocities  $U, W$  are given by

$$(u, v, w) = \epsilon \omega_{nm} a \operatorname{Re} \left\{ C_{nm} e^{i\omega_{nm} t} \left( iU, -\frac{2R}{\omega_{nm}} U, iW \right) \right\}$$

2.5

where  $\epsilon \omega_{nm} a$  is the peak perturbation velocity of the container at the equator and  $C_{nm} = M + iN$ , a complex constant.

Elimination of the pressure terms of the momentum equations, 2.2, in conjunction with the above definitions of  $\psi$ , leads to the differential equation

$$R \frac{\partial}{\partial R} \left( \frac{1}{R} \frac{\partial \psi}{\partial R} \right) - \lambda^2 \frac{\partial^2 \psi}{\partial z^2} = 0,$$

2.6

where

$$\lambda^2 = \frac{4J_2^2}{\omega_{nm}^2} - 1,$$

and the boundary condition

$$\psi = 0 \quad \text{on} \quad R^2 + z^2 = 1.$$

2.7

Although the equation 2.6 for the stream function  $\psi$  does not

separate, the substitution

$$\psi = R \Phi$$

gives

$$\frac{\partial^2 \Phi}{\partial R^2} + \frac{1}{R} \frac{\partial \Phi}{\partial R} - \frac{\Phi}{R^2} - \lambda^2 \frac{\partial^2 \Phi}{\partial z^2} = 0, \quad 2.8$$

which is Laplace's equation for an azimuthal dependence  $e^{i\phi}$  and a stretched  $\bar{z}$  coordinate. A convenient coordinate system, (compatible with the boundary condition, 2.7), in which Laplace's equation separates has been given by Greenspan (1964). He defines a coordinate transformation

$$R = \left( \frac{1}{1 - X_m^2} - \eta^2 \right)^{1/2} (1 - \mu^2)^{1/2} \quad 2.9$$

$$\bar{z} = \left( \frac{1}{X_m^2} - 1 \right)^{1/2} \eta \mu$$

where  $X_m = \omega/2R$ .

Elimination of either  $\eta$  or  $\mu$  from the transformation defined by 2.9 shows that curves of constant  $\eta$  (or  $\mu$ ) are ellipses in the  $(R, \bar{z})$  coordinates. In particular  $\eta_0 = \sqrt{X_m^2/1 - X_m^2}$ ,  $\mu = \cos \theta$  ( $\theta$  is the polar angle) define a circle in the  $(R, \bar{z})$  plane.

In terms of the  $(\eta, \mu)$  coordinates the solutions to equation 2.8 are proportional to

$$\Phi(\eta, \mu) = P_{2n+2}^{(1)}[(1-x_m^2)^{1/2}\eta] P_{2n+2}^{(1)}[\mu] \quad 2.10$$

where  $P_{2n+2}^{(1)}(\cdot)$  is the associated legendre function of the first kind. Since  $\Phi(\eta_0, \mu) = 0$ , the eigen values are given by

$$P_{2n+2}^{(1)}(x_m) = 0.$$

Each polynomial  $P_{2n+2}^{(1)}(x)$  has  $n$  roots for  $(0 < x < 1)$ . For each  $n$  there exists a family of  $n$  modes; the mode number  $m$  within a family ( $1 \leq m \leq n$ ) labels the roots,  $\omega/2\Omega$ , in order of increasing frequency  $\omega$  for a given value of  $2\Omega$ . Each mode has the unique subscript  $(n, m)$ .

Since  $\psi = R\Phi$ , the stream function  $\psi$  may be written

$$\psi_{nm}(\eta, \mu) = \left(\frac{1-x_m^2}{1-x_k^2} - \eta^2\right)^{1/2} (1-\mu^2)^{1/2} \Phi_{nm}(\eta, \mu) \quad 2.10a$$

A convenient representation in terms of the somewhat more useful  $(R, z)$  coordinates, derived from the above expression,\* (Appendix I), is

$$\psi_{nm}(R, z) = R^2 z \prod_{k=1}^n \left[ 1 - \frac{x_m^2}{x_k^2} z^2 - \frac{1-x_m^2}{1-x_k^2} R^2 \right].$$

This product form is convenient for constructing the stream function; the meridional plane traces of the nodal surfaces for  $\psi_{43}(R, z)$  are shown in Figure 1. Stream lines for the first 4 families of modes are shown in Figure 2. Since for any family, modes are ordered with increasing frequency from left to right,

---

\*This derivation is essentially one given earlier by Toomre when the author suggested that the traces of nodal surfaces might be ellipses.

we see that it is true, as suggested earlier in this chapter, that the higher the frequency the greater the proportion of radial motion. The limiting case of  $\omega \rightarrow 2\Omega$ , given at the beginning of this chapter, corresponds to very flat cells with almost no vertical motion. Similarly the case of  $\omega \rightarrow 0$  corresponds to tall narrow cells with almost no radial motion.

This completes the discussion of the structure of inviscid axisymmetric modes for the sphere. We now consider the excitation of these modes.

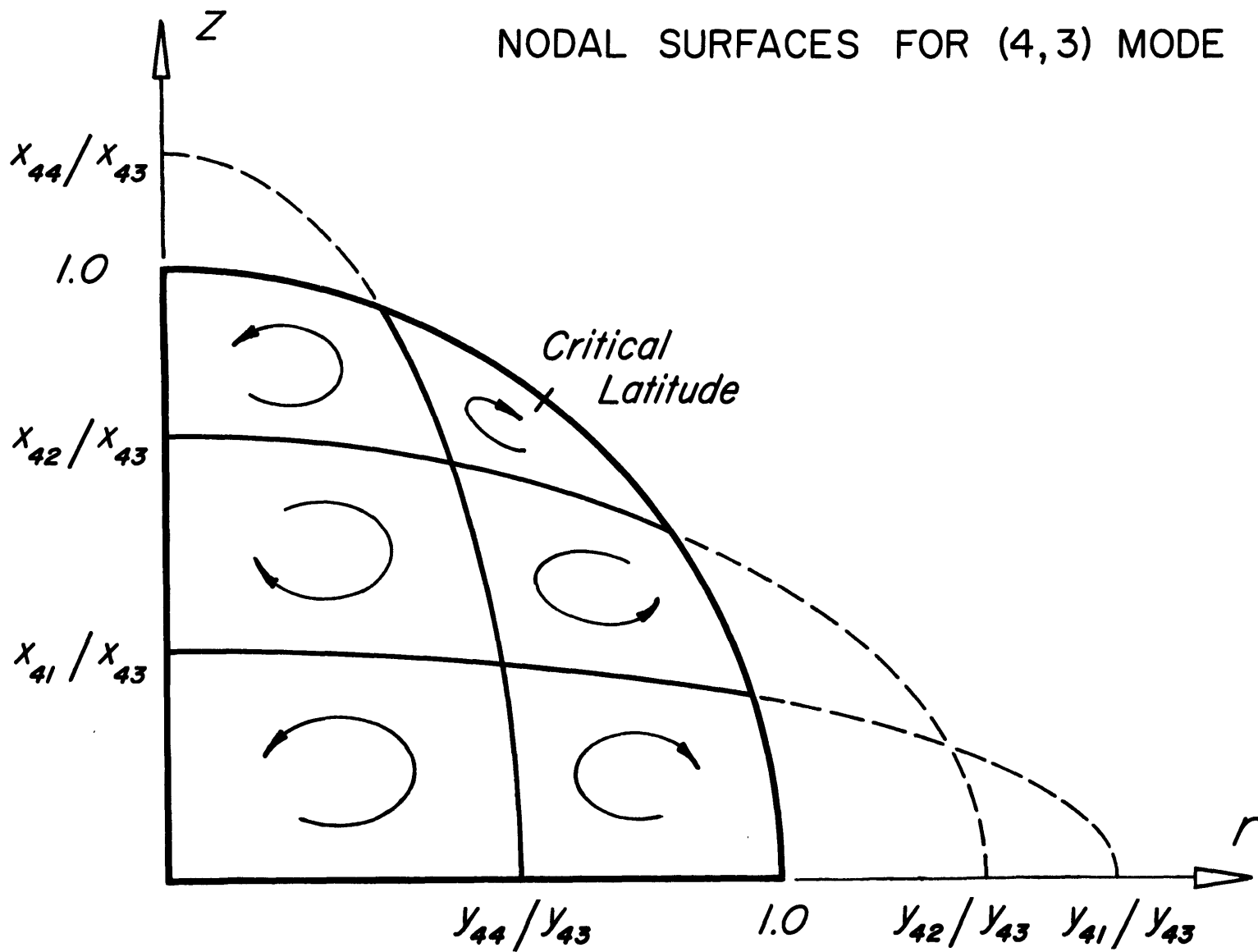
## 2.2 Excitation of inertial modes

The oscillations of the fluid interior were established and sustained by an exchange of fluid between the interior region and Ekman boundary layers. This boundary layer flow was produced by superimposing on the steady container rotation speed,  $\Omega$ , a periodic component,  $\epsilon \omega \cos \omega t$ . This oscillatory perturbation produced a shear stress at the surface of the sphere and a corresponding normal flow, whose direction reversed once each half cycle. A steady state version of this situation for a wind stress at the surface of the earth has been given by Prandtl (1952). In this case the normal velocity is proportional to the vertical gradient of the vorticity of the flow evaluated at the edge of the boundary layer.

Because this perturbation was a spatially simple one, it was expected that only the modes of simple structure would be

Figure 1. Nodal surfaces of the (4,3) mode. The stream function (represented schematically by the open curves with arrows) vanishes along the solid lines. Dashed lines complete the elliptical nodal traces outside the sphere. The  $\bar{x}$  intercepts are derived from  $X_{nm} = a/2 \bar{x}$ ; the  $\bar{r}$  intercepts from  $Y_{nm}^2 = 1 - X_{nm}^2$ .

# NODAL SURFACES FOR (4,3) MODE



excited. Even if it were possible, however, to stimulate the more spatially complex modes (larger  $n$ ) by this boundary layer flow, dissipation in the interior would rapidly limit the amplitude with increasing  $n$ . This fact is apparent from a consideration of the ratio of the scale of (interior/boundary layer) dissipation:

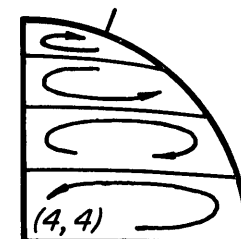
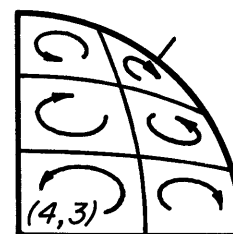
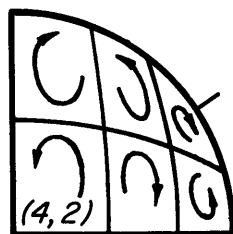
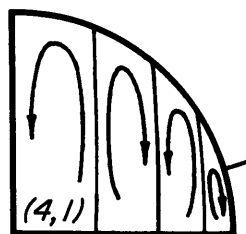
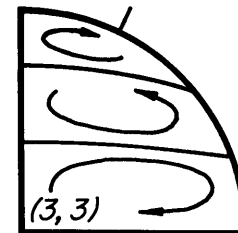
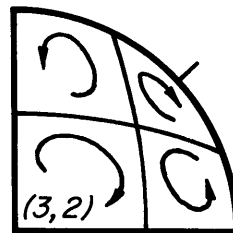
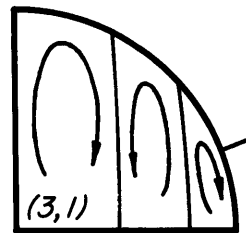
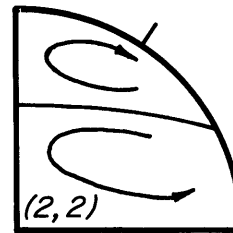
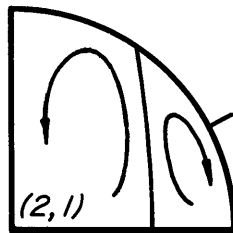
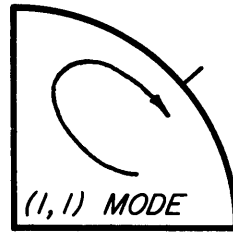
$$\frac{n^2 \nu}{a^2 \omega}$$

The theoretical amplitude and decay rates of the fluid response to the excitation described above, with the frequency of excitation chosen to coincide with a calculated eigenfrequency, have been given by Greenspan (1964). Toomre (1966) has calculated the resonant amplitude of several modes by balancing the mean boundary layer dissipation rate against the mean power input over the surface of the sphere. The details of this amplitude response calculation are given in Appendix II. Possible amplitudes for this condition lie on a circle, in the complex plane, which passes through the origin. Of all these amplitudes we choose the largest, which corresponds to minimum dissipation, as the resonant amplitude. The phase lag at resonance is then the angle between this maximum length vector and the real axis. Toomre has calculated the amplitudes for several of the modes and found agreement with the amplitudes calculated by Kudlick (1966), based on Greenspan's (1964) analysis. The rate at which



Figure 2. Streamlines for some axially and equatorially symmetric modes. The index  $(n, m)$  is constructed as follows:  $n$  is the number of modes in the family;  $m$  is the member within the family ( $1 \leq m \leq n$ ). Increasing  $m$  corresponds to increasing the ratio of horizontal to vertical motion. The bars normal to the surface of the sphere show the locations of the critical co-latitudes,  $\theta_c = \cos^{-1} \omega / 2\Omega$ .

SUMMARY OF MODES



the amplitude vector traces out the response circle is determined by the  $Q$  of the system. We use the definition

$$Q = \frac{\text{Total energy at resonance}}{\text{Loss in energy per radian of oscillation}}$$

The energy loss per radian of oscillation is found from the dissipation integrals of the amplitude response calculation. The functional dependence of phase lag with frequency is not given here; a simple mechanical analog which exhibits the important features of the response of the fluid and does have a known phase dependence on frequency, is discussed in Appendix III.

Quantitative experiments which will be discussed here are concerned with the measurement of pressure. The amplitude response calculations discussed above tell us that if the container rotates as

$$\Omega(t) = \Omega + \epsilon \omega \cos \omega t$$

then the velocity on the axis of the sphere at resonance, of the (1,1) mode say, will be

$$w(z, t) = 0.696 \epsilon \omega a z(1-z^2) \sin(\omega t - \phi_0)$$

The momentum equation for the  $w$  velocity is

$$\frac{\partial w}{\partial t} = -\frac{1}{\rho} \frac{\partial P}{\partial z}$$

The pressure gradient

$$\frac{\partial P}{\partial z} = -0.696 \rho \epsilon \omega^2 a z (1 - z^2) \cos(\omega t - \phi_0)$$

can then be integrated between a point on the axis,  $z = \alpha$ , say, and the pole,  $z = 1.0$ . The result is  $P(z=1.0) - P(z=\alpha)$

$$= -0.174 \rho \epsilon \omega^2 a^2 \left[ 1 - 2\alpha^2 \left( 1 - \frac{\alpha^2}{2} \right) \right] \cos(\omega t - \phi_0) \quad 2.11$$

In particular for a probe at the equator of the sphere,  $\alpha = 0$  and

$$P(1) - P(0) = -0.174 \rho \epsilon \omega^2 a^2 \cos(\omega t - \phi_0) \quad 2.11a$$

When the excess velocity of the container  $\epsilon \omega a \cos \omega t$  reaches a maximum value,  $\epsilon \omega a$  fluid rings next to the container wall will also have their maximum zonal velocity (except for the small phase lag  $\phi_0$ ) and hence will be in their maximum pole-ward position. This corresponds to fluid particles on the axis in their maximum equator-ward location and about to be forced away from the equator so that  $P(0) - P(a)$  has its maximum positive value, which is in agreement with the sign of 2.11a. Let  $\Delta P =$  amplitude of the (equator) - (pole) pressure difference; then for the (1,1) mode,

$$\Delta P = 0.174 \rho \epsilon \omega^2 a^2 \quad , \text{ and}$$

we define a pressure coefficient,

$$C_p = \Delta P / \rho e \omega^2 a^2 \quad 2.12$$

Corresponding to each mode there<sup>is</sup> is a unique  $C_p$  which expresses this dimensionless pressure difference. Both the theoretical amplitude response at resonance and the experimental results presented in the following sections will be expressed, where pressure has been measured, in terms of  $C_p$ .

### 2.3 Response of the sphere; $0.5 < \Omega/\omega < 2.0$ ; $z=0$

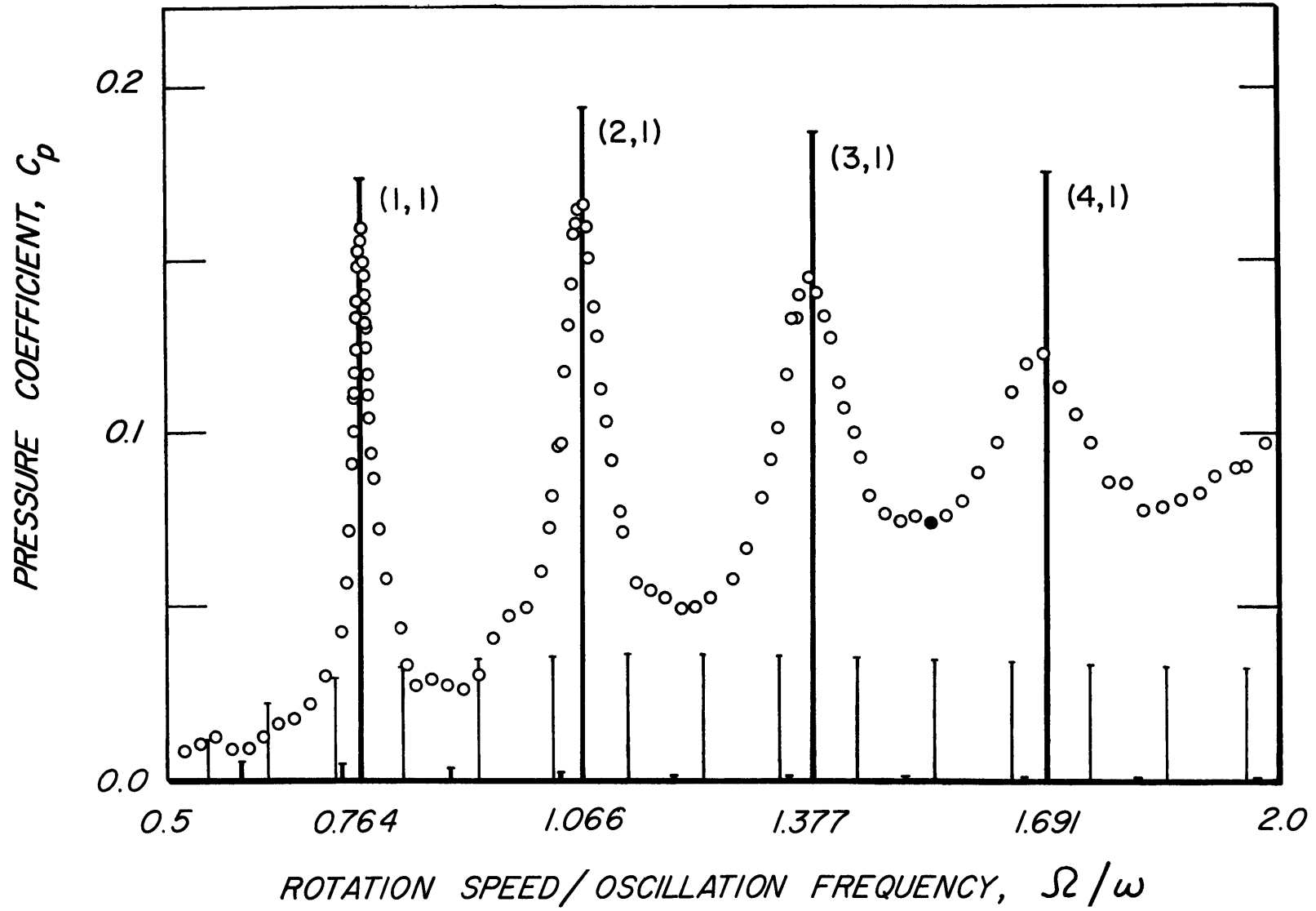
The spherical container was filled with water and the pressure probe was lowered on the axis to the location  $z=0$  (the equatorial plane). The container rotation was

$$\Omega(t) = \Omega + 0.14/\omega \cos \omega t .$$

The rotation speed,  $\Omega$ , was adjusted while the oscillation frequency,  $\omega$ , was held fixed. For each ratio of  $\Omega/\omega$ , the amplitude of the pressure response and its phase relative to the container oscillation were measured. Appropriate calibration constants as found in separate calibration experiments (Sections 6.3.1, 6.3.2) were incorporated to express the response in terms of the dimensionless pressure coefficient  $C_p$ , and absolute phase lag,  $\phi$ .  $\phi$  is the amount, in degrees, by which the maximum (equator) - (pole) pressure difference lags the maximum excess container rotation speed.

Figure 3a. Amplitude response of the sphere. Probe tip at  $z=0$ ;  $\epsilon = 8.0^\circ$ ; water;  $C_p = \Delta p / \rho \epsilon \omega^2 a^2$ . Vertical bars show theoretical inviscid locations and amplitudes of modes of the  $(n, 1)$ ,  $(n, 3)$  and  $(n, 2)$  families, in order of decreasing amplitude, for the range  $(0.5 < \Omega/\omega < 2.0)$ .  $\circ$  average of ten cycles at a particular  $\Omega/\omega$ ;  $\bullet$ , overtone.

AMPLITUDE —  $Z=0, \epsilon=8.0^\circ$



### 2.3.1 The amplitude spectrum

The amplitude spectrum for  $0.5 < \Omega/\omega < 2.0$  is shown in Figure 3a. The abscissa in the figure is the adjustable ratio,  $\Omega/\omega$ ; values shown are the theoretical (inviscid) locations of the (n,1) family of modes, (n=1,2,3,4). The heights of the wide vertical bars at these locations are the amplitudes of these modes, in units of  $C_p$ , for an inviscid fluid. Experimental points outline four distinct spectral peaks which coincide quite well in location with the theoretical inviscid modes but not so well in peak amplitude, the discrepancy being greater for more complex modes. The response of the mode which coincides in frequency with the theoretical (1,1) mode will be dealt with in more detail in section 2.6.

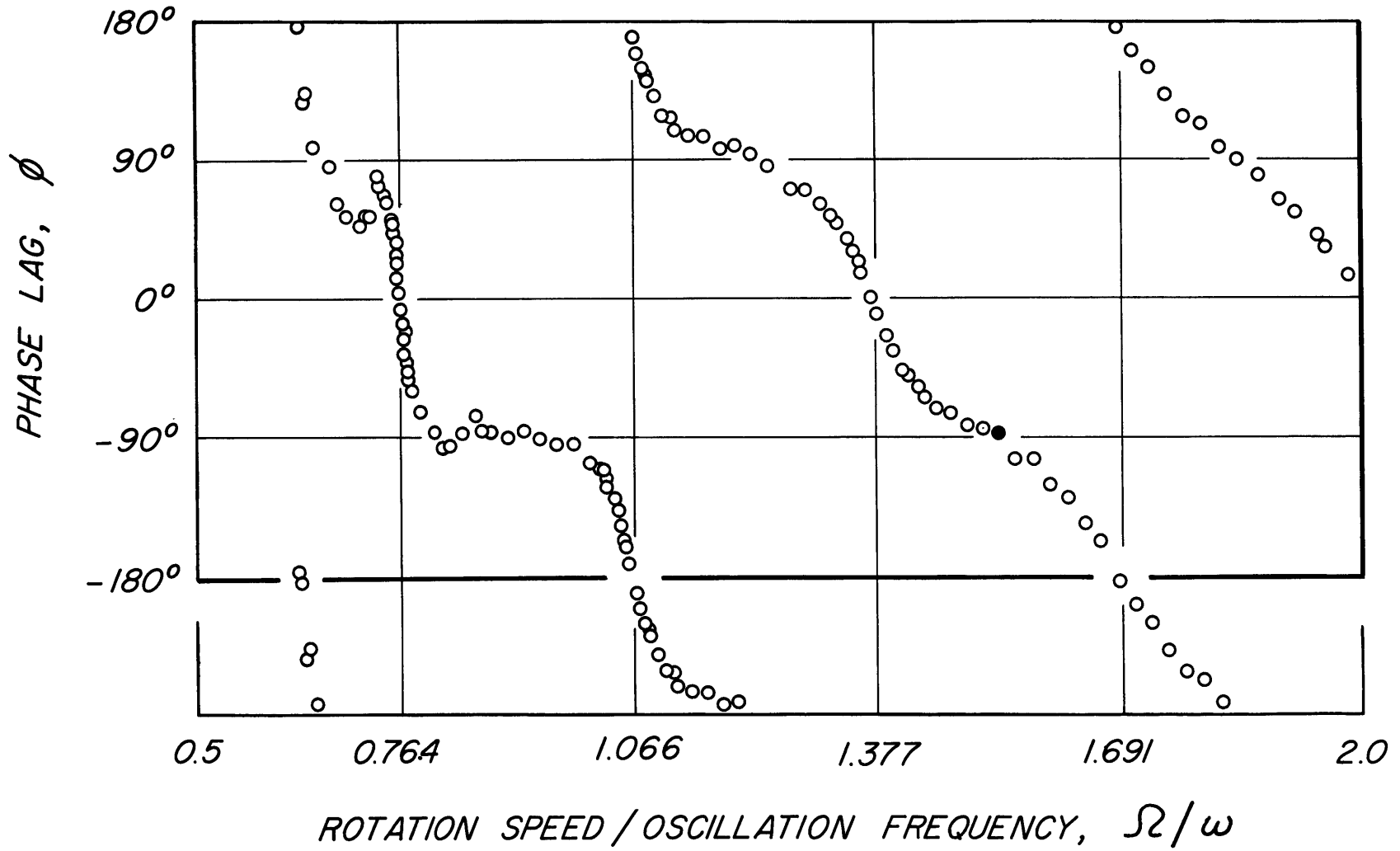
A regular rise in amplitude of the "valleys" between the peaks with increasing  $\Omega/\omega$  is observed. It is suggested that this rise is the effect of the tails of the individual modes adding up. This idea is followed up in more detail in the next section.

The wave form of the pressure signal is usually sinusoidal in appearance except near the location shown by the circles, , where an overtone is observed. The frequency location of this irregular wave form shows that it is probably the mode located at  $\Omega/\omega=0.764$  responding to a second harmonic of the oscillation drive, which we have thus far simply expressed as  $\epsilon \omega \cos \omega t$ . This suggestion is strengthened by the structure of the power spectrum of the oscillation drive discussed in section 2.6.



Figure 4 a. Phase response for the sphere. Probe tip at  $z=0$ ;  $\epsilon = 8.0^\circ$ ; water.  $\phi$  is the magnitude in degrees by which the peak (equator)-(pole) pressure difference lags the maximum angular velocity of the container at each  $\Omega/\omega$ .

PHASE —  $Z=0, \epsilon=8.0^\circ$



### 2.3.2 The phase spectrum

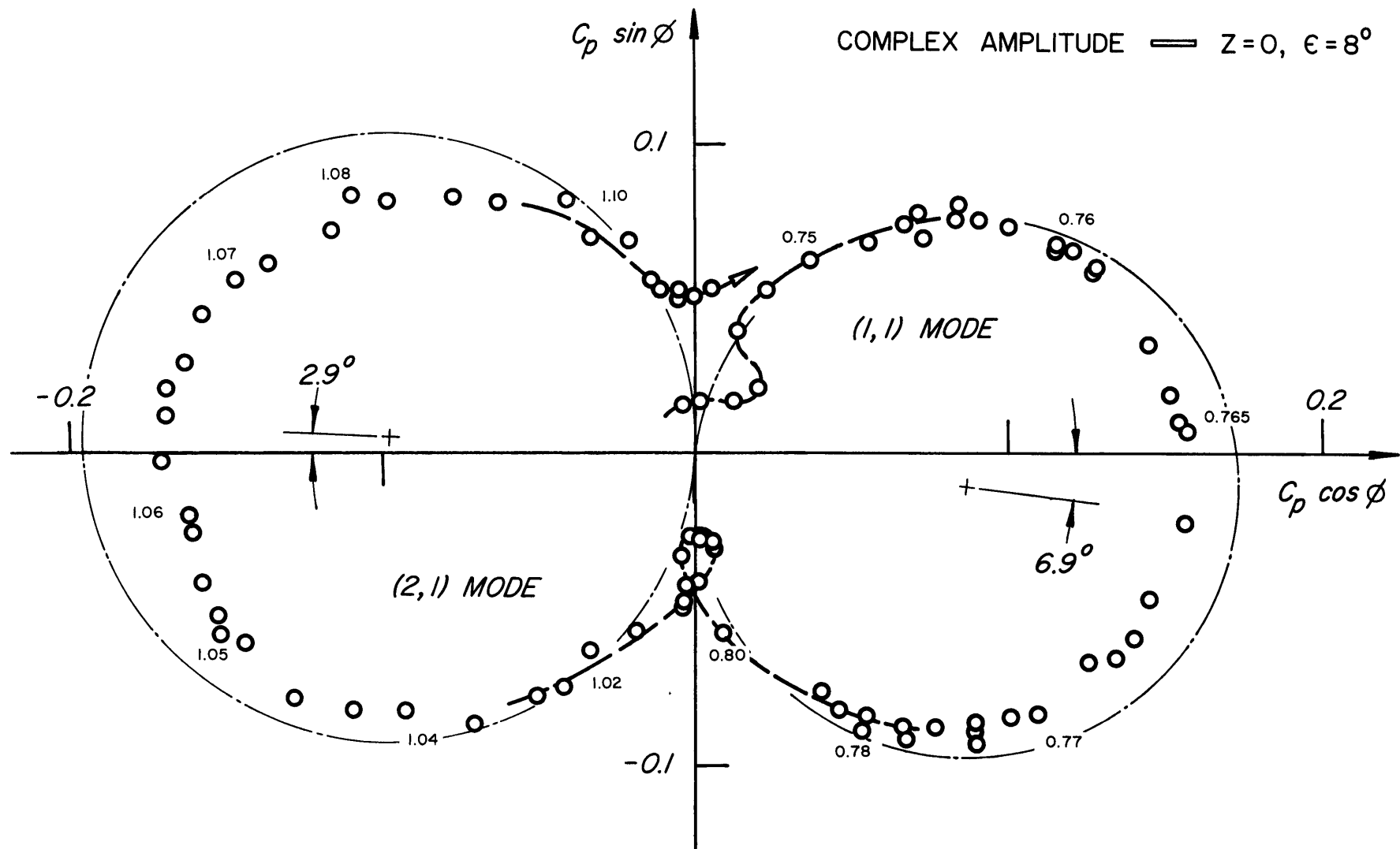
The phase lag,  $\phi$ , in degrees, as a function of  $\Omega/\omega$  is shown in Figure 4a. The region  $90^\circ < \phi < 180^\circ$  is repeated at the bottom of the figure for continuity.

The phase changes rapidly with  $\Omega/\omega$  near the spectral peaks of figure 3a and slowly in the valley regions. From one mode to the next the phase at maximum amplitude decreases by  $180^\circ$ . This result is qualitatively what we would expect from a consideration of the structure of the flow as shown in Figure 2. The sense of the flow for each mode shown in this figure is that which would be seen for the same container phase throughout. The  $180^\circ$  phase change from one mode to the next of the (n,l) series is then simply related to the number of "cells" within the mode.

### 2.3.3. The complex amplitude

The experimental points of the first two modes of Figures 3a, 4a have been combined for the polar plot shown in Figure 5. The polar angle is the phase angle of Figure 4a; the amplitude is the pressure coefficient of Figure 3a. The numbers listed beside the data points are the corresponding values of  $\Omega/\omega$ . The dash-dot lines are the theoretical response circles which were found by balancing dissipation with energy input over the surface of the sphere. This form of presentation of the data is convenient for viewing the amplitude and phase results simultaneously; the slight phase lead at maximum amplitude, shown by the theoretical response circles, is apparent, though to a lesser extent, in the data.

Figure 5. Complex amplitude response of the sphere. Probe tip at  $Z=0$  ;  
 $\epsilon = 8.0^\circ$  ; water;  $C_p = \Delta P / \rho \epsilon \omega^2 a^2$  ;  $\phi$  is the phase  
 angle of figure 4a.  $\circ$  experimental points of figures 3 and 4; some values  
 of  $\Omega/\omega$  are listed outside the circle of data points.            -            ,  
 traces theoretical response circles (Appendix II) for the ( 1, 1 ) and  
 ( 2, 1 ) modes; centres of the circles lie off the  $C_p \cos \phi$  axis by the  
 amount shown.



#### 2.3.4 Summary of spectral results

The frequency ratio,  $\Omega/\omega$ , amplitude,  $C_p$ , and phase,  $\phi$ , at resonance for each of the four modes observed with the probe at  $\theta=0$  and  $\epsilon=0.141$  ( $8.0^\circ$ ) are summarized in Table 1. The numbers in parentheses are estimates of statistical errors in the least significant figure of the quantity they accompany.

The experimental values of  $\Omega/\omega$  are all well within 1% of those given by inviscid theory; there is a slight suggestion that the experimental ratios,  $\Omega/\omega$ , are less than the theoretical ones, the discrepancy being greater for more complex modes.

The amplitude at resonance,  $C_p$ , has already been seen from Figure 3a to fall short of the theoretical values. The phase lag,  $\phi$ , at resonance has been found from the tilt of the response circle of data points in the complex plane.

#### 2.4 Superposition of modes

It was suggested in Section 2.2 that the general rise in valley amplitude with increasing  $\Omega/\omega$  was due to the tails of the modes reinforcing one another. We would like to know, therefore, what the theoretical response of the sphere is off resonance.

As a first step in obtaining the off resonance response, we assume that each mode may be considered separately of all others, even off resonance. If, then, we knew the amplitude dependence on frequency for any one mode, we could obtain the total response for all modes by a vector summation. This is

**Table 1. Summary of results at resonance for the sphere.**

SUMMARY OF RESULTS AT RESONANCE FOR THE SPHERE

$Z = 0, \epsilon = 8.0^\circ$

MODE	$\Omega/\omega$		PRESSURE COEFFICIENT $C_p$		PHASE LAG $\phi^\circ$	
	EXPERIMENT	THEORY	EXPERIMENT	THEORY	EXPERIMENT	THEORY
(1,1)	0.764 (1)	0.764	0.158 (2)	0.174	-5 (2)	-7
(2,1)	1.064 (2)	1.066	0.166 (3)	0.194	181 (2)	177
(3,1)	1.375 (3)	1.377	0.145 (3)	0.187	-6 (3)	-2
(4,1)	1.685 (5)	1.691	0.124 (2)	0.176	178 (3)	179



tantamount to asking what is the rate at which the amplitude vector traces out its possible values on the response circle with frequency,  $\Omega/\omega$ . Although we know qualitatively that this rate is related to  $Q$  of the mode, which was calculated in Section 2.2, the rate has not been given explicitly.

A convenient mechanical analogue, suggested by Toomre, does, however, exhibit almost the same amplitude response circle as a single mode of the sphere. The amplitude dependence of this analogue is easily worked out (Appendix III); we need only add a non zero phase angle at resonance and possible amplitudes for the response of a single mode of the sphere and analogy are identical. If the subscript  $i$  refers to the  $i^{\text{th}}$  mode, of resonant frequency ratio  $R_i$ , quality factor  $Q_i$ , resonant amplitude  $A_i$  and phase  $\phi_i$ , of the  $M$  modes being summed, then the total response at a given  $R$  is

$$Z(R) = \sum_{i=1}^M Z_i(R)$$

$$Z_i(R) = A_i \cos[\phi(R) - \phi_i]$$

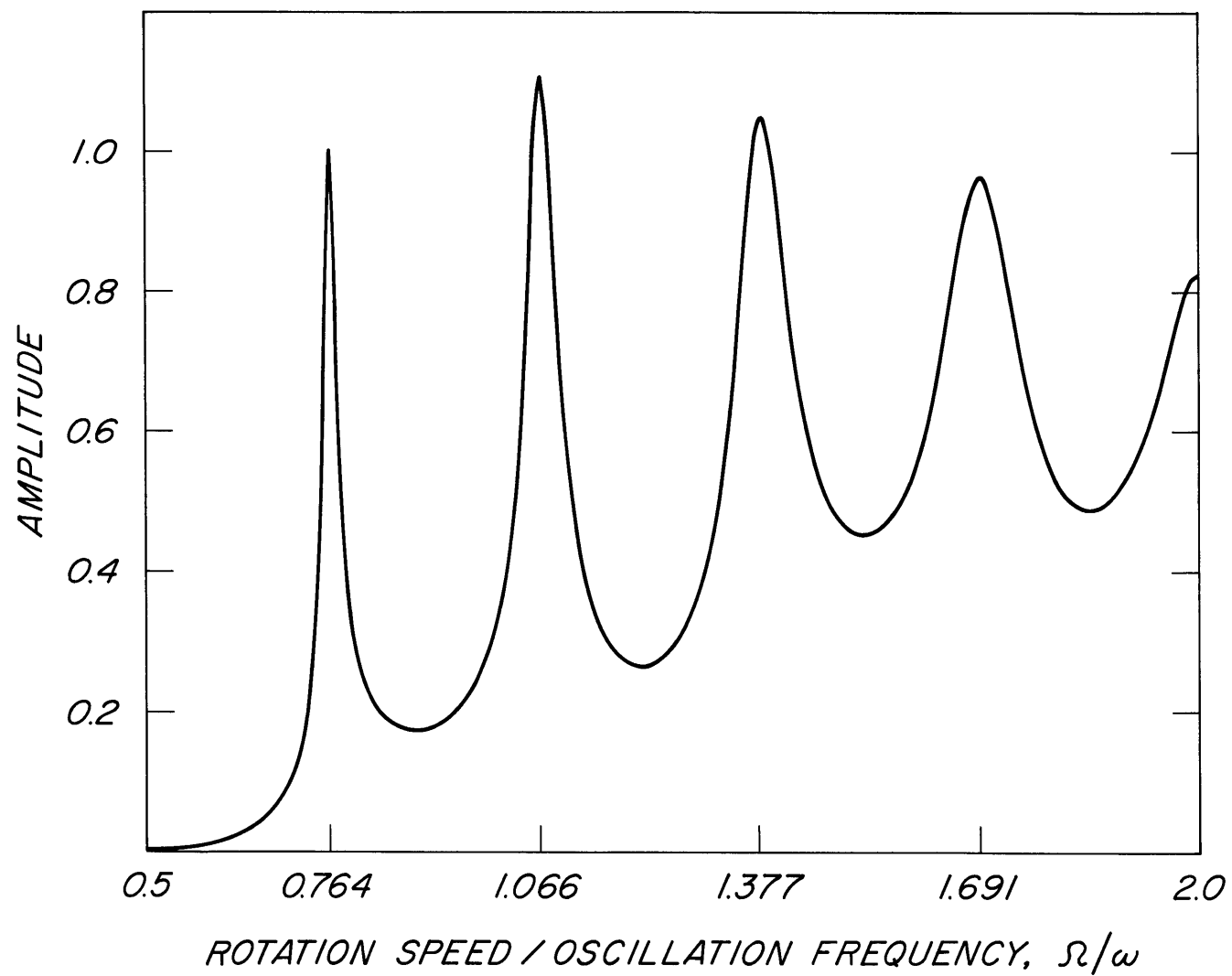
$$\phi(R) = \phi_i + \tan^{-1} \left[ Q_i \frac{1 - (R/R_i)^2}{R R_i} \right]$$

$X_i = Z_i \cos \phi$ , the in-phase component,  $Y_i = Z_i \sin \phi$ , the quadrature component.

This summation was carried out over 10 modes of the  $(n,1)$  family for  $(0.5 < \Omega/\omega < 3.6)$  in order to include the effect of the

Figure 3b. Amplitude response of the vector sum of first 10 modes of the  $(n, 1)$  family;  $(0.5 < \Omega/\omega < 3.6)$ . Only the first 4 of these ten modes lie within the range of the experiments. Theoretical complex amplitudes at resonance and  $Q$ 's for each of the ten modes were the inputs for the superposition (Appendix III).

SUPERPOSITION OF MODES — AMPLITUDE



tails of modes beyond the range of experimental interest ( $0.5 < \Omega/\omega < 2.0$ ). The amplitude response for the summation is shown in Figure 3b. A definite rise, with increasing  $\Omega/\omega$ , of the valleys between the peaks is apparent; even the structure of the rise is, in fact, similar to one of figure 3a. Phase response for the summation is shown in Figure 4b. Generally, the structure is similar to that of Figure 4a, except for the range ( $0.5 < \Omega/\omega < 0.764$ ) where the departure is probably due to the absence of the (3,3) and (4,3) modes in the model.

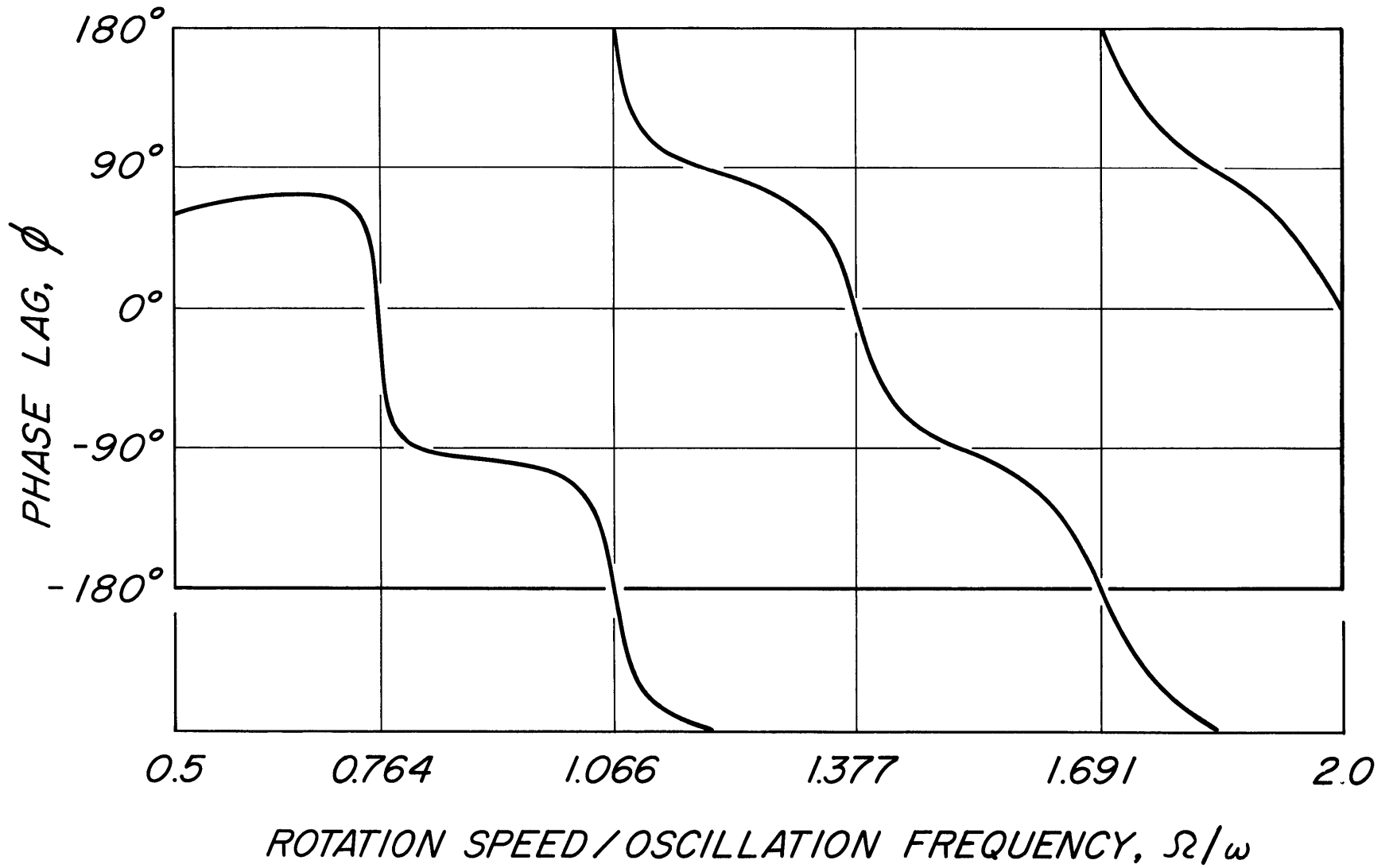
The effect of the superposition on the frequency location, amplitude and phase at resonance of the (1,1), (2,1), (3,1) and (4,1) modes is summarized in Table 2. The columns labeled "input" contain the data used in the superposition; the columns labeled "output" are the input quantities after their adjustment by the presence of the other modes. A tendency is observed for the resonant frequency ratios,  $\Omega/\omega$ , to increase after the superposition and the amplitudes at resonance to decrease.

The phase at resonance seems to show a general clockwise twisting about the origin in the complex plane. (The phase for (2,1) and (4,1) modes has been expressed in terms of the number of degrees by which the amplitude vector lags the line  $\phi=180^\circ$ ).

The Q of the modes, after the superposition, shows some interesting features. The effect of neighboring modes, which is most apparent in the Q's of the (3,1) and (4,1) modes, seems to increase the Q as measured from the  $45^\circ$  phase points and to

Figure 4b. Phase response for the vector sum of modes as given in figure 3b.

SUPERPOSITION OF MODES — PHASE



decrease it as measured from the half power points. This discrepancy is most easily resolved by considering the measurement of  $Q$  from a complex amplitude plot. If only one mode were present the response vector would trace out a circle of diameter  $d$ , say, passing through the origin; another circle,  $C_{hp}$  of the radius  $r=d/\sqrt{2}$  with centre at the origin would intersect the response circle at points corresponding to frequencies  $f_1, f_2$  above and below the resonant frequency  $f_0$ . Lines at  $\pm 45^\circ$  to the main diameter of the response circle would also intersect the response circle at  $f_1$  and  $f_2$ . Thus

$$Q = f_0 / f_2 - f_1$$

would be the same for both the  $45^\circ$  phase points and the half power points. With other modes present, however, the actual response curve is drawn out in a direction perpendicular to the main diameter of the response circle and the  $45^\circ$  lines will in general intersect the response curve at a point closer to the resonant frequency, thus increasing the measured  $Q$ ; the half power circle,  $C_{hp}$ , will, in general, intersect the response curve at a point further from the resonant frequency  $f_0$ , thus decreasing the measured  $Q$ . We shall see in Section 2.7, where the transient response of the sphere is discussed, that this type of discrepancy also appears in experimental  $Q$ 's.

Table 2. Superposition of modes of the  $(n, 1)$  family,  $n = 1, 2, 3, \dots, 10$ .



SUPERPOSITION OF MODES OF THE (N,1) FAMILY, N=1,2,...,10

MODE	FREQUENCY		AMPLITUDE		PHASE		Q		
	INPUT	OUTPUT	INPUT	OUTPUT	INPUT	OUTPUT	INPUT	HALF POWER	45 DEGREE
(1,1)	0.7638	0.7643	1.0000	1.0035	-6.19	-12.85	43.32	42.89	42.86
(2,1)	1.0664	1.0666	1.1170	1.1121	-2.93	-4.19	26.17	26.20	26.70
(3,1)	1.3770	1.3792	1.0758	1.0550	-1.63	-8.84	19.54	18.31	20.93
(4,1)	1.6906	1.6900	1.0091	0.9638	-1.02	-0.27	15.44	13.85	17.99

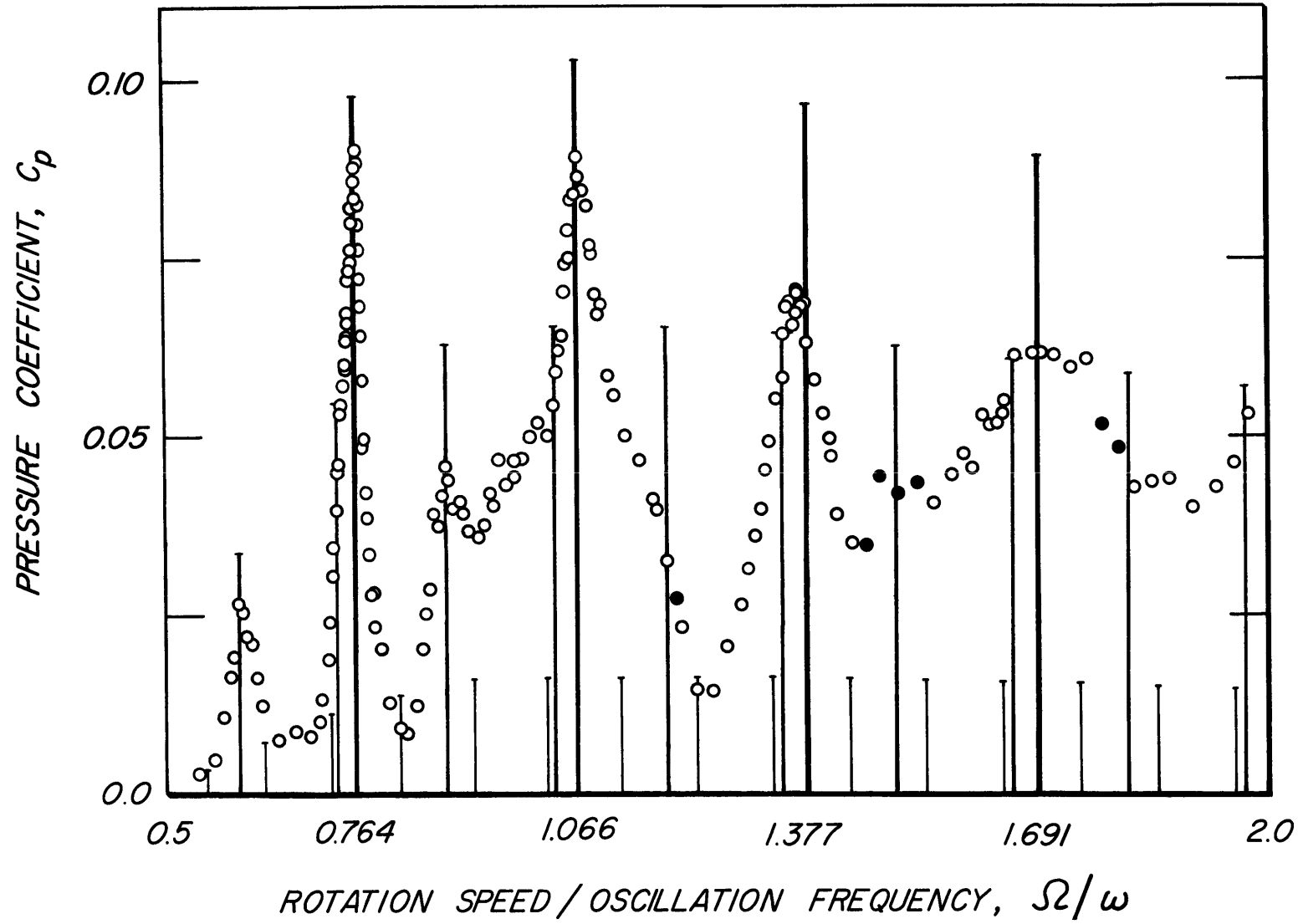
2.5 Response of the sphere;  $0.5 < \Omega/\omega < 2.0$ ;  $z=0.5a$

Although there are many modes of rather simple structure in the interval  $(0.5 < \Omega/\omega < 2.0)$  it was found (Figure 3a) that essentially only 4 of these modes were observed with the probe tip at  $z=0$ . Reference to Figure 2 shows clearly why this is so. Modes of the family,  $(n,2)$ ,  $n=2,3,4\dots$ , have axial pressure gradients over the interval  $(0 < z/a < 1)$  which oppose one another, so that there is essentially no pressure drop between the equator and pole for this family. To "pick out" modes of this family, it is necessary to measure the pressure difference between the pole and a point roughly half way down to the equator. The probe was raised, therefore to the point  $z/a=0.5$  and the rotation speed,  $\Omega$ , was again adjusted for  $(0.5 < \Omega/\omega < 2.0)$ . The amplitude spectrum for these conditions is shown in Figure 6.

It is found, as further consideration of Figure 2 would have revealed, that the  $(n,1)$  family is still present, only at approximately half the amplitude. The tallest bars are the expected (inviscid) amplitudes for this family; the next to the tallest series of bars is the  $(n,2)$  family for  $z=0.5a$ . Two modes corresponding to the  $(n,2)$  family are clearly visible; the  $(2,2)$  mode is to the left of the  $(1,1)$  and the  $(4,2)$  mode is approximately midway between the  $(1,1)$  and  $(2,1)$  modes. The solid circles again are overtones, in this case for the  $(2,2)$ ,  $(1,1)$  and  $(4,2)$  modes.

Figure 6. Amplitude response of the sphere. Probe tip at  $z=0.5a$  ;  
 $\epsilon = 8.0^\circ$  ; water;  $C_p = \Delta P / \rho \epsilon \omega^2 a^2$  . Vertical bars  
are theoretical locations and amplitudes of modes of the  $(n, 1)$ ,  $(n, 2)$   
and  $(n, 3)$  families, in order of decreasing amplitude, in the range  
 $(0.5 < \Omega/\omega < 2.0)$ .  $\circ$  average of 10 cycles at a fixed  $\Omega/\omega$  ;  
 $\bullet$  , overtone.

AMPLITUDE —  $Z = 0.5 \alpha$ ,  $\epsilon = 8.0^\circ$



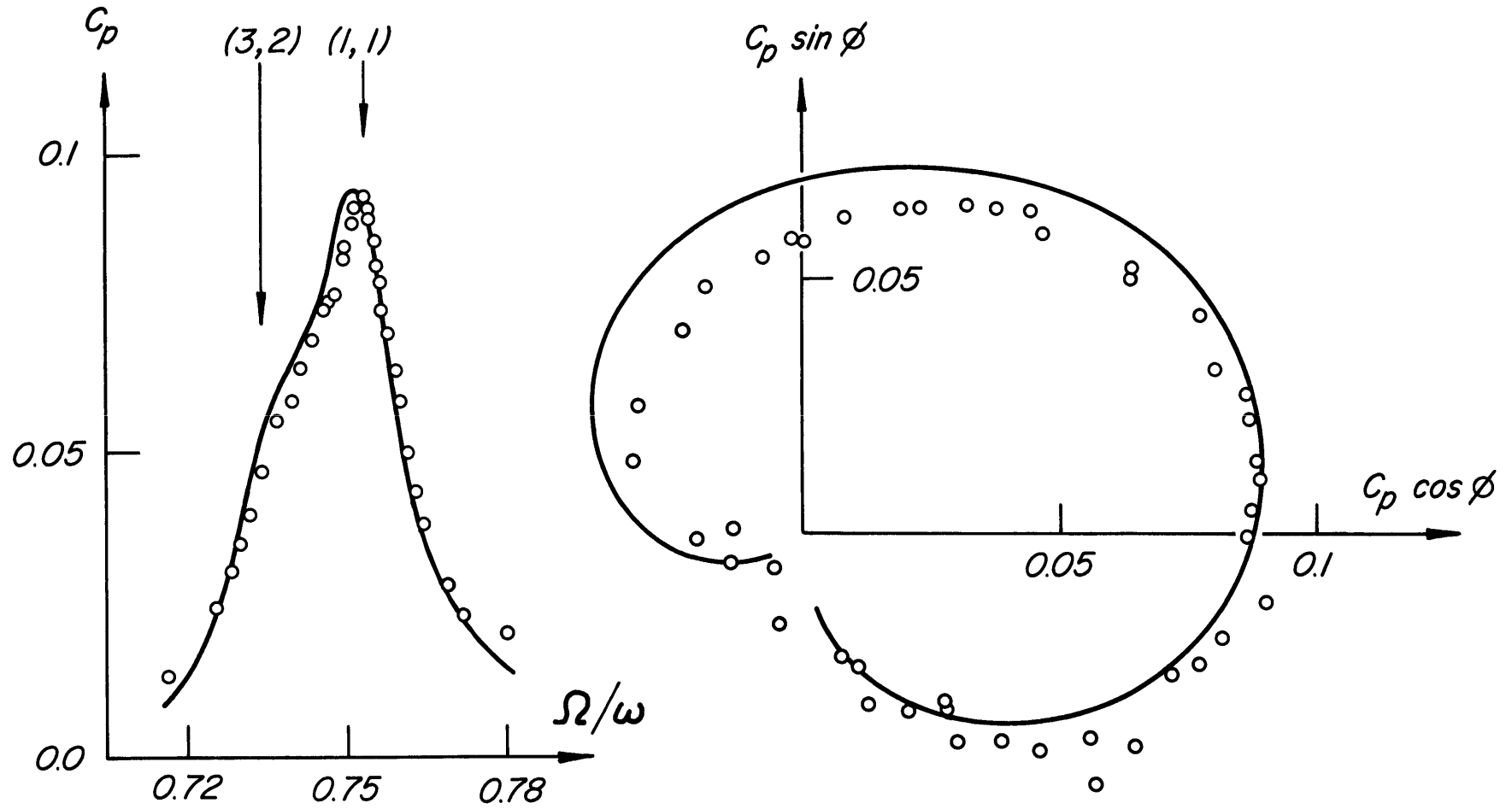
Of particular interest is the slight asymmetry of the (1,1) mode ( $\beta/\omega=0.764$ ) due to the (3,2) mode ( $\beta/\omega=0.738$ ) nearby. The experimental points in the vicinity of  $\beta/\omega=0.75$  are shown on an expanded scale in  $\beta/\omega$ , to bring out this asymmetry, at the left of Figure 7. The total (complex) amplitude of the same experimental points is shown on the right in the same figure. The heavy solid line on the right is the vector sum, taken in the fashion described in Section (2.4), of the (1,1) and (3,2) modes. The heavy line to the left is the amplitude of this sum as a function of frequency obtained from the total response calculated on the right. The general structure of the theoretical response seems to be in agreement with the experimental results, although there appears to be a slight counterclockwise rotation of the theoretical complex amplitude relative to the experimental points. Estimates of dissipation in the interior, not taken into account in the resonant amplitude calculation, show that the response at resonance of the (3,2) mode should be considerably smaller; this would have the effect of rotating the resultant complex response curve by a small clockwise amount.

## 2.6 Details of the (1,1) mode

This section is concerned with some of the details of the (1,1) mode. Pressure is measured for several locations on the axis for a fixed value of  $\beta/\omega$  close to the (1,1) peak. A rectified flow which is closely approximated by a square law dependence

Figure 7. Structure of the  $(3,2) + (1,1)$  peak. Probe tip at  $z=0.5a$ ;  
 $\epsilon = 8.0^\circ$ ; water;  $C_p = \Delta P / \rho c \omega^2 a^2$ ;  $\phi$  is the phase  
 angle of figure 4.  $\circ$ , experimental points; — theoretical response.  
 Right - complex amplitude response for  $\Omega/\omega$  near the  $(3,2) + (1,1)$   
 peak. Theoretical response is the vector sum of individual  $(3,2)$  and  
 $(1,1)$  responses. Left - amplitude response; the theoretical response was  
 obtained from the curve on the right.

"FINE STRUCTURE" OF (3,2)+(1,1) PEAK —  $Z = 0.5a$ ,  $\epsilon = 8.0^\circ$



on angle of oscillation is found near this peak. A shift in the observed location of resonance of the (1,1) mode as a function of oscillation angle is observed.

Considerable effort was expended in finding the experimental pressure coefficient,  $C_p$ , for this mode as the half amplitude of oscillation,  $\xi$ , was decreased.

Finally, some pressure traces of rather interesting frequency content at large angles of oscillation (Rossby number  $\sim 1/3$ ) were Fourier analysed and a power spectrum was computed.

#### 2.6.1 Pressure profile

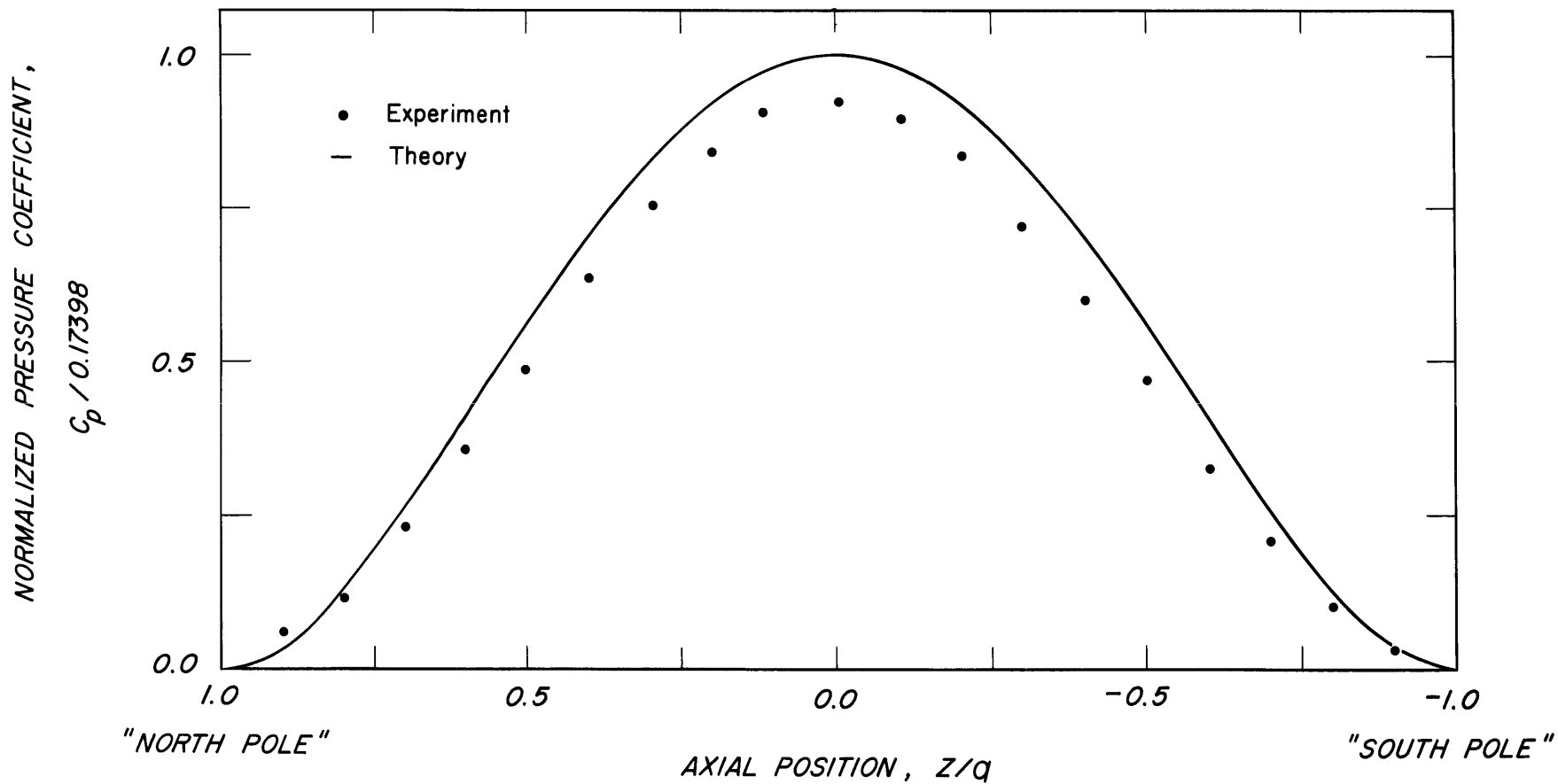
In addition to causing some dissipation, the probe used to measure pressure could perhaps introduce an asymmetry about the equator in the flow. Both for this reason and to confirm the general internal structure of the oscillation, pressure was measured at several points in the interval ( $-1.0 < z/a < 1.0$ ) for the (1,1) mode, ( $1/2 \omega = 0.765$ ). The results are shown in Figure 8. Experimental points are measured pressures, with appropriate calibration constants included, for the axial positions shown. The curved line is the pressure coefficient  $C_p$  as a function of depth (Equation 2.11) of Section 2.2). The discrepancy between the points and the line at  $z/a=0$  is the same one we saw earlier in the (1,1) spectral peak of Figure 3a. This loss in response will be discussed in Section 2.6.4.

A slight asymmetry about the line  $z/a=0$  of the experimental results is apparent when it is pointed out that the points are



Figure 8. Axial pressure response for the  $(1, 1)$  mode. — Theoretical response; • , experimental results for probe of  $i.d = 1mm$ ,  $o.d = 2mm$ . Each point is the average of 10 oscillation cycles; a calibration constant appropriate to the response amplitude at each  $z/a$  location was applied. Slight asymmetry with respect to the line  $z=0$  is probably due to the effective increase in probe length because of the region of stagnant fluid at the probe tip.

PRESSURE PROFILE (1,1) MODE,  $\Omega/\omega = 0.765$ ,  $\epsilon = 8.1^\circ$



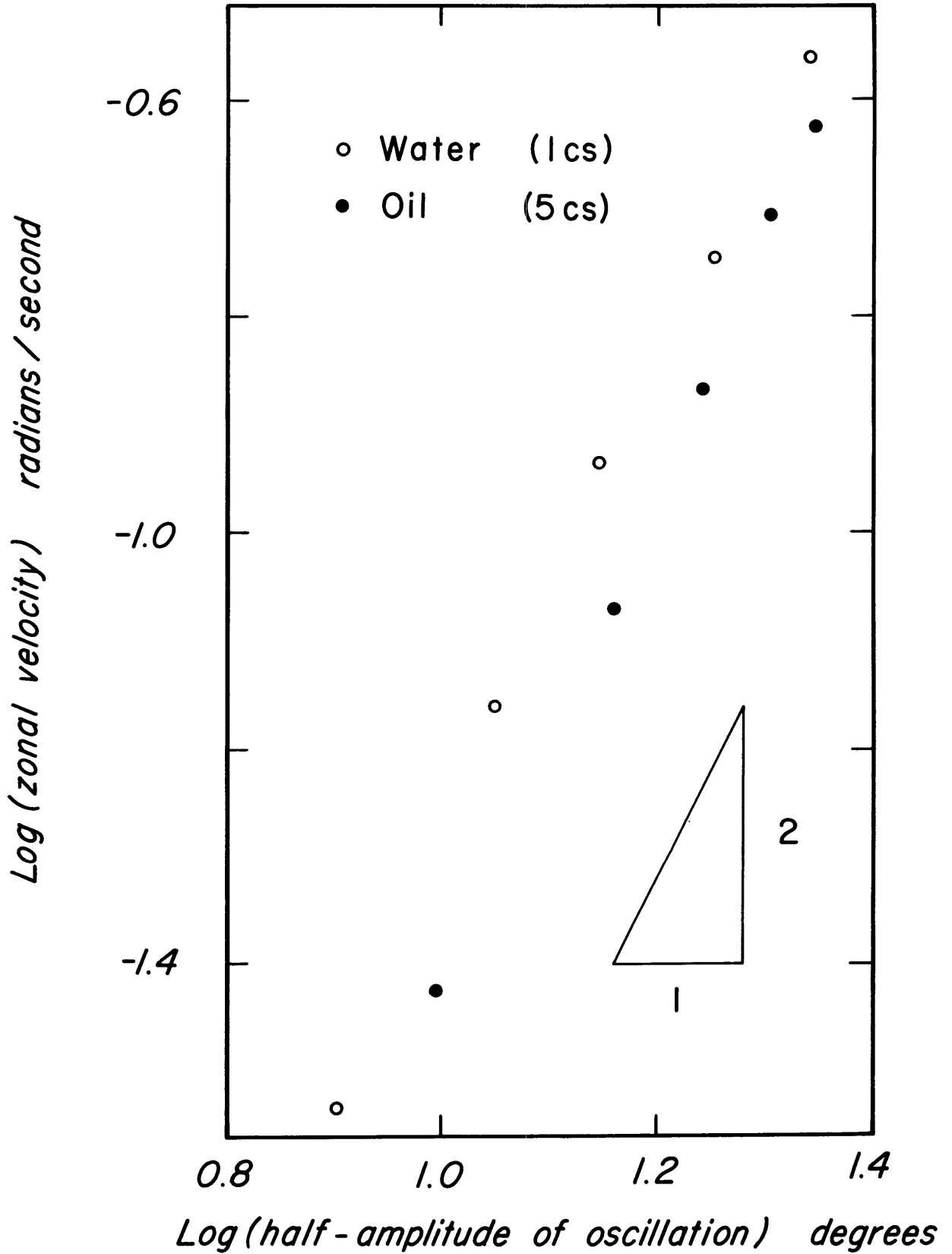
spaced at equal (1 cm) intervals in  $\theta$ . Points in the northern hemisphere have consistently larger values than their counterparts in the southern hemisphere. This asymmetry is accounted for by a consistent error in the measured location of the probe tip. The sense of the error, to be explained, is such that pressures observed come from a greater depth than the measured one. This error is apparently from an effective lengthening of the probe by a stagnant region of fluid at the probe tip. This "lengthening" is estimated to be  $d/4$  for a probe of diameter  $d$ . Such a correction applied to these points ( $d=0.2$  cm) essentially removes the observed asymmetry.

#### 2.6.2 Zonal current

Theory had predicted a double viscous boundary layer (Appendix II) for the oscillating sphere at resonance. Of particular interest was the component of this double layer, which, from the linear theory, grew without limit at a co-latitude  $\theta_c = \cos^{-1} X_m$  where  $X_m = \omega/2\Omega$  for the mode under consideration. Some dye was injected, therefore, at the critical latitude of the (1,1) mode. The most striking result was that the dye was swept away from the point of injection and began to drift, retrograde to the rotation  $\Omega$ . This dye technique was obviously inadequate for the study of oscillatory boundary layers, so it was discontinued for that purpose but retained to study this rectified current. An average drift period for the rectified flow near the critical

Figure 9. Steady zonal current for the (1,1) mode as calculated from the circulation period of a tagged parcel of fluid injected at the critical latitude,  $40.7^\circ$ .  $\circ$  water (0.94 cs);  $\bullet$  silicone oil (5.3 cs); triangle shown gives square law dependence of zonal velocity with half-amplitude of oscillation.

ZONAL CURRENT  $\equiv$  (1,1) MODE



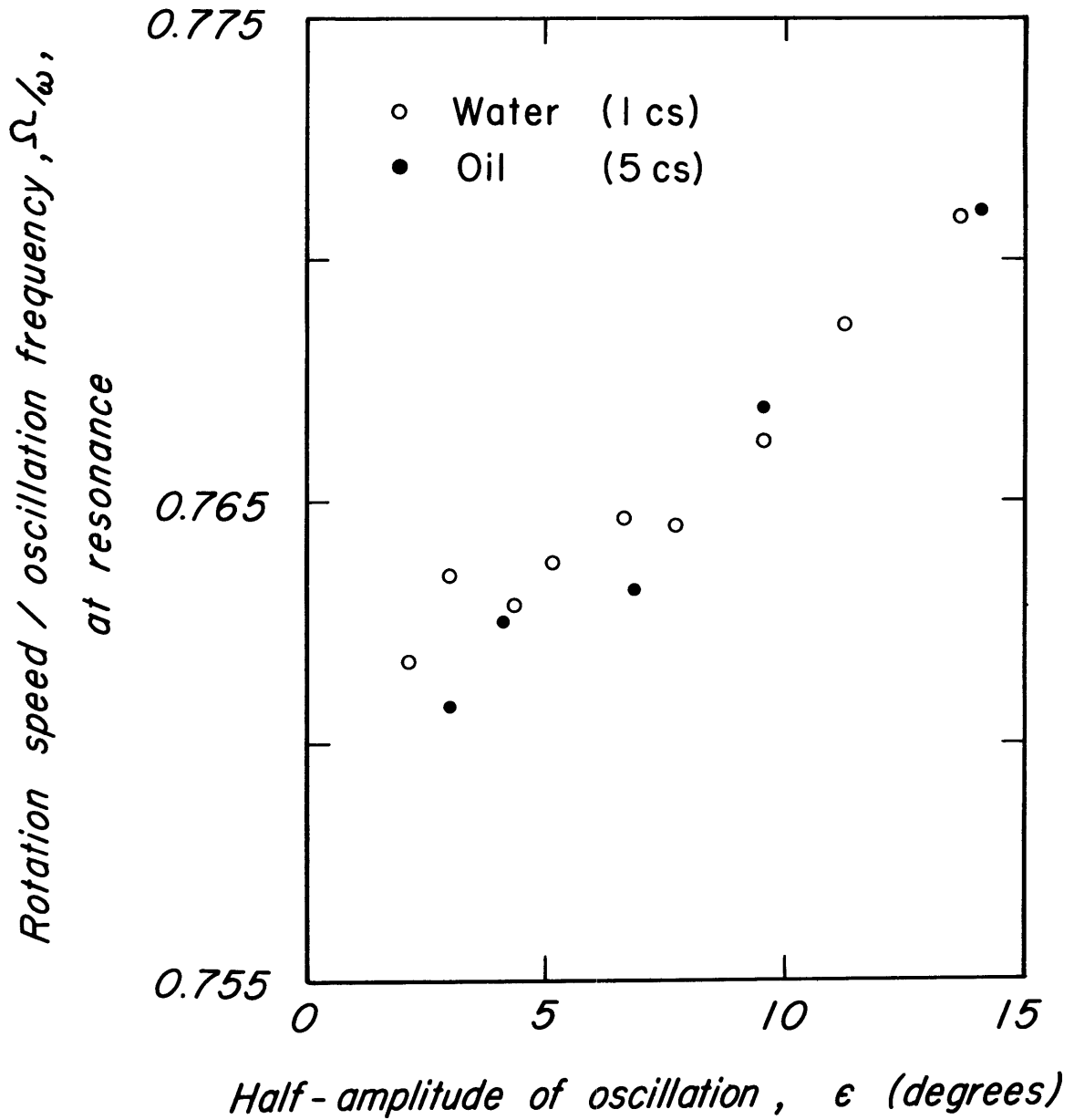
latitude was calculated from dye blob circulation periods for each of several oscillation angles,  $\epsilon$ . The results for water ( $\nu=0.94\text{cs}$ ) and a silicone oil ( $\nu=5.3\text{cs}$ ) are presented in Figure 9. The logarithmic plot suggests a square law dependence of the average rectified current on the oscillation amplitude. The drift velocities for the water are slightly higher than those for oil for each  $\epsilon$ .

### 2.6.3 Resonance "shift"

The observed ratio,  $\Omega/\omega$ , for the maximum response of the (1,1) mode showed a small but regular increase with increasing amplitude of oscillation,  $\epsilon$ . The resonant frequency ratio for the (1,1) mode over the interval ( $2^\circ \leq \epsilon \leq 15^\circ$ ) for both water and the silicone oil is plotted in Figure 10. We have just seen (Figure 9) that the fluid is actually rotating at a mean speed which is less than that given by the mean rotation speed of the container. It is found, however, that an observed mean drift of the fluid,  $\delta\Omega=0.045$  for  $\epsilon=10^\circ$ ) should produce an increase in the ratio  $\Omega/\omega$  of  $\delta\Omega/\omega=0.007$  which is about twice the shift observed in Figure 9. The mean drift as measured at points below the critical latitude does not, therefore, tell the whole story of the apparent resonance shift. Additional sources of this shift seem to be lacking. If, for example, we postulate a shape change in the inviscid interior due to thickening of boundary layers at lower latitudes, we find that such a prolate interior would then have

Figure 10. Resonance "shift" of  $\Omega/\omega$  for (1,1) mode as a function of half amplitude of oscillation,  $\epsilon$  (degrees).  $\circ$  water (0.94cs);  $\bullet$ , silicone oil, (5.3cs). This shift is partly due to a counter-rotation zonal drift of the fluid as observed by following dye traces at middle latitudes (figure 9).

RESONANCE "SHIFT"  $\equiv$  (1,1) MODE





a slightly larger resonant frequency ratio  $\Omega/\omega$ , leaving us even further from explaining a shift which is already too large. A slightly oblate interior would have a lower resonant frequency ratio but there seems to be no good reason for suggesting an oblate interior.

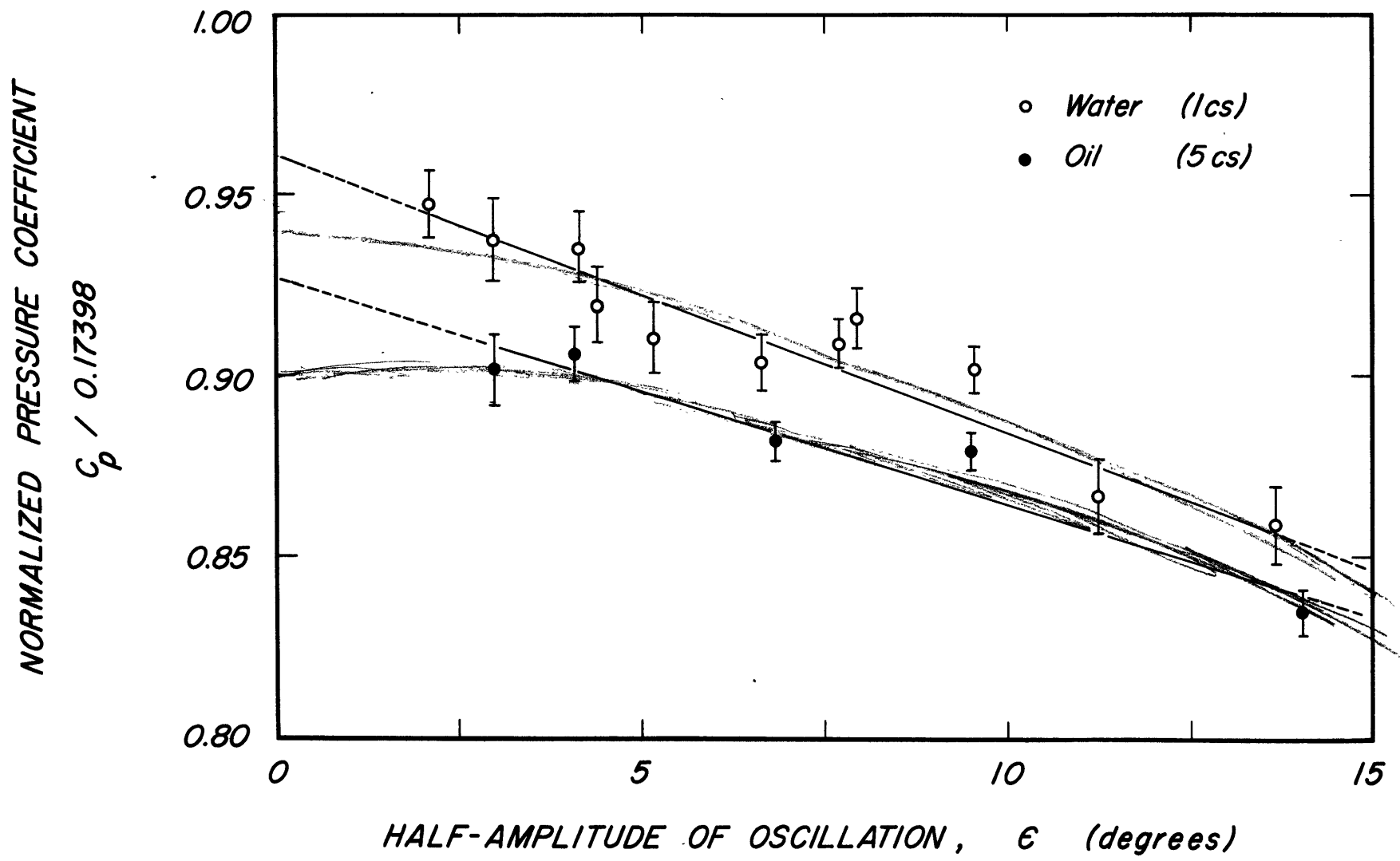
It would appear, therefore, that the mean drift speed of the fluid,  $\delta\Omega$ , as measured at the critical latitude, is considerably greater than the mean drift taken over the entire sphere as experienced by the inviscid interior.

#### 2.6.4 Response at resonance; (1,1) mode

It was noted earlier that in Figures 3a, 6 and 8, experimental results, at resonance of the (1,1) mode, fell below the theoretical pressure coefficient,  $C_p$ , by about 8% for a half amplitude of oscillation,  $\epsilon=8.0^\circ$ . A series of additional experiments was conducted to measure the amplitude of the (1,1) mode at resonance in terms of,  $C_p = \Delta P / \rho \epsilon \omega^2 a^2$ , for various angles,  $\epsilon$ . The purposes of this work were to find (a) the response,  $C_p$ , for the limit of zero angle,  $\epsilon$ , and (b) the dependence of  $C_p$  on  $\epsilon$  (the non-linear effects). The results of these experiments for both water and the silicone oil are shown in Figure 11. The ordinate in the figure is a normalized pressure coefficient,  $C_p/0.17398$ , which is equal to unity for the (1,1) mode at resonance (Section 2.2, equation 2.11a). The lines shown are best fit to the data points in the least squares sense, all data points being given equal weight. Error bars are statistical only

Figure 11. Response at resonance of (1,1) mode for various  $\epsilon$ .  
 $C_p = \Delta p / \rho \epsilon \omega^2 a^2$ ; linear theory gives  $C_p / 0.17398 = 1.0$   
for peak response of (1,1) mode. Error bars are statistical ones based  
on the scatter in each of the quantities  $\Delta p$ ,  $\epsilon$ ,  $\omega$  and  $a$ .  $\circ$   
water (0.94 cs);  $\bullet$ , oil (5.3 cs); — best fit least squares lines.  
Probe dissipation corrections have not been applied; experiments at  $\epsilon = 7.9^\circ$   
show results for water should be raised 0.9%, for oil 3.1%.

RESPONSE, AT RESONANCE  $\equiv$  (1,1) MODE



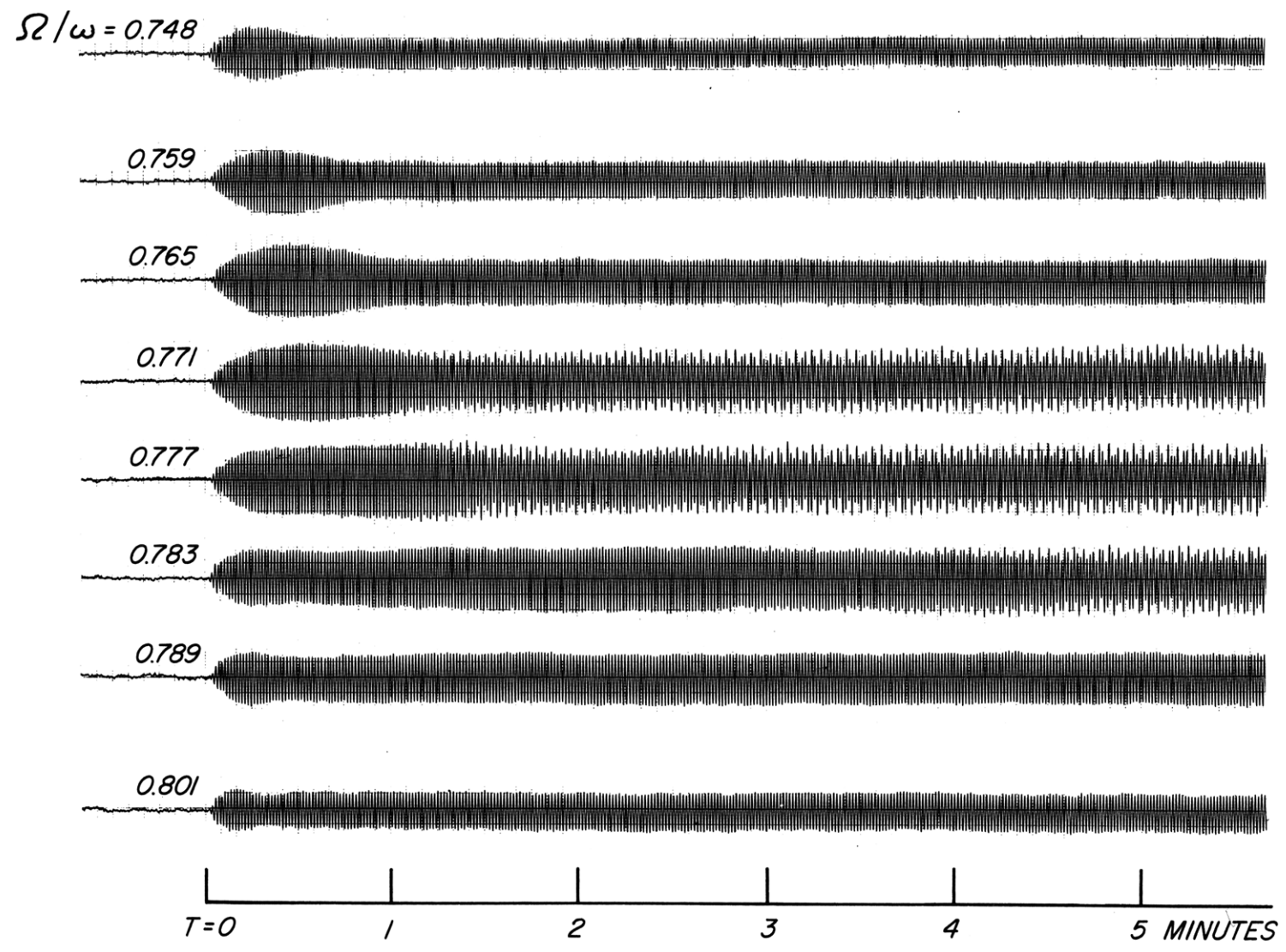
based on the scatter of the elements of  $C_p$  (Chapter VI). It is important to point out that the data points do not include a correction due to dissipation by the probe used to measure the response. The correction for the water results (Section 6.4) is 0.9% and for the oil results 3.1%. These corrections bring the two lines nearly into coincidence, the response for the oil remaining slightly below the response for the water, at  $\epsilon=0$ . Calculation of the dissipation in the interior for the (1,1) mode gives a 5% loss for water at  $\epsilon=0$ , which is slightly more than the experimental results of Figure 11 show. This correction does give an estimate of the error bars of the linear theory; we must be cautious in comparing the experimental results with linear theory at this level of precision.

#### 2.6.5 Large amplitude results; (1,1) mode

At a half amplitude of oscillation  $\epsilon=20^\circ$  and the probe tip located at  $Z=0$ , the oscillation drive was "turned on" for  $\Omega/\omega$  near the (1,1) resonance. Pressure traces for a sequence of  $\Omega/\omega$  values near (1,1) resonance are shown in Figure 12. In almost all traces at this large amplitude an overshoot of the equilibrium value occurs in a rather extended transient stage. In the record  $\Omega/\omega=0.777$  and those adjacent to it a persistence of some additional frequency components in the response is observed. This frequency content is displayed in a power spectrum of the fluid response shown in Figure 13. The power spectra were calculated from a digital record of the steady state pressure response shown in Figure 12.

Figure 12. Time histories of pressure response for various  $\Omega/\omega$  near resonance of (1,1) mode. For  $T < 0$ , fluid is rotating at a constant rate,  $\Omega$  radians/sec; at  $T=0$  oscillation is "turned on" at  $\epsilon = 20.3^\circ$ . In almost all traces at this large amplitude an "overshoot" of the steady state amplitude is observed in the transient state. For traces corresponding to  $\Omega/\omega = 0.771, 0.777$  and  $0.783$  additional frequencies of response are observed.

TIME HISTORIES  $\equiv Z=0, \epsilon=20^\circ$



A discussion of the digital data acquisition system and the appropriate data conversions for the power spectral calculation is given by Rossby (1966).

The central response peak in the figure is the (1,1) mode; the peak to the left corresponds to the (5,1) mode. The peaks to the right in the response spectrum are probably due to power in the drive as seen by the local peaks in the oscillation drive spectrum.

## 2.7 Transient response of the sphere

### 2.7.1 Decay at resonance

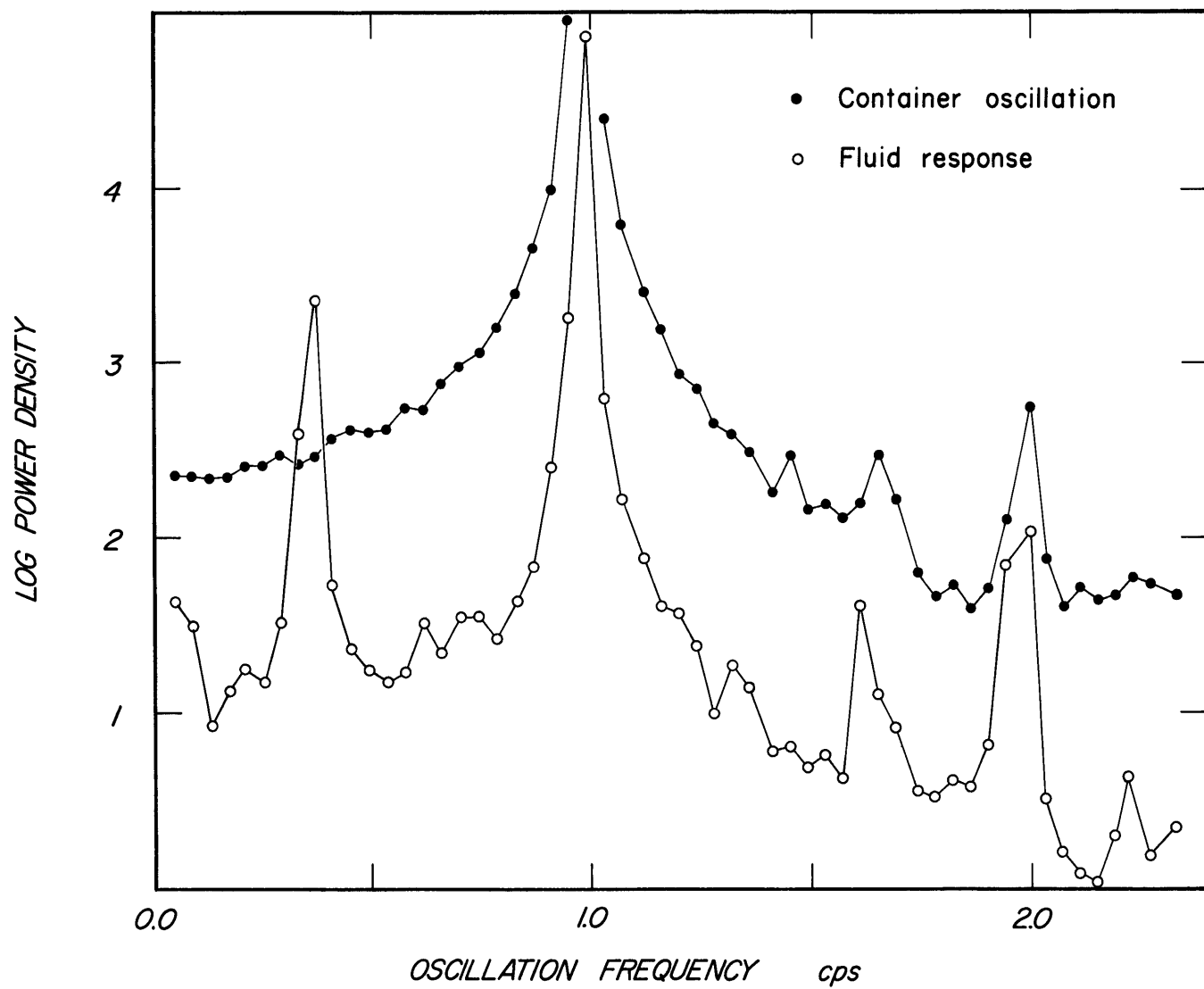
It was suggested by Greenspan that the  $Q$  of the modes be measured by observing the decay at resonance. This decay is, however, not a simple one as is shown in Figure 14.

Successive peak amplitudes of the pressure traces for the decay of the (1,1) mode are plotted logarithmically against the corresponding oscillation number counted from the time at which the drive was "turned off." A definite "beating" in the decay is observed in both the water and oil results; the beat amplitude is greater for larger viscosity. Apparently, then, in our system of many modes during free decay some of the energy in the (1,1) mode is given up to other modes. The decay is similar to a mechanical system which has many normal modes. Consider, for example, a multiple mass-spring oscillator of several masses and springs connected in series. If the springs have force constants

Figure 13. Power density spectra of both the fluid response ("h<sub>0</sub>sh" portion of the traces of figure 12) and the container oscillation at large amplitude ( $\epsilon = 20.3^\circ$ ). Central fluid response peak is the (1, 1) mode; peak to the left corresponds to the (5, 1) mode; peaks to the right are apparently due to excitation at additional frequencies as shown by the container oscillation spectrum.



POWER DENSITY SPECTRA  $\Omega / 2\pi = 0.769$  cps,  $Z = 0$ ,  $\epsilon = 20.3^\circ$



per unit mass of unity and the displacement of the  $i^{\text{th}}$  mass is  $X_i$ , then a typical equation of the chain is

$$\ddot{X}_i = X_{i-1} - 2X_i + X_{i+1}$$

The normal modes of this system can be found by expressing the displacement of the  $k^{\text{th}}$  mass as

$$X_k = \cos p k \cos \omega t$$

in the previous expression. The possible normal modes are determined from the resulting frequency equation

$$\omega = 2 \sin p/2$$

by specifying the displacement of one of the masses in the chain.

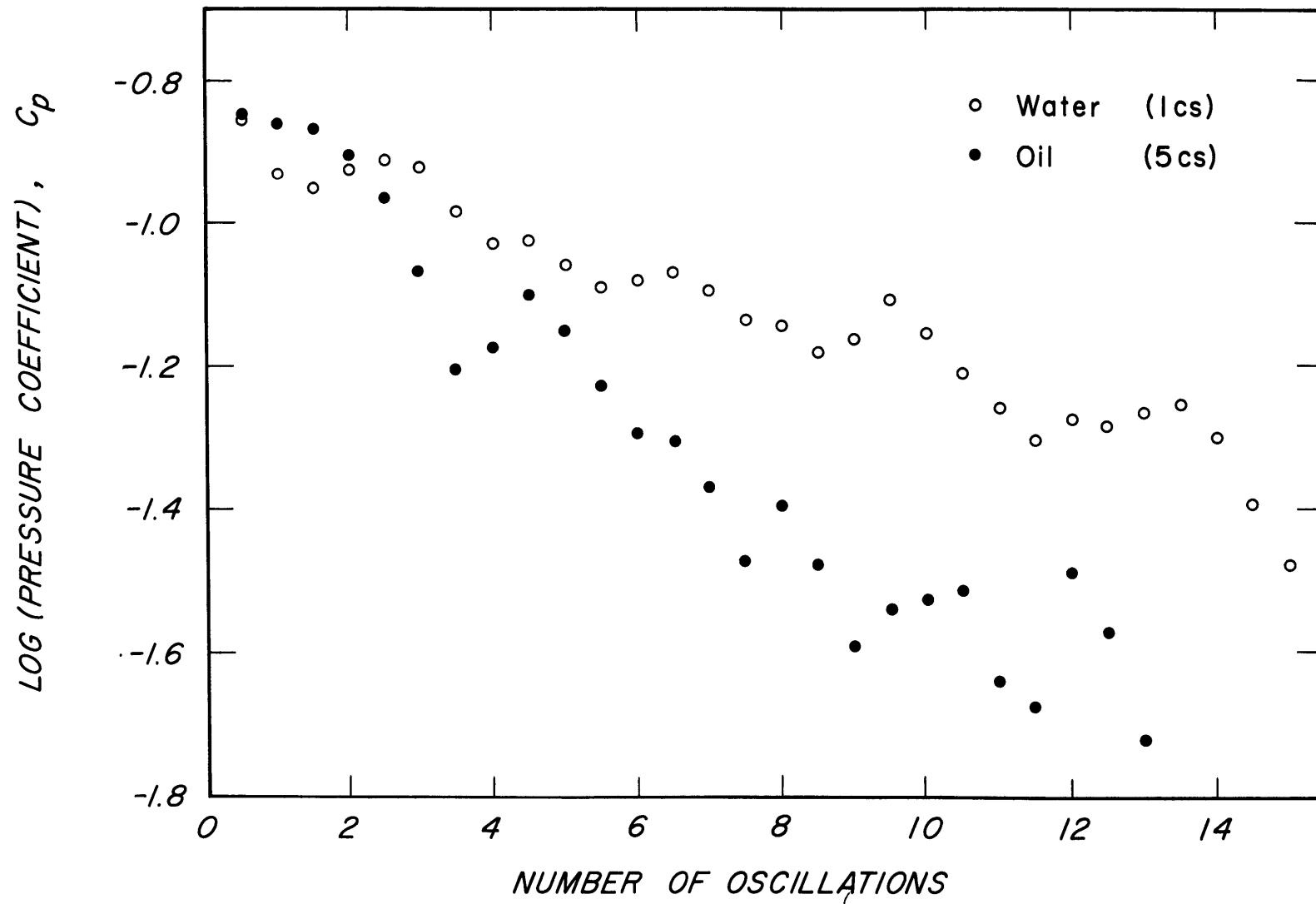
A particular mode  $\omega = 2 \sin \frac{5\pi}{18}$ , was selected for a chain of 10 masses and 9 springs and the normal mode amplitudes were used as the initial displacement distribution among the 10 masses for the following transient problem. One of the end masses was connected to a dashpot so that the equation of motion of this mass was given by

$$\ddot{X}_N = X_{N-1} - X_N - d \dot{X}_N$$

where  $d$  is the damping coefficient per unit mass. The logarithm of the displacement of the first mass in the chain as a function

Figure 14. Amplitude decay at resonance of the (  $1,1$  ) mode.  $\circ$  water (  $0.94 \text{ cs}$  );  $\bullet$  silicone oil (  $5.3 \text{ cs}$  ). "Beating", shown here, is observed in all decay records; the beat amplitude is larger for more viscous fluids.

DECAY AT RESONANCE  $\equiv$  (1,1) MODE,  $Z=0$ ,  $\epsilon=8.0^\circ$



of the number of oscillations since  $t=0$  is shown in Figure 15 for two damping coefficients. A pronounced beating, similar to that for the (1,1) mode of Figure 14 is obvious.

### 2.7.2 Summary of decay rates and Q's for the sphere

The somewhat wavy decay for the (1,1) mode shown in Figure 15 was typical of all the observed decays for the (2,1), (3,1) and (4,1) modes, the amplitude of the wave being greater for the more complex modes. Decay rates were estimated, however, from best fit (by eye) straight lines to the semi-log plots. These decay rates in units of  $a / (v\omega)^k$ , as well as theoretical ones, are tabulated in the first two columns of Table 3. The numbers in parentheses are estimates of statistical errors only.

The Q for a mode, as defined in Section 2.2, can be calculated from the decay rates as,

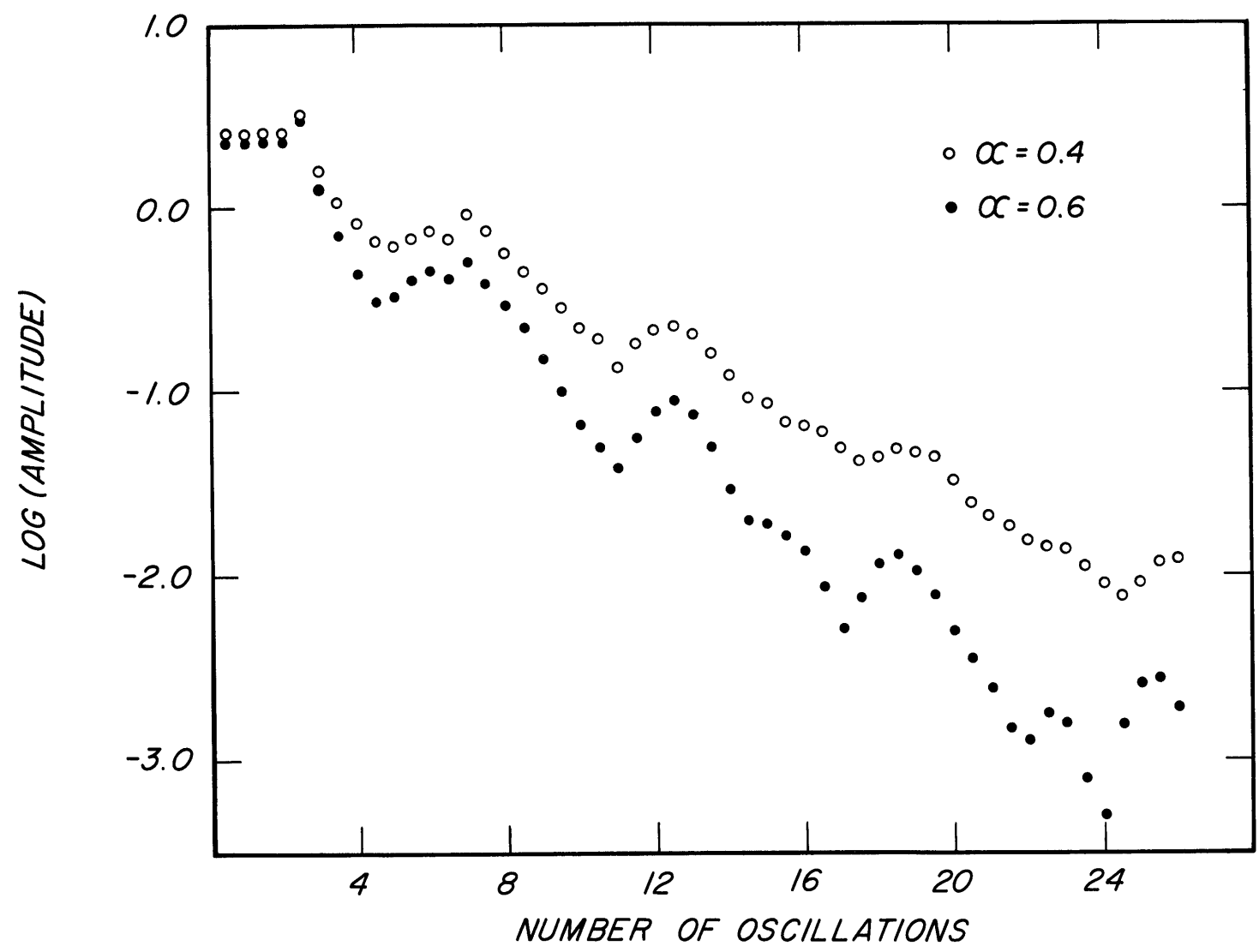
$$2Q = \frac{\text{oscillation rate}}{\text{decay rate}}$$

The experimental Q's as calculated from the decay data are shown in column 3. In addition, the Q measured from the half power points of the amplitude spectra and the 45° lines of the phase spectra are given in columns 4 and 5. The elements of column 6 are the theoretical Q's found from the decay rates of column 2.

The discrepancy in the values of Q in the more complex modes as found by the half power and 45° phase methods is almost certainly due to the distortion of the response circle by adjacent modes

Figure 15. Amplitude decay at resonance of one mass element of a series ten mass-nine spring oscillator which was free at one end of the chain and viscously coupled to a dashpot at the other.  $d$  is a damping coefficient.

DECAY AT RESONANCE  $\Rightarrow$  MULTIPLE MASS-SPRING OSCILLATOR



as discussed in some detail in Section 2.4. The generally lower experimental values of  $Q$  as compared to the theoretical ones must be explained by reference to a mode taken by itself. Any explanation for a lower value of  $Q$  for a single mode is probably related to the increasing loss in amplitude at resonance of the more complex modes (Figure 3a). It is useful to think of this loss in terms of the change in the amplitude vector, in the complex plane, for a fixed frequency  $f$ , say. If the losses referred to above are entirely changes in length of the amplitude vector, then no change in  $Q$  of the smaller response circle will be found. If, however, there is also a change in direction of the amplitude vector i.e., a change in phase for the fixed frequency  $f$ , then a decrease in  $Q$  will always result. Effectively what has apparently happened is that more frequency points have been crowded into the same region between half power or  $45^\circ$  phase and resonance on the new reduced response circle.

## 2.8 Visual Studies

The visual studies discussed in this section divide into two parts. The first part is concerned with the observations of the interior flow; the second part deals with boundary layer structure. All these observations are for the (1,1) mode.

### 2.8.1 Interior flow

A suspension of aluminum flakes, which permitted the passage of a beam of light right through the sphere, followed the



Table 3. Decay rates and Q's for the  $(n, 1)$  family of modes;  $n = 1, 2, 3, 4$ .  
Decay rates are expressed in units of  $a / (\nu\omega)^2$ . Experimental  
Q's derived both directly from the decay times and from the half power and  
 $45^\circ$  phase locations of the spectral data.

MODE	DECAY RATES UNITS OF $q/(\gamma\omega)^{1/2}$		Q'S			
	EXPERIMENT	THEORY	DECAY	HALF POWER	45° PHASE	THEORY
(1,1)	3.17 (0.06)	2.96	40.3 (0.8)	42.6 (1.2)	43.8 (1.2)	43.3
(2,1)	4.95 (0.15)	4.80	25.9 (0.8)	23.3 (0.7)	23.1 (0.7)	26.7
(3,1)	7.88 (0.32)	6.56	16.3 (0.6)	14.9 (0.3)	17.2 (0.9)	19.5
(4,1)	13.02 (1.04)	8.31	9.9 (0.8)	9.5 (0.7)	14.4 (1.0)	15.4

fluid particle motions. The aluminum particles were made visible by reflected light.

Plate 1 shows a **cross** section of the sphere; the plane of light contains the axis of rotation. The bands of the edges of both photographs outline regions where the secondary flow (figure 9) undergoes a rapid change with radius. A second region of change in the radial structure of this zone is apparent in the lower photograph for a slightly larger half-amplitude of oscillation angle,  $\epsilon$ .

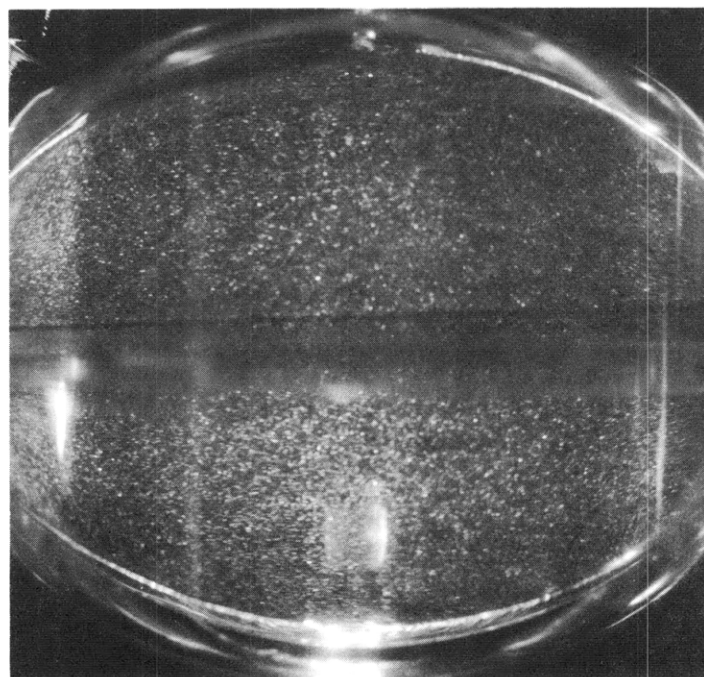
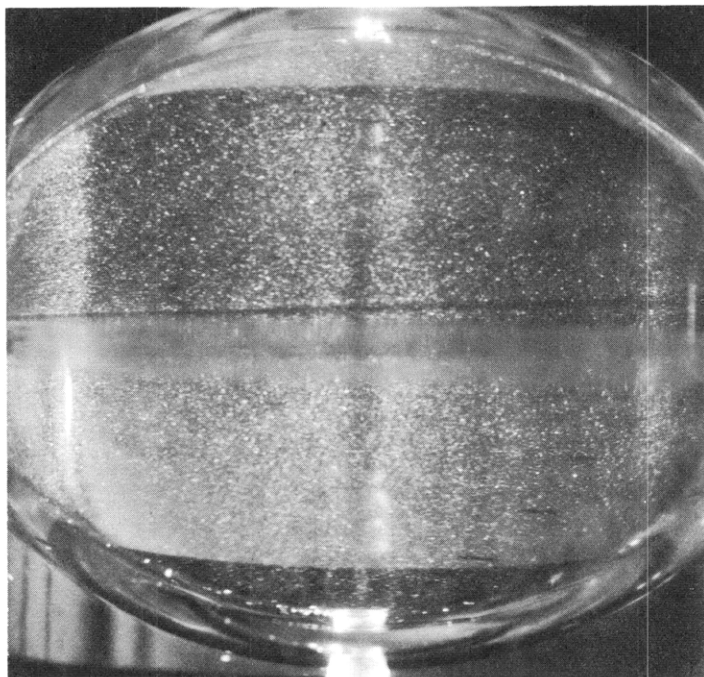
The vertical zones of plate 1 are more well developed in plate 2 where the oscillation half-amplitude has been increased ( $\epsilon = 14.2^\circ$ ). This plate clearly shows how the secondary zonal flow can be used as a marker for the primary oscillatory flow. The two photographs were taken approximately one half oscillation period apart.

The complex pressure traces of figure 11 near  $\Omega/\omega = 0.777$  for  $\epsilon = 20^\circ$  suggested that the flow at this rotation speed might be rather complex. The upper photograph of plate 3 for  $\Omega/\omega = 0.785$ ,  $\epsilon = 22.2^\circ$  clearly supports this suggestion; it is typical of the flow near  $\Omega/\omega = 0.777$  for this large amplitude. The lower photograph is for the same  $\epsilon$  as the upper but for a slightly increased frequency ratio,  $\Omega/\omega = 0.789$ . The complex response of upper photograph has almost disappeared; the diagonal zones, most apparent in the lower right corner of the photograph, are probably the characteristic surfaces of the flow, found in the

$$\epsilon = 8.0^\circ ; \Omega/\omega = 0.766$$

Plate 1. Secondary flow; (1,1) mode

$$\epsilon = 11.3^\circ ; \Omega/\omega = 0.768$$



equation 2.6 of Section 2.1 by ignoring the term  $\frac{1}{R} \frac{d^2}{dR^2}$  (large  $R$  approximation). These surfaces only appear, however, in transient states associated with changes in the rotation speed,  $\Omega$ .

### 3.8.2 Boundary layer structure

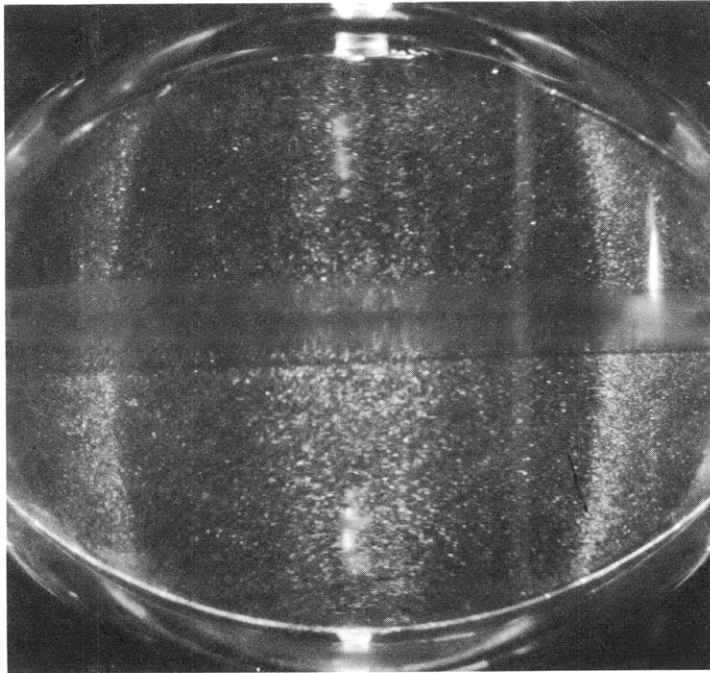
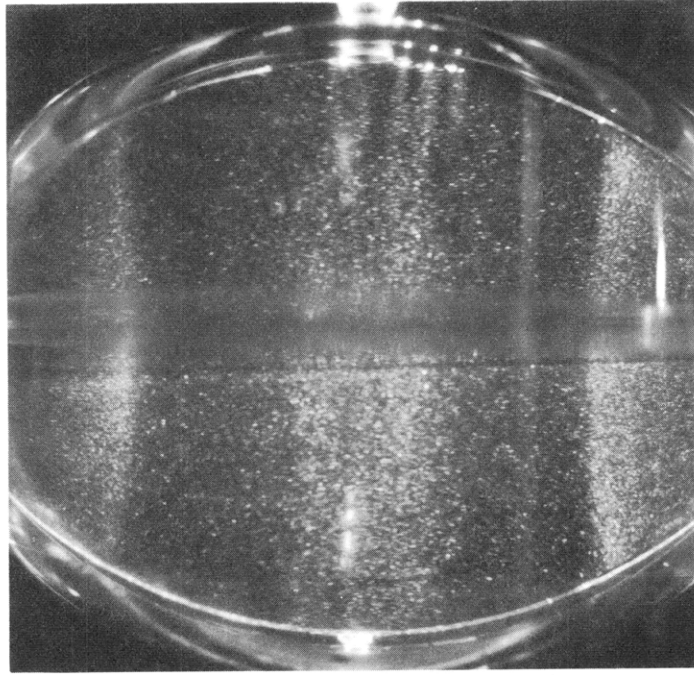
The concentration of aluminum particles was increased to a level sufficient to allow only a short penetration depth of light, so that only the flow near the surface of the sphere was then visible. Plate 4 shows these boundary regions for the (1,1) mode as revealed by this technique. Of particular interest was the "roll structure" which can be seen in the photograph as a series of light and dark bands. This structure was studied in some detail for another transparent sphere of larger diameter and less precise construction (Polar diameter = 31.6 cm; equatorial diameter 29.6 cm). The properties of the roll structure for half-amplitude of oscillation angles,  $5^\circ < \epsilon < 15^\circ$ , are summarized as follows:

1. At small excitation angles,  $\epsilon$ , the existence of the structure is sensitive to  $\Omega/\omega$ ; at large angles,  $\epsilon$ , this sensitivity is greatly reduced.
2. The time of establishment of the structure from the initiation of the excitation drive is longer for smaller angles; it varied from 1/2 minute to 1/5 minute for  $5^\circ < \epsilon < 15^\circ$ .
3. The wave length of the structure was approximately 1/2 cm and was insensitive to the angle  $\epsilon$ .
4. The roll structure was bounded at high latitudes by a laminar region. This maximum latitude extent

$$\epsilon = 14.0^\circ ; \Omega/\omega = 0.763$$

Plate 2. Secondary flow; (1,1) mode

as above, 1/2 oscillation period later.





of the roll structure,  $\kappa^0$ , was regularly related to the excitation angle  $\epsilon$ , as shown in Figure 16.

The experimental points were found by direct observation of this maximum latitude extent of the roll structure for a series of excitation angles,  $\epsilon$ .

These observations were facilitated by a rotating and oscillating prism (Hide, 1958) and mirror arrangement which removed all of the rotation of the container.

There is a strong suggestion in the results of Figure 16 that the boundary between the roll structure and the laminar region represents some critical velocity which is reached at higher latitudes for larger excitation angles. We are led, therefore, to calculate the difference in velocity between the container wall and the fluid next to it. For the (1,1) mode the components of velocity in the eastward (x) direction and the southward (y) direction relative to the container wall are

$$V_x = \epsilon \omega a (\sin \theta - 0.531 \sin 2\theta \cos \theta)$$

$$V_y = \epsilon \omega a (0.696 \sin 2\theta)$$

Where  $\theta$  is the co-latitude, and  $\epsilon$  is in radians.

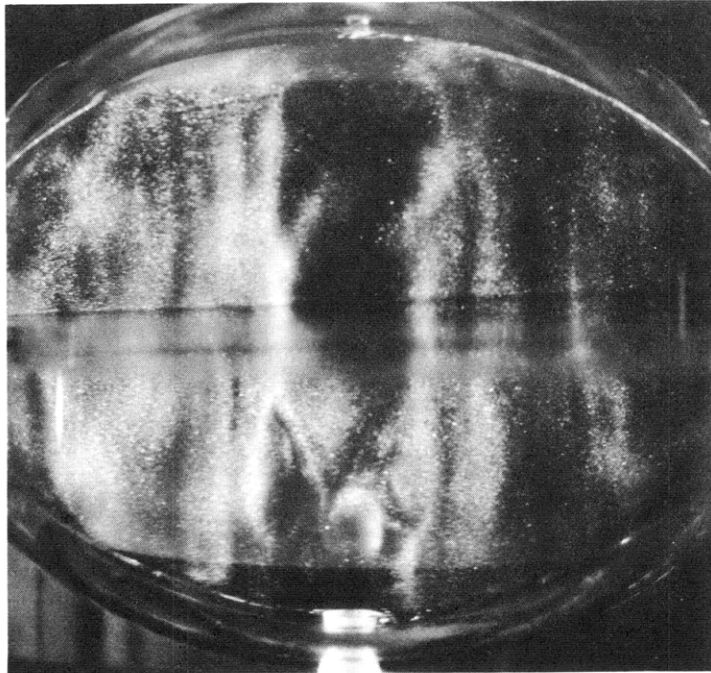
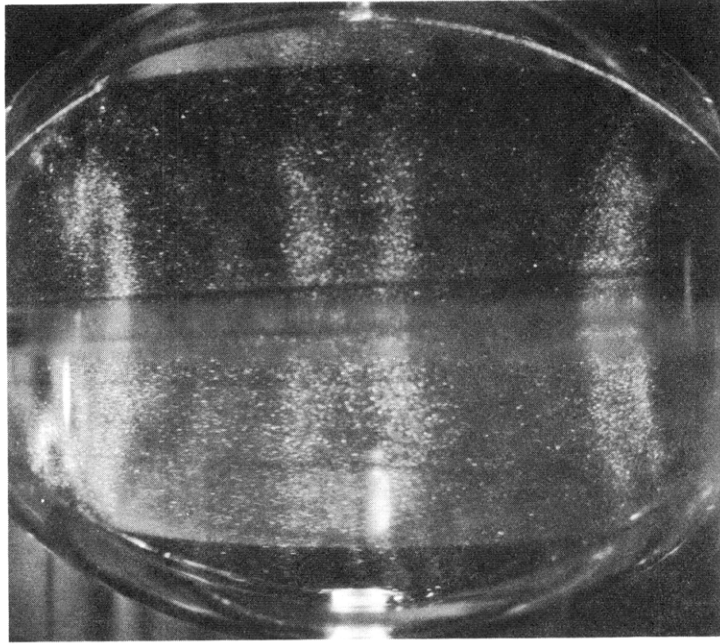
The values of  $V_x$  and  $V_y$  for each pair of  $(\kappa=90^\circ-\theta, \epsilon)$  values are calculated. The relative azimuthal velocity,  $V_x$  seems fairly constant; its mean value is found to be  $9.2 \pm 0.8$  cm/sec. A line

$V_x^* = 9.2$  cm/sec., shown in Figure 16, graphically illustrates

$$\epsilon = 22.2^\circ ; \Omega/\omega = 0.785 \text{ (steady state)}$$

Plate 3. Large amplitude response; (1,1) mode

$$\epsilon = 22.2^\circ ; \Omega/\omega = 0.787 \text{ (transient state)}$$



this tendency of the data to correspond to a constant critical azimuthal velocity. The region to the right of the line  $V_x = V_x^*$  is one of azimuthal velocity greater than  $V_x^*$  cm/sec. A line of constant relative meridional velocity,  $V_y = V_x^*$ , shows that a critical value for the meridional velocity would be larger than that for the azimuthal velocity.

We would expect that a critical velocity in either the meridional or azimuthal direction would be latitude dependent through both the ratio of these velocities,  $V_y/V_x$  and a measure of the boundary layer thickness,  $\sqrt{2} \cos \theta / \omega$ . Since a critical velocity would scale as  $\sqrt{\omega \nu}$ , a reasonable functional dependence for such a critical velocity is

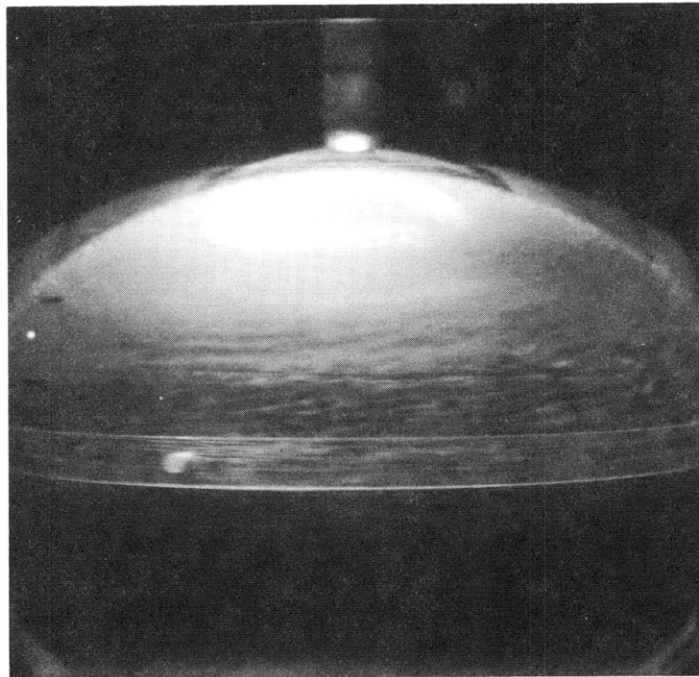
$$V^{*2} = \omega \nu F(\sqrt{2} \cos \theta / \omega, V_y/V_x)$$

A suggested interpretation for the data points of Figure 16 is that the function F for the azimuthal velocity is a slowly varying one; the value  $V_x^*/\sqrt{\omega \nu}$  can then be interpreted as a critical Reynolds number. For  $\omega=6.2$  rad/sec. and  $\nu=0.94$  cs we find

$$\frac{V_x^*}{\sqrt{\omega \nu}} = 38 \pm 3.$$

Plate 4. Boundary layer roll structure; (1,1) mode.

$$\epsilon = 14.8^\circ ; \Omega/\omega = 0.755$$



CHAPTER III

Modes of Spherical Shells

<u>Section</u>		<u>Page</u>
3.1	Introduction	63
3.2	A modal frequency estimate	65
3.3	Response of spherical shells	71
3.4	Variational principle	73
3.5	Visual studies	75

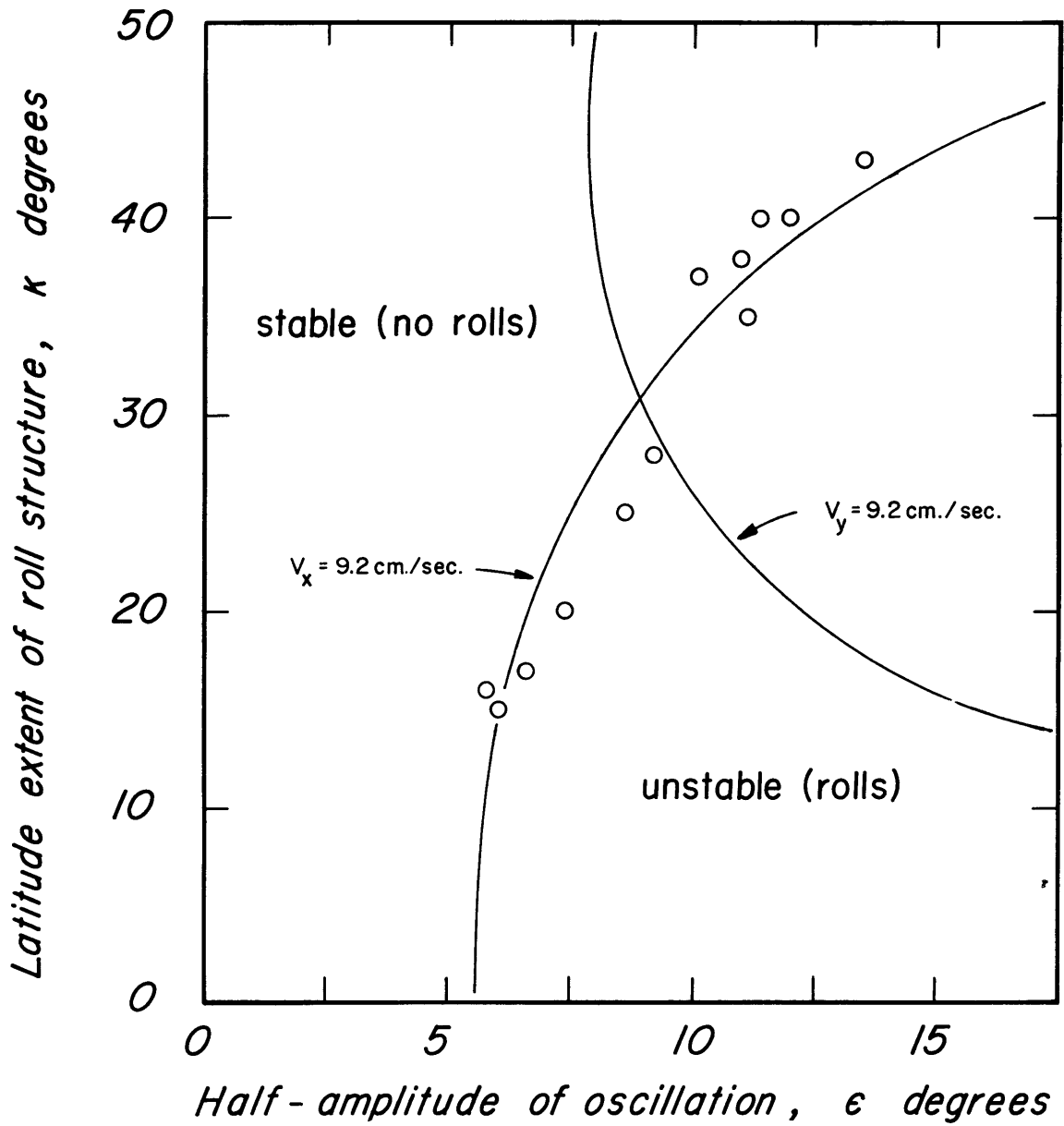
3.1 Introduction

It was pointed out in Chapter I that the vertical component of coriolis force must be retained in the equations of motion for a rotating weakly stratified ( $N/2\Omega \ll 1$ ) fluid. There are places on the earth where this condition exists, namely the Ross Sea (Longuet-Higgins, 1966) and portions of the Great Lakes (Eckart, 1960). A first step, as given by Longuet-Higgins, (1966) in the solution of the problem of a weakly stratified fluid, is the case of a uniform fluid. He has constructed a model of a uniform fluid contained between rigid spherical shells; because planetary waves have very little change in surface elevation, solutions obtained for this model, with periods less than the half pendulum day, would correspond to planetary waves. With this model he has looked for a polynomial series solution to the Poincaré Equation (Chapter II) in order to satisfy the boundary condition that the normal component of velocity vanish at both

Figure 16. Latitude extent of boundary layer roll structure as a function of oscillation half-amplitude for the (1,1) mode. Each data point corresponds to an observed greatest latitude of the roll structure for a fixed oscillation angle. The lines shown are loci of constant relative azimuthal ( $v_x$ ) and meridional ( $v_y$ ) velocity as calculated from linear theory.



BOUNDARY LAYER ROLLS  $\equiv$  (1,1) MODE



the inner and outer spherical surface. It happens that there are insufficient non-singular solutions to form a series which satisfies boundary conditions. He suggested that there may be discontinuous solutions or that solutions may exist which are not valid throughout the shell.

Modes of oscillation of this latter type have apparently been found by Stern (1963), for an equatorial ocean. The latitude extent is  $O(hR)^{1/2}$  where  $h$  is the ocean depth and  $R$  the mean radius of the shell; the periods are very long,  $O(R/h)$ . He assumed that, although the adiabatic Brunt-Vaisala frequency was possibly larger than the inertial frequency, the time scale of the motion was sufficiently long compared to, at least, the thermal diffusion time so that the fluid would essentially not feel the density gradient. Long period oscillations such as these are a lower limit in period of the oscillations considered in the experiments discussed here.

It was of considerable interest, then, to look for axisymmetric modes in a spherical shell of fluid. The following sections discuss experiments concerned with the modes of a shell of fluid, formed by centering an inner sphere in the spherical cavity of the previous experiments.

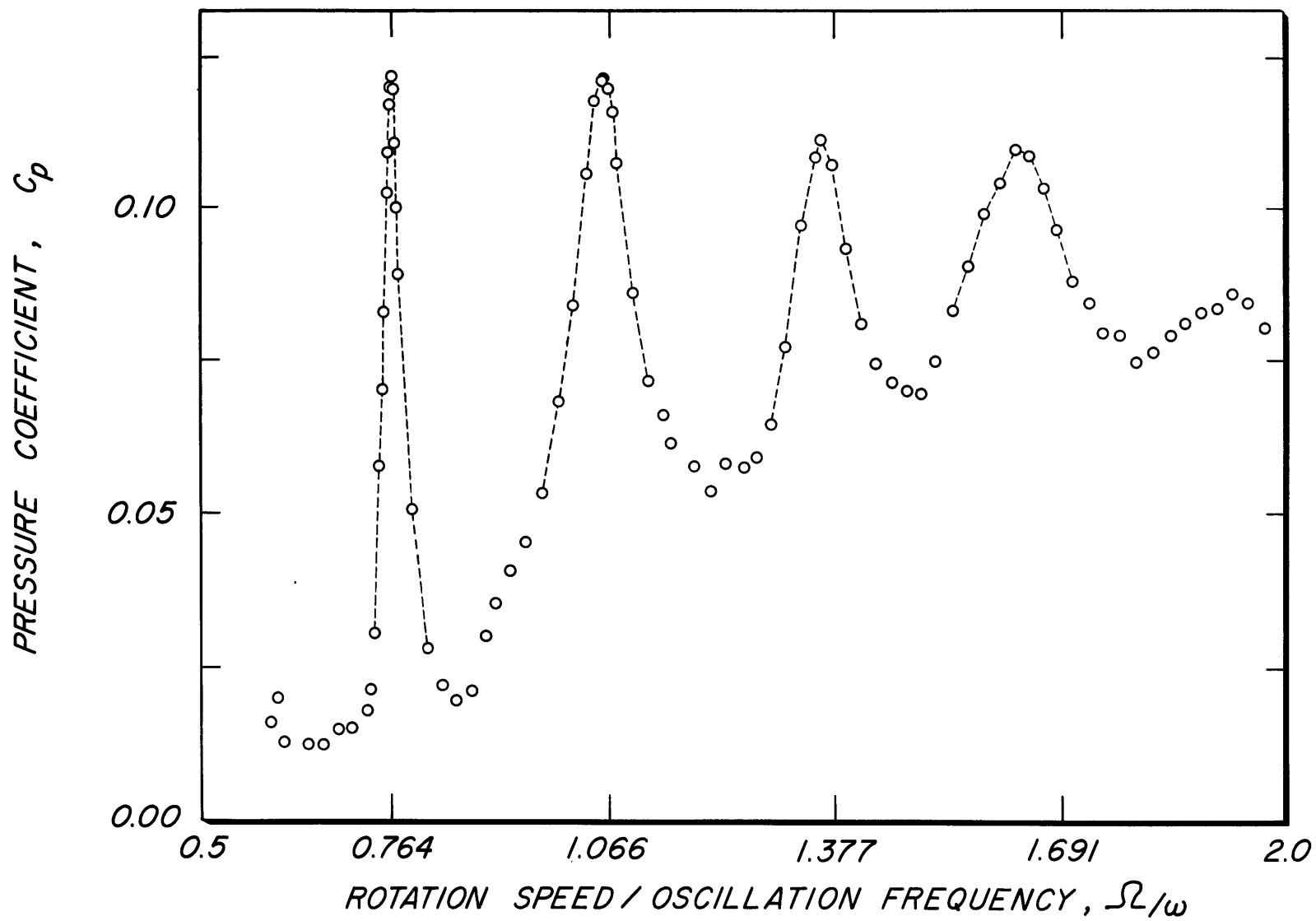
### 3.2 A modal frequency estimate for the spherical shell.

An estimate of the resonant frequency ratios for the spherical shell of fluid can be obtained by going back to the Poincaré equation

$$R \frac{\partial}{\partial R} \left( \frac{1}{R} \frac{\partial \psi}{\partial R} \right) - \lambda^2 \frac{\partial^2 \psi}{\partial z^2} = 0$$

Figure 17. Amplitude response of a spherical shell of fluid;  $b/a = 0.25$ ;  
probe tip at  $z = 0.26a$  ;  $\epsilon = 8.0^\circ$  ; water;  $C_p = \Delta P / \rho \epsilon \omega^2 a^2$ .  
Abscissae are the resonant locations,  $\sqrt{z} / \omega$  , for the first four members  
of the  $(n, 1)$  family of modes for the sphere.

AMPLITUDE  $\equiv$   $b/a = 0.25$ ,  $Z = 0.26a$ ,  $\epsilon = 8.0^\circ$



of Chapter II. Multiplication by  $\psi$  and integration by parts over  $\tau$ , the volume of the sphere, leads to the relation

$$\lambda^2 = \phi_z / \phi_R \quad 3.1$$

where we have put

$$\phi_z = \int_{\tau} \frac{1}{2} \rho w^2 d\tau$$

and

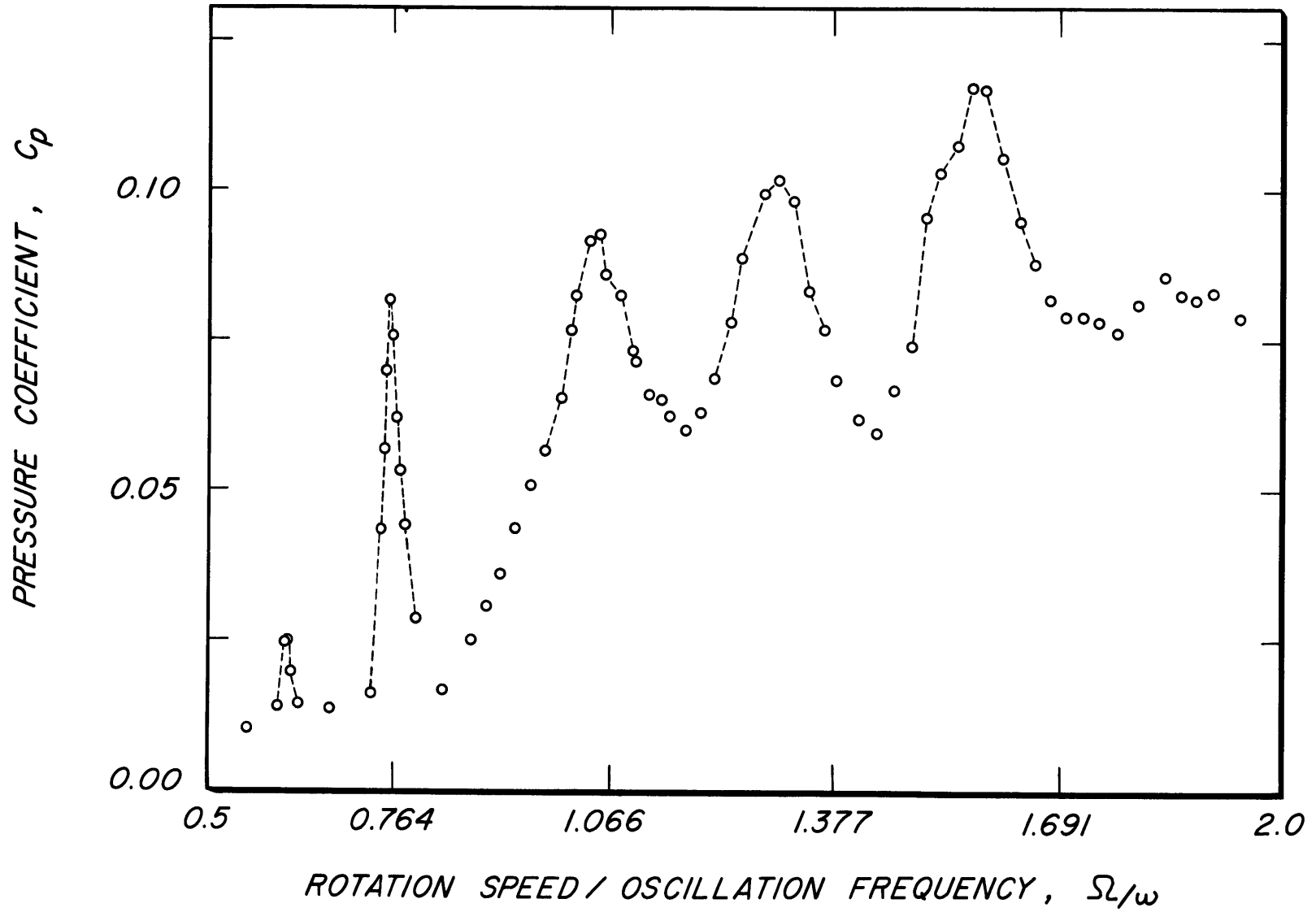
$$\phi_R = \int_{\tau} \frac{1}{2} \rho u^2 d\tau$$

$\phi_z$  is the total kinetic of the vertical motion;  $\phi_R$  is the total kinetic energy of the radial motion.

Since the result 3.1 is independent of the geometry of the boundary, it is precisely true for both the sphere and spherical shell of fluid. An estimate of  $\lambda^2$  for a shell of fluid is obtained by assuming that solidifying the portion of the fluid contained in a sphere of radius  $b$  ( $\ll a$ ) would not essentially alter the flow outside this inner sphere. The estimate of  $\lambda^2$  for the shell is then the ratio  $\phi_z / \phi_R$  for the fluid remaining in the shell.

Figure 18. Amplitude response of a spherical shell of fluid;  $b/a = 0.35$ ;  
probe tip at  $z = 0.36a$  ;  $\epsilon = 7.9^\circ$  ; water;  $C_p = \Delta p / \rho \omega^2 a^2$  .  
Abcissae are the resonant locations,  $\omega/\omega_0$  , for the first four members  
of the (  $n, l$  ) family of modes for the sphere.

AMPLITUDE  $\equiv$   $b/a = 0.35, Z = 0.36a, \epsilon = 7.9^\circ$



For example, we found earlier for the (1,1) mode

$$\psi_{1,1}(R, z) = R^2 z (1 - R^2 - z^2)$$

Within a sphere of radius  $g$

$$\phi_z(g) = 4(63g^5 - 126g^7 + 71g^9),$$

$$\phi_R(g) = 126g^5 - 252g^7 + 150g^9.$$

For

$$\frac{\phi_z(1)}{\phi_R(1)} = \lambda^2 = 4/3 \quad \text{which is}$$

the exact value for the sphere. Estimates of  $\lambda^2$  and the corresponding ratios  $\mathcal{J}/\omega$  are given below

$$g = b/a \quad \lambda_g^2 = \frac{\phi_z(1) - \phi_z(g)}{\phi_R(1) - \phi_R(g)} \quad \mathcal{J}/\omega$$

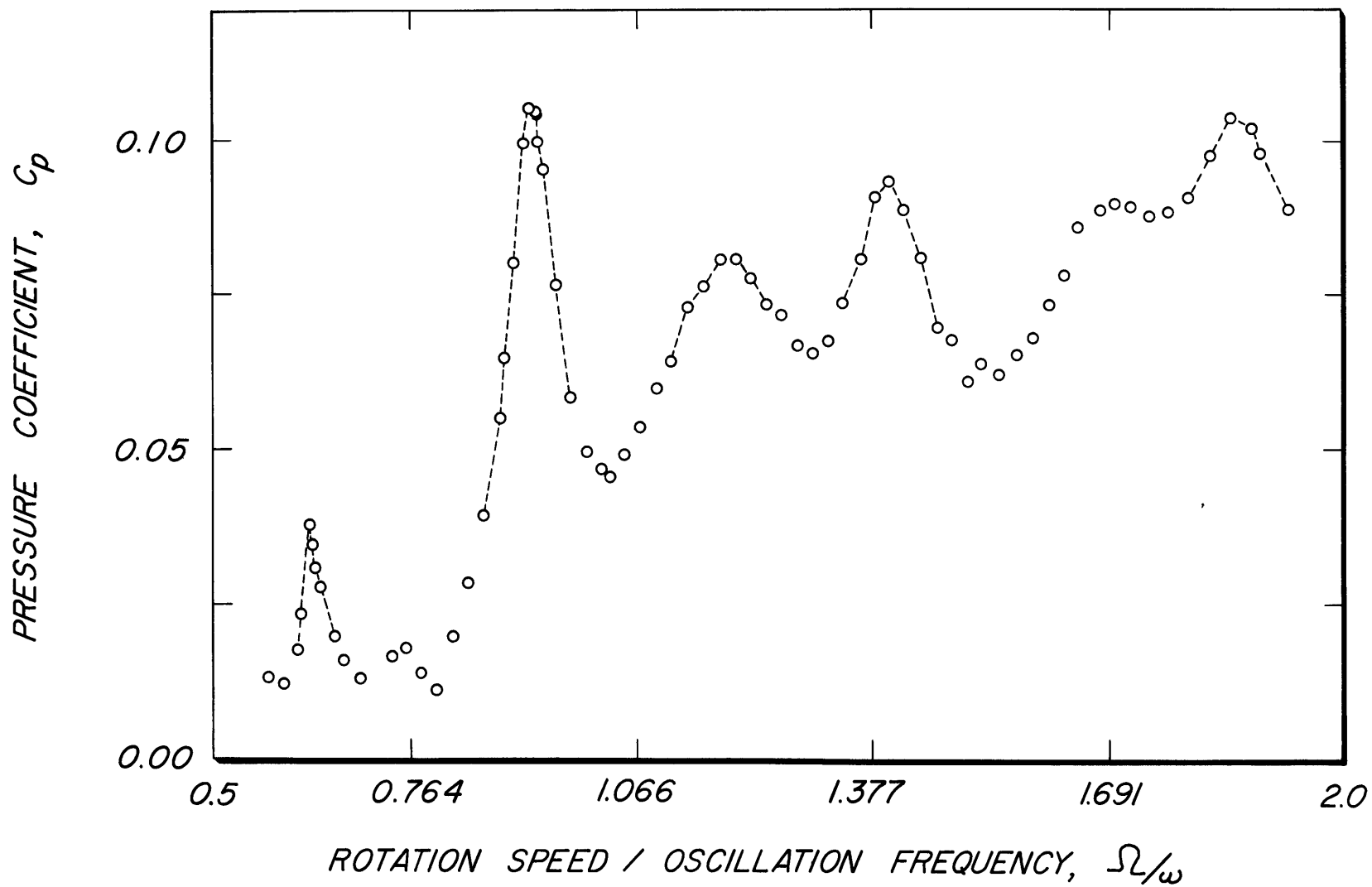
0	1.33	0.764
1/4	1.33	0.764
1/2	1.27	0.753

According to this estimate  $\mathcal{J}/\omega$  for the (1,1) mode of the sphere decreases very slowly with increasing  $g$ , which, in this



Figure 19. Amplitude response of a spherical shell of fluid;  $b/a = 0.51$ ;  
probe tip at  $z = 0.53a$  ;  $\epsilon = 7.9^\circ$  ; water;  $C_p =$   
 $\Delta P / \rho c \omega^2 a^2$ ; Abscissae are the resonant locations,  $\Omega/\omega$  , for the first  
four members of the  $(n, 1)$  family of modes for the sphere.

AMPLITUDE  $\equiv b/a = 0.51, Z = 0.53a, \epsilon = 7.9^\circ$



estimate, is the ratio of the diameter of the inner sphere to that of the outer sphere. That this is indeed the case is seen in the experimental results for spherical shells of fluid in the following section.

### 3.3 Response of spherical shells

The spherical shell assembly (sphere and centered inner sphere) was filled with fluid and rotated as

$$\Omega(t) = \Omega + \epsilon \omega \cos \omega t .$$

$\Omega$  was adjusted over several values while  $\omega$  remained constant such that ( $0.5 < \Omega/\omega < 2.0$  ). The pressure probe was lowered on the axis until the tip was just clear of the "north pole" of the inner sphere. The diameter of the sphere is  $2a$  cm; let the diameter of the inner sphere be  $2b$  cm. The amplitude response,  $C_p$ , for spherical shells  $b/a=0.254$ ,  $0.349$  and  $0.510$  is shown in Figures 17, 18, 19 respectively. In all of the figures the modes corresponding to the  $(n,1)$  family have lower values of  $\Omega/\omega$  than for the sphere. The shift in frequency is greater for larger  $b/a$ . The mode which corresponds to the  $(2,2)$  mode of the sphere is only really visible in Figure 19 for  $b/a=0.51$ , but it is noteworthy that this mode is shifted in the opposite direction to all the others. Apparently, from the arguments of Section 3.2, the percentage loss of kinetic energy

Table 4. Experimental modal frequency ratios for the sphere and spherical shells.

EXPERIMENTAL MODAL FREQUENCY RATIOS  
 SPHERE AND SPHERICAL SHELLS

b/a	(2,2)	(1,1)	(2,1)	(3,1)	(4,1)	(5,1)
0.000	0.607 (5)	0.764 (1)	1.064 (2)	1.375 (3)	1.685 (5)	
0.254 (1)	0.605 (6)	0.764 (1)	1.059 (2)	1.359 (3)	1.633 (5)	1.930 (7)
0.349 (1)	0.617 (3)	0.760 (1)	1.045 (2)	1.300 (3)	1.580 (9)	1.840(12)
0.510(13)	0.634 (3)	0.755 (6)	0.926 (2)	1.190 (3)	1.403 (5)	1.700 (7)

of horizontal motions is greater than the percentage loss of kinetic energy of vertical motions for this mode.

The (1,1) mode shows very little shift in frequency with increasing  $b/a$  but it does lose amplitude rather rapidly. The small shift which is observed is in the appropriate direction and of about the right magnitude as given by the crude energy estimates of the previous section.

The modal frequency ratios for both the sphere and the spherical shells are summarized in Table 4. The numbers in parentheses are estimates of the errors in the least significant figure of the quantity they accompany.

#### 3.4 Variational principle

An interpretation of the experimental results which is more precise than the kinetic energy arguments of Section 3.2 is found in a slightly different formulation of the eigenvalue problem. It is shown in Appendix IV that the ratio of the kinetic energy of vertical motion to the kinetic energy of radial motion is stationary when the stream function of these motions is an eigenfunction of the Poincaré problem. By adjusting trial functions in this ratio, eigenvalues can be found by locating the point where this ratio of energy integrals is stationary. Trial functions here were polynomial series with unknown coefficients; the coefficients in the series were adjusted until the ratio was stationary. The details of the technique are given in Appendix IV. It should be added that if, indeed, exact solutions to the

Table 5. Modal frequency ratios of the  $(n, l, 2)$  families  
for the sphere from the variational principle.  
Exact values from linear theory are shown in the bottom  
line.

MODAL FREQUENCY RATIOS ... SPHERE  
FROM VARIATIONAL PRINCIPLE

NUMBER OF TERMS IN SERIES	(2,2)	(1,1)	(2,1)	(3,1)	(4,1)
1		0.7638			
3	0.6023	0.7638	1.0664		
6	0.6023	0.7638	1.0664	1.3770	
10	0.6023	0.7638	1.0664	1.3770	1.6906
15	0.6023	0.7638	1.0664	1.3770	1.6906
21	0.6023	0.7637	1.0664	1.3770	1.6905
$P_{2n+2}(\frac{\omega}{2\Omega}) = 0$	0.6022	0.7638	1.0664	1.3770	1.6906



spherical shell problem do require velocity discontinuities, these would appear in the stream function as slope discontinuities. A series expansion, of relatively few terms, would apparently smooth over these kinks.

The numerical predictions for some of the modal frequency ratios for the sphere are given in Table 5. The first column gives the number of terms in the polynomial expansion; the bottom row lists the exact modal values as given by the roots of associated Legendre function. Agreement is generally quite good.

Table 6 lists the results of a series expansion for a spherical shell of ratio  $b/a=0.51$  which corresponds to the largest inner sphere used in the experiments. The bottom row gives the experimental values. The somewhat dubious convergence shown here is typical of the numerical results with the spherical shells. The general features of the experimental results are, however, preserved in the model. All modes of the  $(n,1)$  family show a decrease in the frequency ratio, from the value for the sphere which is also seen in the model. In particular the relatively small shift of the  $(1,1)$  mode in comparison to the  $(2,1)$ ,  $(3,1)$  and  $(4,1)$  modes is reproduced. Finally, the  $(2,2)$  modal frequency ratio of the model increases from its value for the sphere (0.602) to a value fairly close to the experimental one.

### 3.5 Visual studies

The interior flow for a spherical shell of fluid ( $b/a=0.51$ ) was observed directly by means of the aluminum particle suspension

Table 6. Modal frequency ratios for the spherical shell,  
 $b/a = 0.51$ , from the variational principle  
and experiments.

MODAL FREQUENCY RATIOS ... SPHERICAL SHELL  
FROM VARIATIONAL PRINCIPLE

$b/a = 0.51$

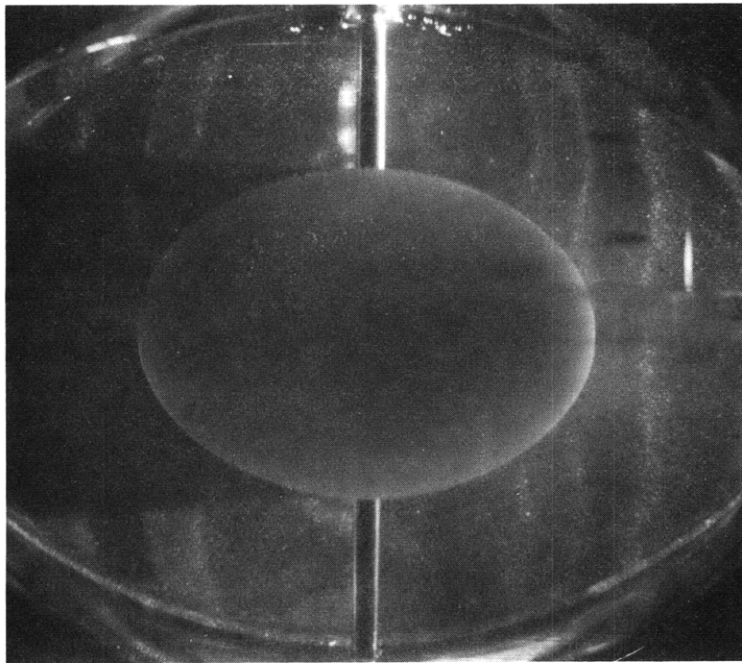
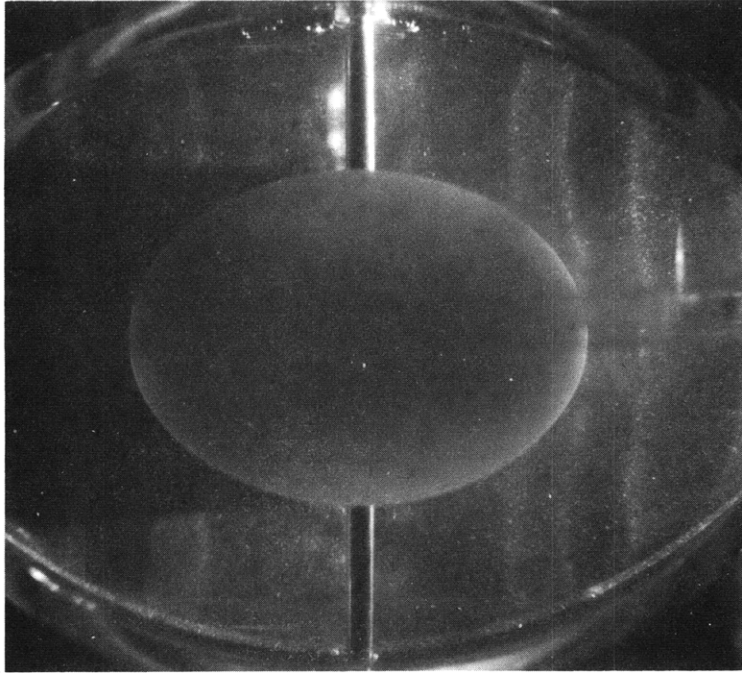
NUMBER OF TERMS IN SERIES	(2,2)	(1,1)	(2,1)	(3,1)	(4,1)
1		0.7638			
3	0.6150	0.7638	1.0039		
6	0.6235	0.7638	0.9644	1.2990	
10	0.6273	0.7637	0.9357	1.2592	1.5926
15	0.6278	0.7627	0.9210	1.2268	1.5306
21	0.6325	0.7605	0.9395	1.1905	1.4761
EXPERIMENT	0.634(3)	0.755(6)	0.926(2)	1.190(3)	1.403(5)

and flat beam of light technique discussed in Section 2.8.1. The photographs of Plate 5, taken one half oscillation period apart, show a sharp radial gradient in the secondary flow ( $\zeta=14.0^\circ$ ) for the shifted (2,2) mode. The flexing of these shear surfaces of the secondary flow clearly show the primary radial fluid oscillation.

$$\epsilon = 14.0^\circ ; \Omega/\omega = 0.625$$

Plate 5. Secondary flow for spherical shell  $b/a$   
= 0.51. "(2,2)" mode.

as above, 1/2 oscillation period later.



CHAPTER IV

Discussion of Errors

Every parameter,  $P$ , measured in the experiments may be expressed in terms of a mean value,  $P_0$  and an error,  $\alpha$ , as

$$P = P_0 + \alpha$$

The error  $\alpha$  is, in general, composed of a random part,  $\beta$ , and a nonrandom or systematic,  $\gamma$ , such that

$$\alpha = \beta + \gamma .$$

The following sections are concerned with these two sources of error in the parameter  $P$ .

4.1 Random errors,  $\beta$

In most experimental measurements a random error is the result of several independent events. For example, the measurement of time with a stopwatch depends on eye position, anticipation time, and reaction time, each of which in turn depends on even less obvious events. It can be shown from the central limit theorem (Fraser, 1958) that such a random error  $\beta$  made up of several independent components will have a normal probability density function

$$f(\beta) = \frac{1}{\sqrt{2\pi}} e^{-\beta^2/2\sigma^2}$$

with standard deviation  $\sigma$ . The mean value of the distribution has been removed.

If  $\sigma$  were known and we were given N experimental measurements  $X_1, X_2, \dots, X_n$  of P, a best estimate of P is

$$\bar{X} \pm \sigma/\sqrt{N}$$

where

$$\bar{X} = \sum_i X_i / N$$

The standard deviation,  $\sigma$ , is, however, usually not known so it must be estimated. An unbiased estimate of  $\sigma$  for N samples is

$$s = \sqrt{\frac{\sum_i (X_i - \bar{X})^2}{N-1}}$$

If we use this estimate of  $\sigma$  in the previous estimate of P we find, for N measurements

$$\bar{X} \pm \sqrt{\frac{\sum (X_i - \bar{X})^2}{N(N-1)}}$$

The error bars in the experimental results were calculated from this relationship. In variables composed of more than one measured parameter in product form, the error bars were computed as follows. Let

$$P = \prod_i P_i^{\theta_i}$$

where  $\theta_i$  may be positive or negative and i runs through the number



of measured quantities making up P. Then

$$\frac{\Delta P}{P} = \sum_i \theta_i \frac{\Delta P_i}{P_i}$$

so that for small changes in  $P_i$  the percentage error in P is the sum of the weighted percentage errors of the  $P_i$ . The error bars shown in Figure 11 were calculated in this manner where the sources were the observed pressure, calibration constant, oscillation angle, oscillation period and sphere radius.

Somewhat more empirical techniques were used for error bars in quantities such as the experimental modal frequency ratios. For each spectral peak an estimate, by eye, of extreme values of a best fit smooth curve through the data points was the error bar. Similar remarks apply to error estimates of spectral Q's.

#### 4.2 Systematic errors, $\delta$ .

Systematic errors were minimized by repeating experiments, wherever possible, under different sets of conditions. For example, spectral data was obtained over the range of  $\Omega$  by sometimes increasing and sometimes decreasing the rotation speed. If possible, parameters were measured by different techniques. Calibration experiments which involved the use of an optical

lever (200x magnification) to measure fluid level displacements, were checked with a cathetometer telescope. The oscillation angle,  $\epsilon$ , measured dynamically was checked with a static measurement. Rotation periods given by the electronic stopwatch were periodically checked with a calibrated stopwatch.

Some small systematic errors were ignored. The pressure coefficient,  $C_p$ , although a slow function of amplitude through various non-linear mechanical elements of the transducer, was computed for peak values of the spectral data. This leads to errors of the order of 3% in the lower regions of the peaks where the random errors are easily of that order. Systematic errors in  $Q$  from this source as estimated from the spectral half widths are within the random error estimates.

Finally, certain systematic errors were probably not small but were unavoidable. For example, while random errors in the decay rates as measured for complex decays of the type shown in Figure 14 can be estimated from several decays, the systematic errors remain unknown.

CHAPTER V

Summary

Some axisymmetric inertial modes of oscillation of a rotating fluid sphere have been excited by superimposing a small harmonic perturbation on the otherwise uniformly rotating fluid. The resulting exchange of fluid between the Ekman boundary layers and the interior was sufficient to set the fluid into oscillation. The oscillatory pressure difference developed between the pole and a point on the rotation axis was measured with a pressure transducer. A spectrum of several distinct amplitude peaks as a function of the ratio  $\Omega/\omega$  was found; the frequency locations of these peaks were in good agreement with those given by linear theory.

The amplitudes at resonance, however, were all significantly less than one would expect from linear theory. A more detailed study of the response of the (1,1) mode showed that the loss in amplitude at resonance decreased linearly with excitation angle (Rossby number) but that a significant 4% loss remained even for an extrapolation to zero Rossby number. Estimates of dissipation in the interior would account for most of this loss were they the only corrections to linear theory to be made.

The amplitude of resonance did not decrease to zero between spectral peaks. A general ~~use~~<sup>rise</sup> in response of the "valley" amplitudes was accounted for by a linear superposition of the total amplitudes of several of the more important modes. For the

purposes of the superposition it was assumed that the response amplitude of a particular mode varied with frequency in a manner given by a simple mechanical analogue. Several interesting effects were observed for the (1,1) mode with increasing oscillation angle,  $\epsilon$ .

A rectified current in the retrograde direction was found to have a square law dependent on  $\epsilon$ . Visual studies of the interior flow showed a vertical cylindrical boundary where there were sharp radial gradients in this zonal current.

A small but regular shift in the resonant frequency ratio,  $\Omega/\omega$ , for the (1,1) mode was observed with increasing  $\epsilon$ . This shift was about half of what one would expect due to the obvious error in rotation speed as measured from the container rotation speed.

A boundary layer instability which occupied the equatorial regions was found to extend to a certain latitude which depended on the oscillation angle,  $\epsilon$ . From this dependence a critical Reynolds number was estimated to be  $38 \pm 3$ .

Finally, at very large  $\epsilon$  amplitudes, it was found by means of a power spectral analysis of the rather complex fluid response that a mode which corresponded to the (5,1) mode was excited in addition to the (1,1) mode.

The measurement of precise decay rates for any particular mode was hindered by the interference of other modes during the free decay at resonance. Q's for several of the modes as

measured from half-power and  $45^\circ$  phase frequency locations were in fair agreement with linear theory. For the more complex modes, loss in amplitude at resonance was accompanied by a general lowering of measured Q values.

There is, at present, some theoretical interest in the modes of oscillation of a spherical shell of fluid. The introduction of an inner boundary presents difficulties in finding a solution which will satisfy both inner and outer surface boundary conditions. Several of these modes were excited experimentally for various ratios of inner to outer sphere diameters. The frequency locations of these modes were interpreted as follows: the equation for the stream function was shown to be the Euler equation of a proper variational problem. Eigenvalues were calculated by adjusting trial functions to satisfy the stationarity condition of this problem.

CHAPTER VI

Apparatus and Methods

<u>Section</u>		<u>Page</u>
6.1	Hardware	86
	6.1.1 Fluid container	
	6.1.2 Oscillation drive	
	6.1.3 Rotation drive	
	6.1.4 Electric slip rings	
6.2	Instruments	89
	6.2.1 Manometer tube	
	6.2.2 Pressure transducer	
	6.2.3 Transducer-converter	
	6.2.4 Tachometer generator	
	6.2.5 Recorder	
	6.2.6 Electric filters	
	6.2.7 Electronic stopwatch	
6.3	Calibrations	97
	6.3.1 Amplitude calibrations	
	6.3.2 Phase calibrations	
6.4	Probe effect	103
6.5	Angle measurement	103
6.6	Visual studies	104

6.1 Hardware

6.1.1 The fluid container

The spherical cavity was constructed as follows: a solid lucite cylinder was sliced into two right circular cylinders of unequal length so that the removal of a disc of material from the longer and a ring of material from the shorter permitted the two

halves to be fitted together again. (Figure 20.) With the equator as the plane of contact, a hemisphere was machined out of each of the two cylinders by rotating it in a lathe and restricting a tool bit to follow the arc of a circle. The assembled body of revolution was a cylindrical container with a centered spherical cavity of radius  $a = 10.00 \pm 0.01$  cm.

For subsequent work with a thick spherical shell of fluid an inner sphere was supported from below by an axial post which had been pressed into the container base.

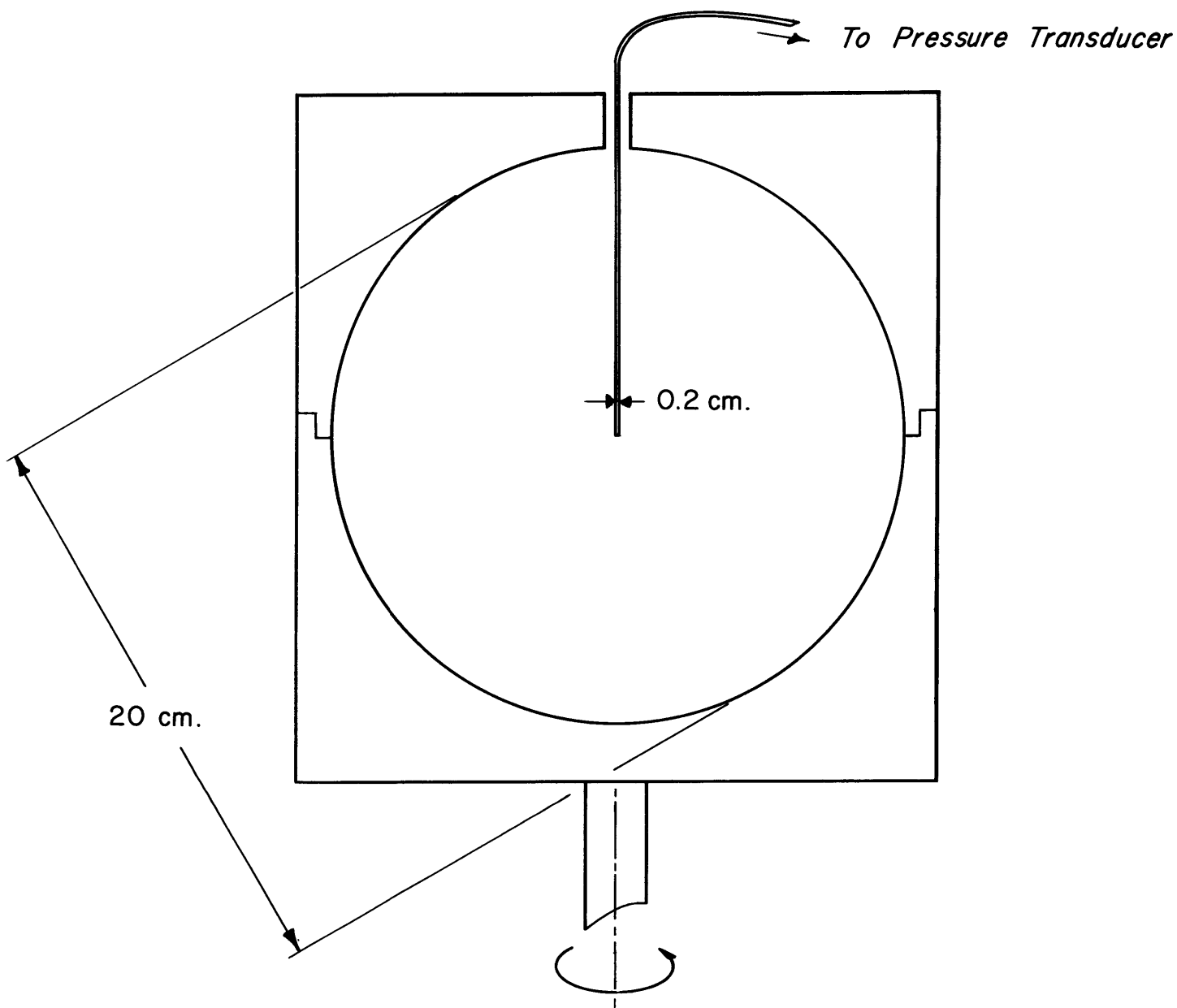
#### 6.1.2 Oscillator drive

One end of the cylindrical container was attached to a shaft which was free to rotate in bearings fixed coaxially in the main drive shaft. An axial torsion bar connected rigidly to both shafts was designed to oscillate the container relative to the main shaft at a natural frequency of 1.0 cps. (This choice of frequency made it possible to excite modes in the range  $1 > \frac{\omega}{2\pi} > 1/4$  for a practical rotation limit of  $\sqrt{2}/2\pi = 2$  cps.) By balancing the torque due to the angular acceleration of the container assembly,  $I\omega^2$ , with the restoring torque supplied by the torsion bar,  $\tau$ , it was found that a bar of steel with radius 0.17 cm and length 55 cm was convenient. The angular inertial reaction of the main shaft was minimized by adding a steel turntable of radius 75 cm and thickness 1.2 cm. To fix the amplitude of the oscillation,  $\epsilon$ , and restore bearing friction losses, a linkage (Figure 21) driven by a synchronous motor of the same output frequency as that given

Figure 20. Fluid container and pressure probe. The container is made of two lucite hemispheres fitted together at the equator. The probe, made of 15 gauge hypodermic tubing, is fixed in position. The perturbation of the rotation speed,  $\epsilon \omega \cos \omega t$ , is accomplished via an axial torsion bar and linkage shown in Figure 21.



OSCILLATING SPHERE



$$\Omega(t) = \Omega + \epsilon\omega \cos\omega t$$

above was added. The link,  $d$ , was adjusted so that the angle between  $d$  and  $b$  was, on the average over a cycle,  $90^\circ$ .

### 6.1.3 Rotation drive

The main shaft was driven by means of a pulley and gear-belt arrangement from a variable-speed transmission. The transmission functions as follows: a set of three conical planetary gears rotates about a common center axis at a fixed rate due to a synchronous drive input. A ring encircling the cones governs the rotation of the cones about their own axis because there is no slipping between the cones and the ring. The adjustable output is due to the adjustable radius of curvature of the cones in contact with the ring.

### 6.1.4 Electric slip rings

Electrical contact with the rotating system was maintained by a set of metal rings and spring loaded brushes. Power rings (brass) were used for current to the oscillator motor which was fixed to the rotating table; more highly conducting rings (silver) were used for the tachometer signal. Each ring had three brushes in contact with it to insure constant electrical connection.

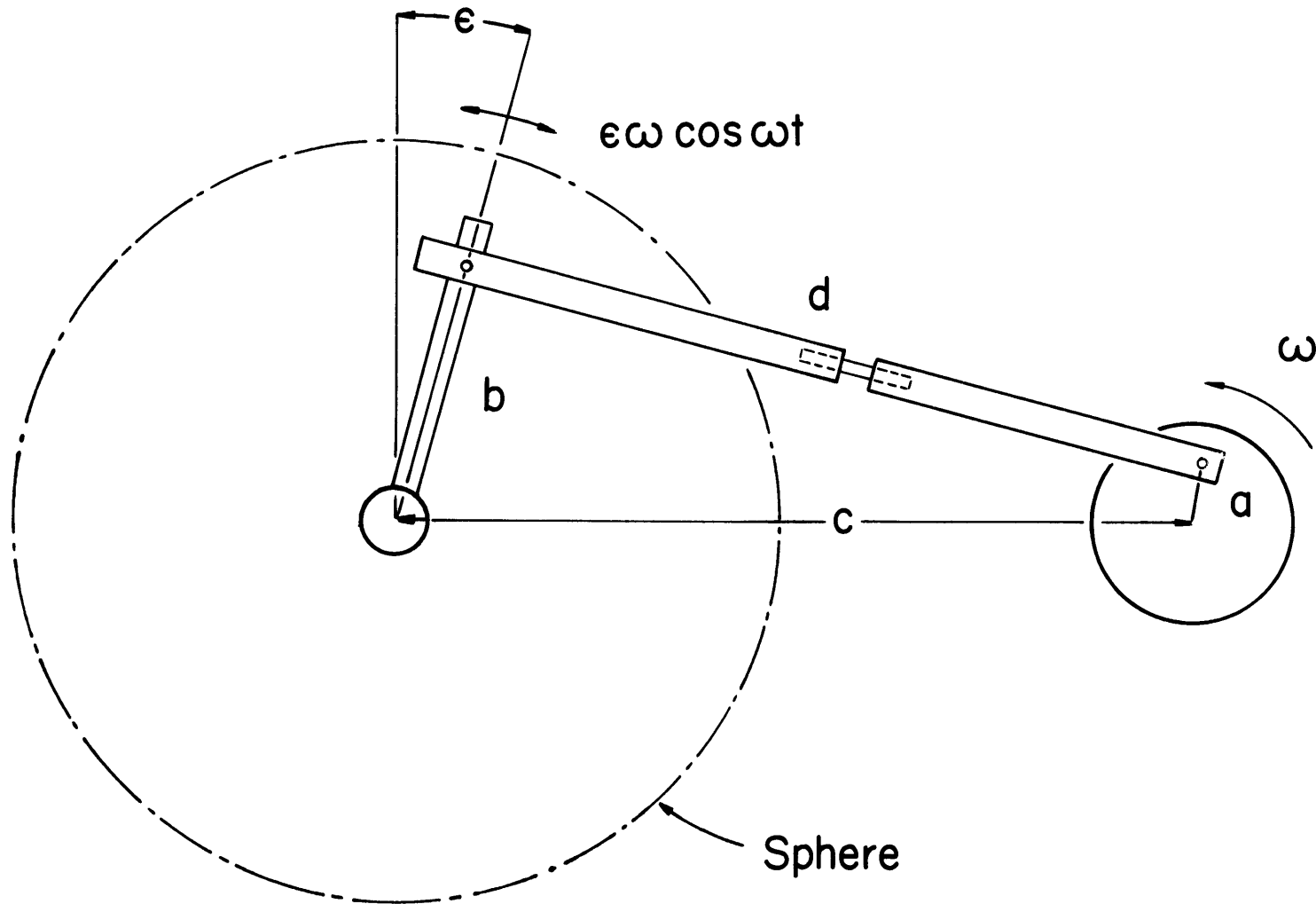
## 6.2 Instruments

### 6.2.1 Manometer tube

The axial symmetry of the flow was utilized by measuring the pressure response associated with axial fluid acceleration.

Figure 21. Top view of oscillator linkage and drive. A torsion bar located on the rotation axis helped supply the torque required to oscillate the sphere. The precise frequency of oscillation,  $\omega$ , and angle,  $\epsilon$ , were fixed by a synchronous motor and linkage a b c d. The adjustable link d allowed the mean angle between b and d to be set at  $90^\circ$  for various oscillation angles,  $\epsilon$ .

# OSCILLATOR LINKAGE



Initially, pressure was measured directly by observing the fluid level in an axial manometer tube. Precise ( $< 5\%$ ) measurements with this technique were hampered by free surface effects and a large dynamical correction ( $\sim 10\%$ ) due to the acceleration of the fluid in the manometer tube. The manometer tube technique was abandoned and replaced by a differential pressure transducer system. The low volume displacement ( $2.2 \times 10^{-4} \text{ mm}^3/\text{mm}$  water or  $1900 \text{ \AA}$  linear displacement in a  $1.2 \text{ mm}$  diameter probe) of the transducer rendered the inertial correction unnecessary.

#### 6.2.2 The pressure transducer

The pressure transducer and auxiliary electronics (Hewlett-Packard, Sanborn Division: transducer model No. 268B, transducer converter model S92-300) were used to convert an oscillatory fluid pressure to an oscillatory voltage of the same frequency. The transducer is differential in the sense that there are two chambers fitted with elastic membranes to respond to pressure changes supplied to each chamber. The chambers are not, however, independent, because both membranes are connected to a central shaft which drives a ferrite core. An applied fluid pressure to either chamber produces a deflection of the elastic membrane. The ferrite core, connected to the membrane, moves between primary and secondary coils of a transformer. The secondary coil is a composite of two reverse-wound coils so that a core displacement which increases the response of one coil decreases the response of the other. The difference in response of the two

secondary coils is converted to a DC voltage (see Transducer Converter, below) which is almost proportional to the applied pressure.

In this experiment one chamber was hydraulically connected with tubing (3/8" tygon) to a probe (O.D. 0.072", I.D. 0.048") the tip of which was located at the point at which pressure was to be measured. The other chamber was open to a column of fluid whose level could be adjusted to give a desired DC signal at the output. The null position for the ferrite core could thus be found by adjusting the bias head of fluid until there was no output voltage. All experiments conducted were for core movements about the same null position. This precaution was observed to avoid non-linear effects associated with mechanical deflections about a variable DC level.

### 6.2.3 Transducer converter

The transducer converter produces the excitation voltage (40 volts, 0 to peak, at 5000 cps) for the transducer primary coils and detects the induced signals in the secondary coils. The excitation voltage is produced as follows. A 60 cps 115 volt RMS line signal is supplied to a step-down power transformer; the secondary coil voltage is rectified (full wave) to give 40 volts DC level. One stage of regulation follows the rectification. This essentially DC signal is the source for an oscillator whose output is a signal of 40 volts zero to peak at 5000 cps. This is the transducer primary coil excitation voltage. The

5000 cps carrier from each side of the transducer secondary coil relative to the common center tap is rectified separately.

Non-linearity in the rectified signal is summarized as follows: Because both rectifier diodes operate near peak voltages for small core displacements about the null position, there is little non-linear contribution to the response from these elements. In addition, for small deflections of the elastic membrane, response for this element is almost proportional to pressure. Similarly, for small core deflections voltage induced in the secondary coils will be almost linear with core deflection. Calibration experiments show that the total of all non-linear effects leads to a quadratic response of voltage for applied pressure which is only 3% of the linear response.

#### 6.2.4 Tachometer generator

The armature of a tachometer generator was fitted with a grooved pulley and O-ring assembly. The generator was fixed in position so that the O-ring was in contact with the surface of the container. Thus, an oscillation of the container,  $Ew \cos \omega t$  produced an A.C. voltage proportional to  $Ew \cos \omega t$ . The phase of the forcing relative to the fluid response was then measured as a time base comparison of this signal against the transducer signal.

#### 6.2.5 Recorder

An analog recorder (Beckman, Type S-II Dynograph) was used to display both the pressure transducer and tachometer signals.

The properties of the recorder are summarized as follows:

1. Input: Differential input effectively isolates both sides of the signal input from "ground". This input was compatible with the differential output of the transducer converter. Range of input signals is  $10\ \mu\text{v/cm}$  to  $50\ \text{v/cm}$  (each of four channels has writing width of 4 cm). Pressure signals were in the ranges  $100\text{-}500\ \mu\text{v/cm}$ ; tachometer signals,  $50\text{-}100\ \text{mV/cm}$ .
2. Speed selections: Chart speeds in the range (.1-25) cm/sec. were available. Slow speed (0.1 cm/sec) was used for runs where many readings of amplitude were desired for averaging; faster speeds were used to spread out waveforms for phase reduction.
3. Band width: Response as a function of frequency was essentially constant in the range 0 to 150 cps.
4. Signal source resistance: Peak-to-peak recorder noise was approximately  $5\ \mu\text{v}$ , input being shorted,  $10\ \mu\text{v}$ , at  $100,000\ \Omega$  input resistance and  $800\ \mu\text{v}$  at 1 megohm input resistance.

#### 6.2.6 Electric filters

With an essentially flat recorder frequency response, there was very little loss of signal at 1 cps, but also there was little attenuation of 60 cps "pick up". Although both tachometer and pressure transducer signals contained this 60-cycle "noise", the signal-to-noise ratio for the transducer signal was significantly



smaller than that of the tachometer. Noise at frequencies other than 60 cps was negligible by comparison.

Transducer Filter. Precautions were taken to shield all lines from the transducer converter to the recorder input. Significant reduction in 60-cycle noise was found by connecting the center tap of the differential output of the transducer converter to cable shield which was finally connected to ground at the recorder input. There still remained significant 60-cycle noise ( $150\mu v$  compared to signals of  $\sim 500\mu v$ ) which was apparently due to 60-cycle ripple in the converter itself.

A resistor-capacitor electric filter in which components carry the voltage in proportion to their impedance to the various frequencies in the input wave was designed to "attenuate" (in this fashion) the 60-cycle wave. Two constraints were considered. First, the resistance of the filter as viewed from the recorder was to be kept below  $100,000\Omega$  to limit recorder noise to  $10\mu v$ ; second, the impedance of the filter as viewed from the signal source was to be significantly greater than the source impedance of  $15,000\Omega$  in order that most of the signal voltage would be realized across the filter. A three-stage R-C filter was designed with each stage having its critical frequency  $1/RC = (\omega_s * \omega_N)^{1/2}$ , with stages 1 and 2 effectively independent and stage 3 a repetition of stage 2. Some sacrifice in efficiency in signal-to-noise ratio increase was traded, with the addition of stage 3, for not significantly increasing the filter output resistance.

Tachometer Filter. There remained, after shielding of cables, a significant 60-cycle pickup voltage in the tachometer generator signal. Because the signal levels in this case were much greater (50mv range), input resistance to the recorder was no longer a severe constraint in the design of a filter.

### 6.2.7 Electronic stopwatch

The rotation rate  $\Omega(t)$  was measured with an electronic stopwatch and trigger circuit. The stopwatch (Beckman, Model 5230, Eput and Timer) begins counting with the arrival of an external pulse. Counts are generated by an internal oscillator and displayed with neon tubes on the counterface. Counting ceases with the arrival of a second pulse identical to the first.

External pulses which begin and stop the internal oscillator of the stopwatch are delivered by a "trigger" circuit of two resistors  $R_C$ ,  $R_B$  and a battery of voltage  $E$ , all in series. The resistor  $R_C$  is a cadmium sulfide element; its resistance decreases from  $R_2=5000\Omega$ , dark resistance, to  $R_1=200\Omega$ , light resistance for a 75-watt bulb at 5-cm distance from the element. The resistor  $R_B$  across the stopwatch input was chosen to maximize the voltage pulse delivered to the stopwatch (for a fixed  $E$ ) with a change in  $R_C$ . The voltage pulse is given by

$$\Delta V_{R_B} = \left( \frac{R_B}{R_1 + R_B} - \frac{R_B}{R_2 + R_B} \right) E.$$

For  $\frac{d(\Delta V_{R_B})}{d R_B} = 0$ ,  $R_B = \sqrt{R_1 R_2} = 1000 \Omega.$

A mirror in the steady part of the rotating system (rotating table) reflects the light from a fixed source (75-watt bulb) to the fixed Cds resistor. For the interval in which  $R_C$  is decreased, there is an increase in voltage across  $R_B$  sufficient to activate the internal clock of the stopwatch.

### 6.3 Calibrations

#### 6.3.1 Amplitude calibration

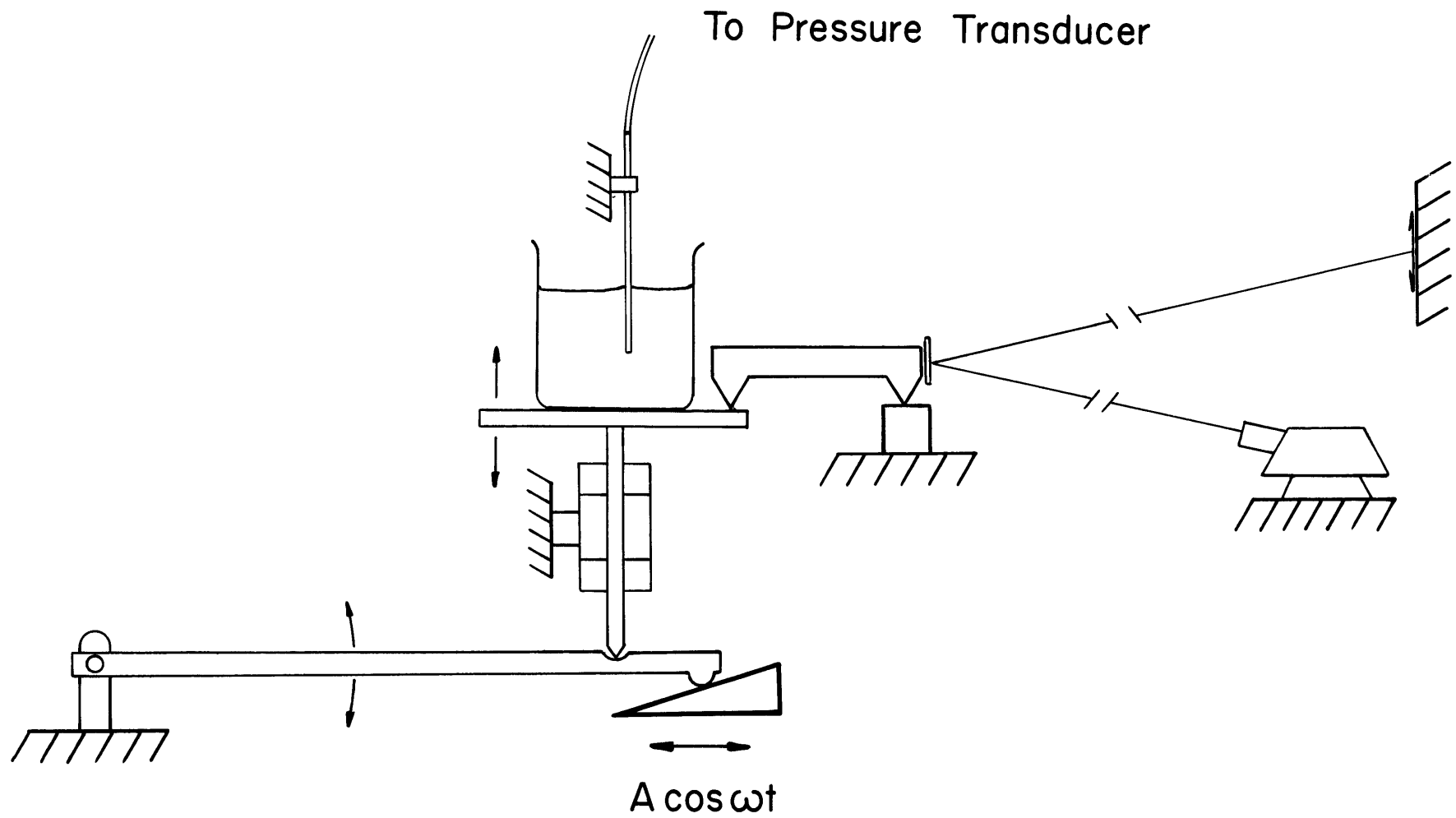
A known pressure difference was supplied to the transducer to permit subsequent measurements of absolute pressure. Because of significant frequency-dependent electrical (filter) and mechanical (viscous fluid lag) losses, the calibration pressure was supplied at the working oscillation frequency ( $\omega = 6.2$  rad/sec). Specifically, a beaker of fluid was raised and lowered harmonically while the pressure probe remained fixed under this "oscillating" free surface (Figure 22).

The time-dependent part of the pressure at mean depth  $H$  below the surface is given by

$$\rho g \Delta \left\{ \left[ 1 - \frac{H\omega^2}{g} \right] \sin \omega t + \frac{\omega^2}{2g} \cos 2\omega t \right\}$$

Where  $\Delta$  = amplitude of free surface displacement (cm),  $g$  = acceleration due to gravity ( $\text{cm}/\text{sec}^2$ ) and  $\rho$  = fluid density ( $\text{g}/\text{cm}^3$ ).

Figure 22. Amplitude and phase calibration. The triangular device in the centre of the figure is connected to the base of the oscillating sphere. The small fluid level displacements are magnified by the optical lever and projection system. Phase calibrations were made by a time base comparison of the pressure signal with the signal from a tachometer generator in contact with the sphere.



CALIBRATION SCHEMATIC

The optical leve, shown in Figure 22, was used to magnify the free surface displacement. A typical magnification factor was 200.

A calibration constant  $c_\mu$ , for each gain selection  $\mu$  of the chart recorder, was constructed as follows:

$$c_\mu = A_\mu / \Delta^*$$

where  $A_\mu$  = peak-to-peak response to applied pressure head at gain setting  $\mu$  on chart recorder, and  $\Delta^* = \Delta(1 - \frac{H\omega^2}{g})$  i.e., effective applied pressure head in centimeters of fluid.  $c_\mu$  is measured in centimeters of response per centimeter of applied fluid head.

A typical pair of calibration lines for water and silicone oil are shown in Figure 23. The fluid displacement,  $\Delta$ , is shown in millimeters in the figure; the maximum pressure observed for the (1,1) mode with  $\zeta = 8^\circ$  corresponds to approximately 1mm of fluid displacement.

Pressure measurements of the sphere in terms of centimeters of recorder response,  $E_\mu$ , were converted to pressure units,

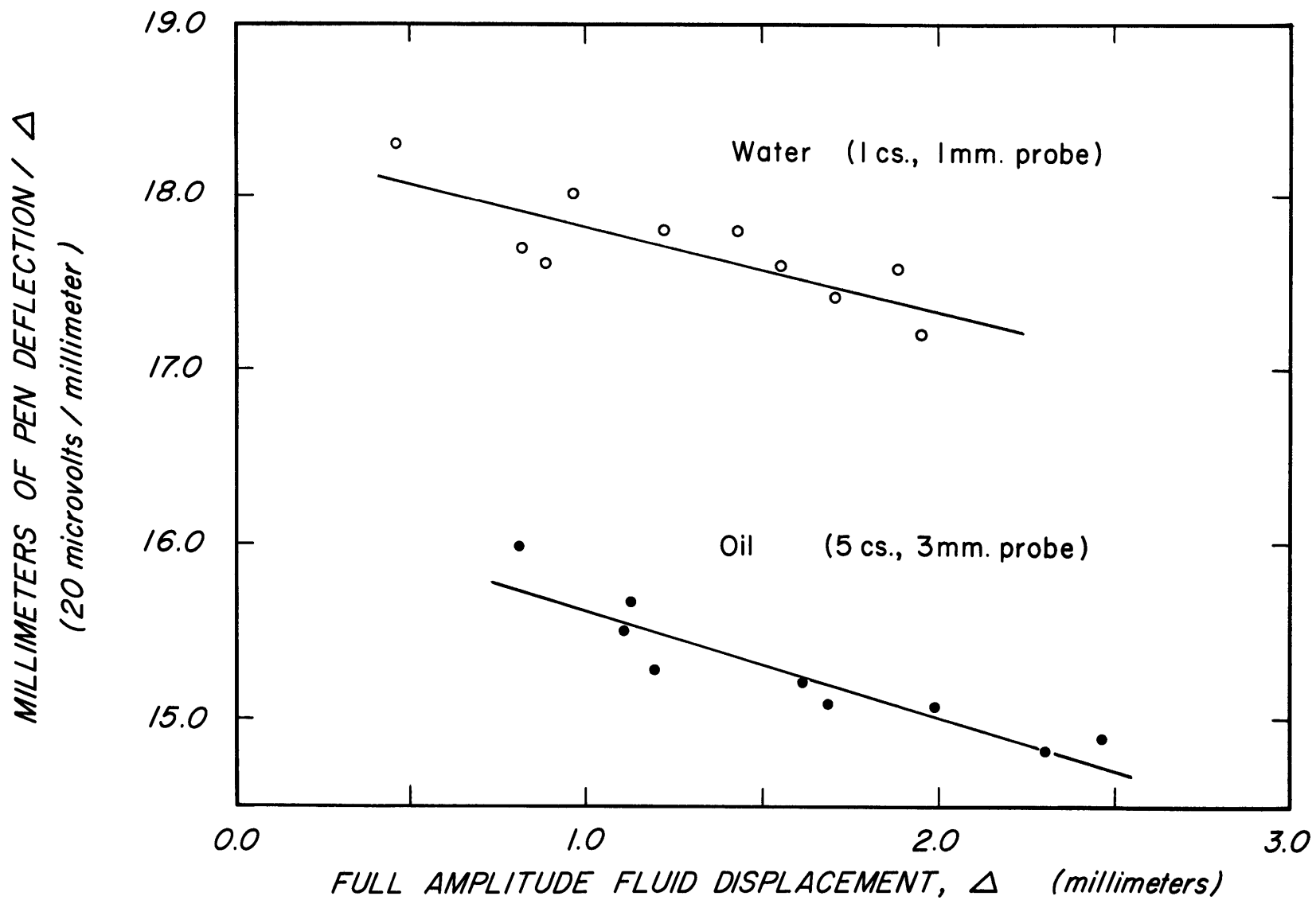
$$\Delta P = \rho g E_\mu / c_\mu \text{ dynes/cm}^2$$

where  $\rho$  is the density ( $\text{gm/cm}^3$ ) of the fluid in the beaker.

Scaling of the equations of motion shows that the pressure scale is

Figure 23. Response calibrations for the pressure transducer system. Abscissa is the peak to peak amplitude,  $\Delta$ , of the fluid displacement; ordinate is the peak to peak response,  $C_{\mu}$  on the chart recorder (20 micro volts/millimeter scale) per unit fluid displacement,  $\Delta$ .  
○, water, probe *i.d.* = 1 mm, *o.d.* = 2 mm ; ●, oil (5 cs), probe *i.d.* = 3 mm; *o.d.* = 5 mm. Lines shown minimize the sum of squares of the deviations of experimental points above and below the line.

# AMPLITUDE CALIBRATIONS





$$P_0 = \rho \epsilon \omega^2 a^2$$

where  $\rho$  = density of the fluid sphere ( $\text{g/cm}^3$ ),  $\epsilon$  = half-amplitude of oscillation (radians),  $a$  = sphere radius (cm) and  $\omega$  = oscillation frequency (rad/sec). A convenient pressure coefficient based on the above scaling was constructed as

$$C_p = \frac{\Delta P}{\rho \epsilon \omega^2 a^2} = \frac{g}{\omega^2 a^2} \left( \frac{1}{C_m} \right) \left( \frac{\epsilon_m}{\epsilon} \right)$$

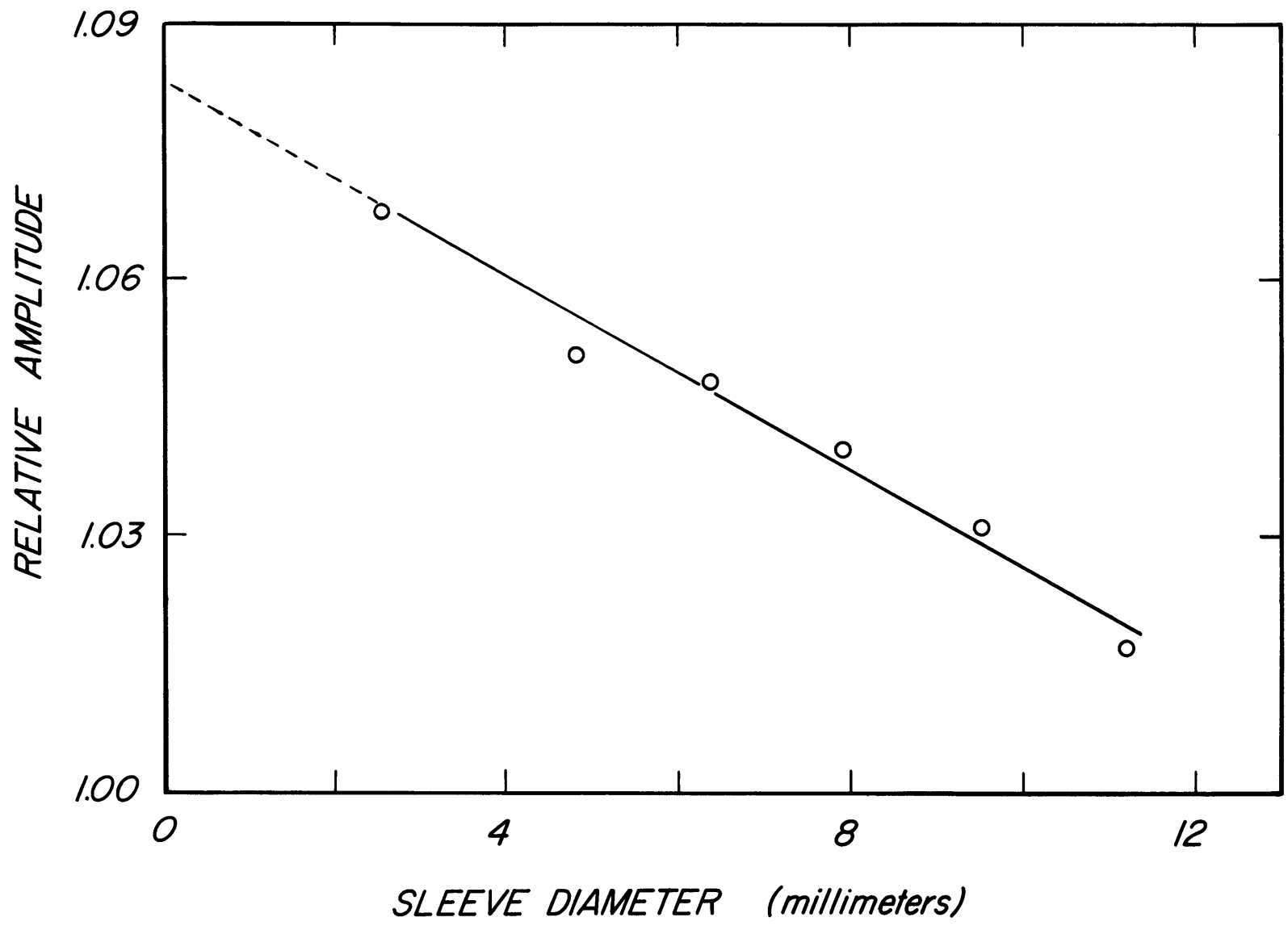
The density,  $\rho$ , does not appear because the calibration fluid was the same as the working fluid.

### 6.3.2 Phase calibration

Reference to Figure 22 shows that during calibrations, the maximum angular displacement of the sphere corresponds to the maximum change in head of the calibration fluid surface. Thus, if there were no phase lags in the system the maximum response of the pressure transducer would lag by  $90^\circ$  the maximum response from the tachometer generator. Direct measurement of the total phase lag of the system under these conditions yields the net phase difference due to lags in both the pressure signal (viscous fluid lag, filter) and the tachometer signal (filter), after the known  $90^\circ$  lag has been removed. The direct measurement of phase, was observed as the distance between a simultaneous event (a pulse) on each of the pressure and tachometer signal traces.

Figure 24. Response of the (1,1) mode. Probe at  $z = -0.3a$ ;  $\epsilon = 7.9^\circ$ ; water. Cylindrical sleeves extending from  $z = 0$  to  $z = a$  were fitted to the probe. Straight line is best fit loss curve for sleeve diameter; loss is 0.5% per millimeter sleeve diameter.

PROBE EFFECT  $\Rightarrow$  (1,1) MODE,  $Z = -0.3a$ ,  $\epsilon = 7.9^\circ$



The two traces were compared by the superposition of one over the other on a glass table illuminated from below.

#### 6.4 Probe effect

Some loss in response arose from the rubbing of the fluid against the pressure probe. The rate of this loss as a function of probe diameter was measured in the following manner. The probe was lowered so that the tip was below the equatorial plane of the sphere ( $z/a = -0.3$ ). For  $\Omega/\omega$  adjusted to be near the (1,1) resonance, the response was measured with sleeves of various diameters surrounding the probe and extending from the equatorial plane to the pole. The amplitude response for water as a function of sleeve diameter is shown in Figure 24. The least squares straight line shown in the figure corresponds to a loss of 0.5% per millimeter of probe diameter. This corresponds to a loss for the experiments with water of 0.9%. Similar probe effect experiments give a loss at resonance of 3.1% for oil results.

#### 6.5 Angle measurement

The moment of inertia of the sphere was not so small compared to the turntable moment of inertia that inertial reaction of the turntable with the oscillation of the sphere was negligible. This reaction would have the effect of decreasing the free angle of oscillation,  $\epsilon$ , compared to a value measured for the table rigidly fixed. The angle was therefore measured while

the turntable was rotating by observing the inter-arrival times for a fixed point in the rotating and oscillating system. Physically, this was done by fixing the reflecting mirror, for the electronic stopwatch circuit, on the sphere.

If  $T_{\max}$  = maximum inter-arrival time (seconds),  
 $T_{\min}$  = minimum inter-arrival time (seconds),  
and  $\omega$  = oscillation frequency (radians/sec),

it can be shown that the dynamic half-amplitude of oscillation is

$$\epsilon_d = \frac{\pi [T_{\max} - T_{\min}]}{\left| T_{\max} \sin\left(\frac{\omega T_{\min}}{2}\right) + T_{\min} \sin\left(\frac{\omega T_{\max}}{2}\right) \right|} \text{ radians.}$$

This result is due to Toomre.

## 6.6 Visual studies

Because the flow was axisymmetric it was possible to illuminate the fluid in meridional planes with a fixed plane of light passing through the rotation axis. Fluid particles are "tagged" both with dye and aluminum particles. Primary radial oscillatory motions were made visible, with the aluminum particle suspension, by the flexing of an axisymmetric vertical shear zone associated with a steady secondary zonal current. Vertical oscillations of

the fluid were observed on the rotation axis by following aluminum particles directly.

The steady zonal current was observed by injecting small quantities of an almost neutrally bouyant basic solution into the sphere of water and phenolphthalein solution. The injected fluid immediately colours (red) and can be followed for a considerable time.

The boundary layers were observed by creating a very dense aluminum particle suspension in the interior region so that light from a fixed source would only penetrate the boundary layer regions. To prevent aluminum particles from sticking to the surface of the sphere, the interior surface was rubbed with glycerine before filling the container with water. Aluminum particle suspensions were made as follows: to a small amount of detergent a pinch of extra fine aluminum flakes was added. When wetting was complete, a little methanol and water were added to increase the solution volume. In most cases it was convenient to inject the suspension into the sphere of fluid with a hypodermic syringe.

REFERENCES

- Aldridge, K. D. and Toomre, A., 1967: Axisymmetric inertial oscillations of a rotating sphere of fluid. To be submitted to J. F. M.
- Arons, A. B. and Stommel, H., 1956: A  $\beta$  plane analysis of free periods of the second class in meridional and zonal oceans. Deep-Sea Res., 4, 23-31.
- Basset, A. B., 1888: A treatise on Hydrodynamics. Vol. II. Dover Books.
- Bjerknes, V. J. Bjerknes, H. Solberg and T. Bergeron, 1933: Physikalische Hydrodynamik. Berlin, J. Springer.
- Bullard, E. C. and Gellman, H., 1954: Phil. Trans. A, 247, 213-278.
- Cartan, M. E., 1922: Bull. Sci. Math., 46, 317.
- Chandrasekhar, S., 1961: Hydrodynamic and Hydromagnetic Stability, Oxford: Clarendon Press. Chapter 7.
- Eckart, C., 1960: Hydrodynamics of oceans and atmospheres. London: Pergamon Press.
- Fraser, D. A. S., 1958: Statistics, an Introduction, New York: John Wiley and Sons.
- Fultz, D., 1959: A note on overstability and the elastoid-inertia oscillations of Kelvin, Solberg, and Bjerknes. J. of Met. 16, 199-208.
- Greenspan, H. P., 1964: On the transient motion of a contained rotating fluid, J. F. M. 20, part 4, 673-696.
- Hildebrand, F. B., 1961: Methods of Applied Mathematics. Prentice Hall Inc.
- Hough, S. S., 1898: On the application of Harmonic analysis to the dynamical theory of the tides, Phil. Trans., 191, 139-185.
- Hide, R., 1958: An experimental study of thermal convection in a rotating liquid. Phil. Trans. A., 250, 451.

- Hide, R., 1966: Free hydromagnetic oscillations of the earth's core and the theory of the geomagnetic secular variation. Phil. Trans. A, 259, 615-650.
- Kelvin, 1880: On the vibrations of a columnar vortex. Collected papers, Vol. 4, p. 152-165.
- Kudlick, M. D., 1966: On transient motions in a contained, rotating fluid. Ph.D. Thesis, M.I.T.
- Lee, Y. W., 1960: Statistical Theory of communication. John Wiley and Sons.
- Longuet-Higgins, M. S., 1966: Personal Communications.
- Longuet-Higgins, M. S., 1966: Planetary waves on a hemisphere bounded by meridians of longitude. Phil. Trans. A, 260, 317-350.
- Long, R. R., 1952: The flow of liquid past a barrier in a rotating spherical shell. J. of Met., 9, 187-199.
- Phillips, O. M., 1960: Centrifugal waves. J. F. M., 7, 340.
- Prandtl, L., 1952: Essentials of Fluid Dynamics. New York: Hafner.
- Rossby, C. G., 1939: Relation between variations in the intensity of the zonal circulation of the atmosphere and the displacement of semi-permanent centers of action. J. of Mar. Res. 2, No. 1, p. 38.
- Rossby, H. T., 1966: An experimental study of Benard convection with and without rotation. Ph.D. Thesis, M.I.T.
- Stern, M., 1963: Trapped oscillations in the equatorial boundary layer. Tellus, Vol. 15, No. 3.



APPENDIX I. Polynomial Representation of the Stream Function,  $\psi_{nm}$ .

We had from Chapter II, 2.10a,

$$\psi_{nm}(\eta, \mu) = \left(\frac{1}{1-x_m^2} - \eta^2\right)^{\frac{1}{2}} (1-\mu^2)^{\frac{1}{2}} P_{2n+2}^{(1)}\left[(1-x_m^2)^{\frac{1}{2}}\eta\right] P_{2n+2}^{(1)}(\mu) \quad \dots \text{Al.1}$$

We wish to show that by the transformation of variables to  $(R, z)$  coordinates,

$$R = \left(\frac{1}{1-x_m^2} - \eta^2\right)^{\frac{1}{2}} (1-\mu^2)^{\frac{1}{2}} \quad \text{Al.2}$$

$$z = \left(\frac{1}{x_m^2} - 1\right)^{\frac{1}{2}} \eta \mu$$

the stream function can be written

$$\psi_{nm}(R, z) = R^2 z \prod_{k=1}^n \left(1 - \frac{x_m^2}{x_k^2} z^2 - \frac{1-x_m^2}{1-x_k^2} R^2\right)$$

By definition,

$$P_{2n+2}^{(1)}(x) = C x (1-x^2)^{\frac{1}{2}} \prod_{k=1}^n (x^2 - x_k^2) \quad \text{Al.3}$$

where C is some constant. Then from Al.1, Al.3

$$\psi_{nm}(\eta, \mu) = \psi_0 \prod_{k=1}^n \left[(1-x_m^2)\eta^2 - x_k^2\right] \left[\mu^2 - x_k^2\right]$$

where

$$\psi_0 = C R (1 - X_m^2)^{1/2} \eta \mu \left[ 1 - (1 - X_m^2) \eta^2 \right]^{1/2} [1 - \mu^2]^{1/2}$$

or

$$\psi_0 = C' R^2 Z \quad \text{from A2.2}$$

$$\psi_{nm} = C' R^2 Z \prod_{k=1}^n \left[ \frac{(1 - X_m^2) \eta^2 \mu^2 - X_k^2 (\mu^2 + (1 - X_m^2) \eta^2) + X_k^4}{X_k^2} \right]$$

The underlined quantities may be converted to terms in  $(R, Z)$  from the transformations A1.2.

From the transformation of  $Z$ ,

$$(1 - X_m^2) \eta^2 \mu^2 = X_m^2 Z^2$$

From the transformation of  $R$ ,

$$1 - [\mu^2 + \eta^2 (1 - X_m^2)] + (1 - X_m^2) \eta^2 \mu^2 = (1 - X_m^2) R^2$$

From the previous line,

$$\mu^2 + \eta^2 (1 - X_m^2) = 1 - (1 - X_m^2) R^2 + X_m^2 Z^2 \quad \text{and}$$

therefore,

$$\psi_{nm} = C' R^2 Z \prod_{k=1}^n \left[ X_m^2 Z^2 - X_k^2 (1 - (1 - X_m^2) R^2 + X_m^2 Z^2) + X_k^4 \right]$$

or

$$\psi_{nm}(z) = C'' R^2 z \prod_{k=1}^n \left[ 1 - \frac{x_m^2 z^2}{x_k^2} - \frac{1 - x_m^2 R^2}{1 - x_k^2} \right].$$

APPENDIX II. Response at Resonance for the Sphere.

Let  $(x, y, z)$  be a cartesian coordinate frame fixed in the rotating system,  $\Omega$ . The  $x$  axis is parallel to lines of constant latitude and its sense is eastward; the  $z$  axis is normal to the surface of the sphere and its sense is into the fluid; the  $y$  axis, (directed southward), completes the right handed system.

The momentum equations for velocity components  $(v_x, v_y)$  are, to a boundary layer approximation:

$$\frac{\partial v_x}{\partial t} + 2\Omega \cos \theta v_y = \nu \frac{\partial^2 v_x}{\partial z^2} \quad \text{A2.1}$$

$$\frac{\partial v_y}{\partial t} - 2\Omega \cos \theta v_x = -\frac{1}{\rho} \frac{\partial p}{\partial y} + \nu \frac{\partial^2 v_y}{\partial z^2}$$

where  $\theta$  is the co-latitude. The azimuthal pressure gradient,  $\frac{\partial p}{\partial x}$ , vanishes because there is axial symmetry.

Boundary conditions on  $(v_x, v_y)$  are, from (§ 2.1, equation 2.5) at  $z = \infty$ ,

$$v_x = \epsilon \omega a \frac{U(\theta)}{X_{nm}} \left[ -M \cos \omega t + N \sin \omega t \right] \quad \text{A2.2}$$

$$v_y = \epsilon \omega a \frac{U(\theta)}{\cos \theta} \left[ -M \sin \omega t - N \cos \omega t \right]$$

and at  $z = 0$

$$\begin{aligned} v_x &= K E \omega a \sin \theta \cos \omega t \\ v_y &= 0 \end{aligned} \tag{A2.3}$$

where  $K=1$  when container oscillation is "turned on" and  $K=0$  when it is "turned off".

We separate the velocity components  $(v_x, v_y)$  into  $z$  independent (interior) and  $z$  dependent (boundary layer) parts as follows:

$$\begin{aligned} v_x(z, t) &= v_{x\infty}(t) + v_x'(z, t) \\ v_y(z, t) &= v_{y\infty}(t) + v_y'(z, t) \end{aligned} \tag{A2.4}$$

With this separation the momentum equations become, with  $2\Omega \cos \theta = f$ :

$$\begin{aligned} \left( \frac{dv_{x\infty}}{dt} + f v_{y\infty} \right) + \frac{dv_x'}{dt} + f v_y' &= \nu \frac{d^2 v_x'}{dz^2} \\ \frac{dv_{y\infty}}{dt} - f v_{x\infty} + \frac{1}{\rho} \frac{dP}{dy} + \frac{dv_y'}{dt} - f v_x' &= \nu \frac{d^2 v_y'}{dz^2} \end{aligned} \tag{A2.5}$$

The bracketed terms are both zero for  $z \rightarrow \infty$  because we want  $v_x', v_y' \rightarrow 0$  as  $z \rightarrow \infty$ . Since those terms are independent of  $z$ , we have for all  $z$ ,

$$\begin{aligned} \frac{dv_x'}{dt} + f v_y' &= \nu \frac{d^2 v_x'}{dz^2} \\ \frac{dv_y'}{dt} - f v_x' &= \nu \frac{d^2 v_y'}{dz^2} \end{aligned} \tag{A2.6}$$

subject to the boundary conditions

at  $z = \infty$

$$\begin{aligned} v_x' &= 0, \\ v_y' &= 0, \end{aligned} \tag{A2.7}$$

and at  $z=0$

$$\begin{aligned} v_x' &= \epsilon \omega a \left\{ \left[ K \sin \theta + \frac{M U(\theta)}{X_{hm}} \right] \cos \omega t - \frac{N U(\theta)}{X_{hm}} \sin \omega t \right\} \\ v_y' &= \epsilon \omega a \left\{ \left[ \frac{M U(\theta)}{\omega \sin \theta} \right] \cos \omega t + \frac{N U(\theta)}{\omega \sin \theta} \sin \omega t \right\} \end{aligned} \tag{A2.8}$$

Elimination of either  $v_x'$  or  $v_y'$  in equations A2.6 leads to an equation for the other variable of the form

$$\left( \frac{\partial}{\partial t} - \nu \frac{\partial^2}{\partial z^2} \right)^2 V + f^2 V = 0 \tag{A2.9}$$

Its elementary solutions are

$$V(z, t) = \text{Re} \left\{ V_0 e^{i\omega t} e^{\alpha z} \right\}$$

where

$$(\nu \alpha^2 - i\omega)^2 + f^2 = 0.$$

The latter equation has four roots

$$\alpha = \pm (1+i) \left[ \frac{\omega \pm f}{2\nu} \right]^{1/2}$$

two of which do not correspond to boundary layer solutions because  $\text{Re } \alpha > 0$ .

The two physically admissible wave numbers are abbreviated

as

$$\alpha_+ = \left| \frac{\omega + f}{2\nu} \right|^{1/2} ; \quad \alpha_- = \left| \frac{\omega - f}{2\nu} \right|^{1/2} \quad (0 \leq \theta \leq \pi/2)$$

This representation implies that the boundary layer has a double structure in  $z$ . The  $\alpha_+$  layer is well behaved at all latitudes; the  $\alpha_-$  layer becomes very thick at  $f = \omega$ . Since, the boundary layer length scale is proportional to the ratio of viscous forces to inertial forces, this thickening of the  $\alpha_-$  layer corresponds to the latitude where the coriolis force on a fluid particle is equal and opposite to the centrifugal force. The particle orbit for the  $\alpha_+$  mode is in the opposite sense to the orbit of the  $\alpha_-$  mode so that the  $\alpha_+$  layer remains well behaved.

We choose solutions to A2.6

$$\begin{aligned} v_x' &= e^{-\alpha_+ z} \operatorname{Re} \left\{ A e^{i(\alpha_+ z - \omega t)} \right\} + e^{-\alpha_- z} \operatorname{Re} \left\{ C e^{i(\alpha_- z \pm \omega t)} \right\} \\ v_y' &= e^{-\alpha_+ z} \operatorname{Re} \left\{ -i A e^{i(\alpha_+ z - \omega t)} \right\} \pm e^{-\alpha_- z} \operatorname{Re} \left\{ -i C e^{i(\alpha_- z \pm \omega t)} \right\} \end{aligned} \quad \dots \text{A2.10}$$

where + corresponds to  $\theta < \theta_c$

- corresponds to  $\theta > \theta_c$

and  $\theta_c = \cos^{-1}(\omega / 2\Omega)$

The application of the boundary conditions A2.8 give

$$A_r = \epsilon \omega a \left[ K - \frac{M U(\theta)}{\cos \theta} \left( 1 - \frac{\cos \theta}{x} \right) \right] ; \quad A_i = \epsilon \omega a \frac{N U(\theta)}{\cos \theta} \left( 1 - \frac{\cos \theta}{x} \right)$$

$$C_r = \epsilon \omega a \left[ K + \frac{M U(\theta)}{\cos \theta} \left( 1 + \frac{\cos \theta}{x} \right) \right] ; \quad C_i = \epsilon \omega a \frac{N U(\theta)}{\cos \theta} \left( 1 + \frac{\cos \theta}{x} \right)$$

where  $A = A_r + i A_i$  ;  $C = C_r + i C_i$  .

We now calculate possible steady response amplitudes based on the balance between the rate at which energy is being dissipated in the fluid and the rate at which work is being done on the fluid by the container.

The rate of dissipation per unit area is

$$D = \mu \int_{z=0}^{\infty} \left[ \left( \frac{\partial v_x}{\partial z} \right)^2 + \left( \frac{\partial v_y}{\partial z} \right)^2 \right] dz.$$

Since

$$\left( \frac{\partial v_{x,y}}{\partial z} \right)^2 = \left( \frac{\partial v_{x,y}'}{\partial z} \right)^2 \equiv \frac{d}{dz} \left( v_{x,y}' \frac{\partial v_{x,y}'}{\partial z} \right) - v_{x,y}' \frac{d^2 v_{x,y}'}{dz^2},$$

integration by parts and the application of A2.6 gives,

$$D = \mu \left[ v_x' \frac{\partial v_x'}{\partial z} + v_y' \frac{\partial v_y'}{\partial z} \right]_{z=0}^{z=\infty} - \rho \int_0^{\infty} \left[ v_x' \left( \frac{\partial v_x'}{\partial t} + f v_y' \right) + v_y' \left( \frac{\partial v_y'}{\partial t} - f v_x' \right) \right] dz.$$

Since  $v_x', v_y' \rightarrow 0$  as  $z \rightarrow \infty$  the upper limit of the first square bracket is zero. The integrands vanish if we take the time average ( $\langle \rangle$ ) over one oscillation cycle and

$$\langle D \rangle = \mu \left[ \left\langle v_x' \frac{\partial v_x'}{\partial z} \right\rangle + \left\langle v_y' \frac{\partial v_y'}{\partial z} \right\rangle \right]_{z=0}.$$



The time average of the rate at which the container does work on a unit area of the fluid is

$$\langle W \rangle = \mu \left. \left\langle v_x \frac{\partial v_x'}{\partial z} \right\rangle \right|_{z=0} \quad \text{A2.11}$$

The balance condition that

$$\iint_S \langle D \rangle d\tau = \iint_S \langle W \rangle d\tau$$

becomes

$$\iint_S \left[ \left\langle v_x' \frac{\partial v_x'}{\partial z} \right\rangle + \left\langle v_y' \frac{\partial v_y'}{\partial z} \right\rangle \right]_{z=0} d\tau = \iint_S \left. \left\langle v_x \frac{\partial v_x'}{\partial z} \right\rangle \right|_{z=0} d\tau \quad \text{A2.12}$$

In terms of the solution A2.10 the dissipation is

$$\frac{\mu}{4} \left( \frac{\omega}{2\nu} \right)^{1/2} (\epsilon \omega a)^2 \left[ K^2 I_0 + 2KM I_1 + (M^2 + N^2) I_2 \right]$$

where

$$\frac{1}{2} I_\rho = 2\pi a^2 \int_0^{\pi/2} \left\{ \sin^3 \theta \left\{ \frac{U(\theta)}{\sin \theta \cos \theta} \right\}^\rho \right.$$

$$\left. \cdot \left\{ \left( \frac{\cos \theta}{x} + 1 \right)^{1/2} \left( \frac{\cos \theta}{x} - 1 \right)^\rho + \left| \frac{\cos \theta}{x} - 1 \right|^{1/2} \left( \frac{\cos \theta}{x} + 1 \right)^\rho \right\} d\theta \right.$$

From A2.11 and the solution A2.10 the time averaged work done over the sphere is

$$\frac{\mu}{4} \left( \frac{\omega}{2\nu} \right)^{1/2} (\epsilon \omega a)^2 \left[ K^2 I_0 + KM I_1 - KN J_1 \right]$$

where

$$\frac{1}{2} J_1 = 2\pi a^2 \int_0^{\pi/2} \left\{ \sin^3 \theta \frac{u(\theta)}{\sin \theta \cos \theta} \right\}.$$

$$\left\{ \left( \frac{\cos \theta}{x} + 1 \right)^{1/2} \left( \frac{\cos \theta}{x} - 1 \right)^{-1/2} - \left| \frac{\cos \theta}{x} - 1 \right|^{1/2} \left( \frac{\cos \theta}{x} + 1 \right)^{1/2} \right\} d\theta$$

The balance, A2.12 gives

$$\begin{aligned} & (- \text{ for } \theta \leq \theta_c \\ & + \text{ for } \theta \geq \theta_c) \end{aligned}$$

$$(M^2 + N^2)I_2 + KI_1M + KJ_1N = 0.$$

The in-phase and quadrature components  $(M, N)$  of the response lie on a circle passing through the origin. The centre is at

$$\left( -I_1/2I_2, -J_1/2I_2 \right)$$

and the radius is

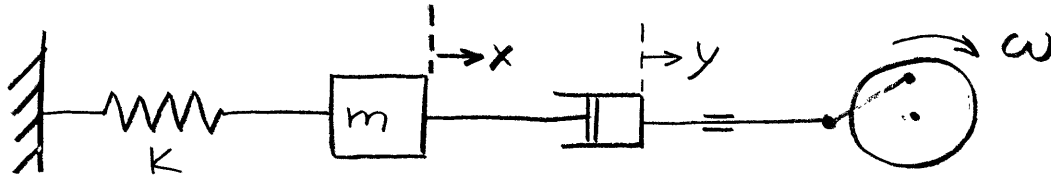
$$\sqrt{I_1^2 + J_1^2} / 2I_2.$$

The phase angle for the maximum response is

$$\phi_0 = \tan^{-1} (J_1 / I_1).$$

APPENDIX III. Superposition of Modes—a Mass-Spring Oscillator Analogy.

The rate at which the amplitude vector rotates around the response circle as a function of the frequency ratio  $\omega/2\Omega$  has not been found here. We consider, however, the following mechanical analogue, suggested by Toomre, which does have a known amplitude versus frequency dependence. A mass,  $m$ , is connected to a rigid support through a spring of spring constant  $K$ . The mass is vis-ously driven through a dashpot-crank arrangement shown below.



The net force on the mass equals its rate of change of momentum; we have

$$m\ddot{x} = -Kx - 2\alpha(\dot{x} - \dot{y})$$

where  $2\alpha$  is the dashpot damping coefficient.

Then

$$\ddot{x} + \frac{2\alpha}{m}\dot{x} + \frac{k}{m}x = \frac{2\alpha}{m}\dot{y} \quad \text{A3.1}$$

Let

$$\Omega_0^2 = \frac{k}{m} \quad ; \quad \frac{2\alpha}{m} = 2\epsilon \quad \text{and} \quad Q = \frac{\Omega_0}{2\epsilon}$$

The motion  $y$  is specified as

$$y = \text{Re}\{A e^{i\omega t}\}$$

and we seek solutions of the form

$$x = \operatorname{Re} \{ X_0 e^{i\omega t} \}$$

in equation A3.1.

We find

$$X_0 = \frac{i \frac{\omega}{\sigma_0} A}{Q \left[ 1 - \left( \frac{\omega}{\sigma_0} \right)^2 \right] + i \frac{\omega}{\sigma_0}}$$

from which

$$|X_0| = \frac{\frac{\omega}{\sigma_0} A}{\left[ Q^2 \left( 1 - \left( \frac{\omega}{\sigma_0} \right)^2 \right) + \left( \frac{\omega}{\sigma_0} \right)^2 \right]^{1/2}}$$

and

$$\tan \phi = Q \cdot \frac{1 - \left( \frac{\omega}{\sigma_0} \right)^2}{\frac{\omega}{\sigma_0}}$$

A3.2

where

$$\phi = \tan^{-1} \left( \operatorname{Im} \{ X_0 \} / \operatorname{Re} \{ X_0 \} \right)$$

At resonance,  $\omega = \sigma_0$  and  $|X_0| = A$ ; the maximum response of the mass is limited to the amplitude of the dashpot displacement.

From the identity

$$\cos^2 \phi = \frac{1}{1 + \tan^2 \phi}$$

we find from A3.2

$$|X_0| = A \cos \phi$$

and

$$\phi = \tan^{-1} \left[ Q \cdot \frac{1 - \left(\frac{\omega}{\omega_0}\right)^2}{\frac{\omega}{\omega_0}} \right].$$

APPENDIX IV. Variational Formulation of the Eigenvalue Problem.

We defined  $\Psi$  by the relations

$$U = \frac{1}{R} \frac{\partial \Psi}{\partial z} \quad ; \quad W = -\frac{1}{R} \frac{\partial \Psi}{\partial R} .$$

where  $U$  is the radial velocity ( $R$ ) and  $W$  is the vertical velocity ( $z$ ).

We found earlier that

$$R \frac{\partial}{\partial R} \left( \frac{1}{R} \frac{\partial \Psi}{\partial R} \right) - \lambda^2 \frac{\partial^2 \Psi}{\partial z^2} = 0 \quad \text{A4.1}$$

with the boundary conditions  $\Psi = \text{constant}$  around the boundaries, and, because of symmetry, along the lines  $R = z = 0$ .

Now we ask: is this equation the Euler Equation of some variational problem?

Try formulating the variational problem by multiplying both sides of this equation by  $\delta \Psi$ , the variation of  $\Psi$ . It will be useful to multiply through by  $1/R$  as well. Then

$$\left( \frac{1}{R} \Psi_R \right)_R \delta \Psi - \lambda^2 \frac{\Psi_{zz}}{R} \delta \Psi = 0 \quad \text{A4.2}$$

From the identity

$$\left( \frac{1}{R} \Psi_R \delta \Psi \right)_R = \left( \frac{1}{R} \Psi_R \right)_R \delta \Psi + \delta \left( \frac{\Psi_R^2}{2R} \right) ,$$

there follows

$$\left( \frac{1}{R} \Psi_R \right)_R \delta \Psi = -\delta \left( \frac{\Psi_R^2}{2R} \right) + \left( \frac{1}{R} \Psi_R \delta \Psi \right)_R \quad \text{A4.3}$$

and similarly

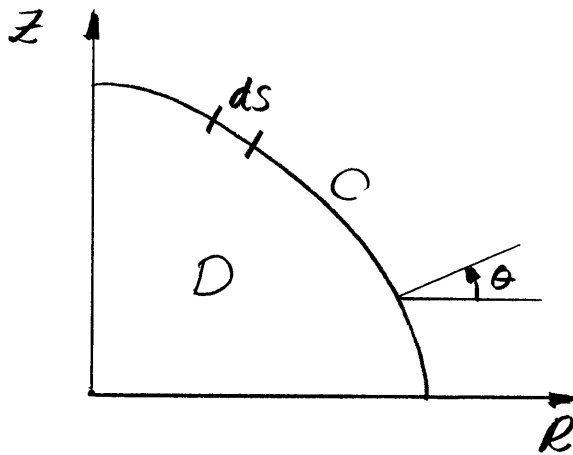
$$\left(\frac{1}{R} \psi_{zz}\right) \delta\psi = -\delta\left(\frac{\psi_z^2}{2R}\right) + \left(\frac{1}{R} \psi_z \delta\psi\right)_z \quad \text{A4.4}$$

Use the identities (3) and (4) in equation (2) to obtain

$$-\delta\left(\frac{\psi_R^2}{2R} - \lambda^2 \frac{\psi_z^2}{2R}\right) + \left(\frac{1}{R} \psi_R \delta\psi\right)_R - \lambda^2 \left(\frac{1}{R} \psi_z \delta\psi\right)_z = 0 \quad \dots \text{A4.5}$$

Now consider a region  $D$  in the  $R, z$  plane surrounded by a curve  $C$ . Integrate over the region  $D$ . The first term in the above equation becomes

$$-\delta \iint_D \left( \frac{\psi_R^2}{2R} - \lambda^2 \frac{\psi_z^2}{2R} \right) dR dz$$



The second term is

$$\iint_D \left(\frac{1}{R} \psi_R \delta\psi\right)_R dR dz = \int_C \frac{1}{R} \frac{\partial\psi}{\partial R} \cos\theta \delta\psi ds$$

$\psi$  is specified around C and  $\frac{\psi_R}{R} = -W$ ,

which is finite. Therefore there is no contribution from this integral.

Similarly

$$\iint_D \left( \frac{1}{R} \psi_z \delta\psi \right)_z dR dz = \int_C \frac{1}{R} \psi_z \sin\theta \delta\psi dS$$

vanishes in virtue of  $\psi$  being specified and  $u = \frac{1}{R} \frac{\partial\psi}{\partial z}$ , which remains finite.

Therefore, the variational problem is specified as

$$\delta \iint_D \frac{1}{2R} (\psi_R^2 - \lambda^2 \psi_z^2) dR dz = 0 \quad \text{A4.6}$$

with  $\psi = \text{constant}$  along the curve C. We now check that this variational problem leads to the correct Euler Equation. If

$$F = \frac{\psi_R^2}{2R} - \frac{\lambda^2 \psi_z^2}{2R}$$

then the Euler equation is

$$\frac{\partial}{\partial R} (F_{\psi_R}) + \frac{\partial}{\partial z} (F_{\psi_z}) = 0 \quad (\text{Hildebrand, 1961})$$

$$\text{Here, } F_{\psi_R} = \frac{\psi_R}{R} \quad ; \quad \frac{\partial}{\partial R} (F_{\psi_R}) = \frac{\partial}{\partial R} \left( \frac{1}{R} \psi_R \right) ;$$

$$F_{\psi_z} = -\frac{\lambda^2 \psi_z}{R} \quad ; \quad \frac{\partial}{\partial z} (F_{\psi_z}) = -\frac{\lambda^2}{R} \psi_{zz} .$$



The Euler equation is, here,

$$\frac{\partial}{\partial R} \left( \frac{1}{R} \frac{\partial \psi}{\partial R} \right) - \frac{\lambda^2}{R} \frac{\partial^2 \psi}{\partial z^2} = 0$$

or

$$R \frac{\partial}{\partial R} \left( \frac{1}{R} \psi_R \right) - \lambda^2 \psi_{zz} = 0$$

as given in equation (1).

The variational problem can also be given as

$$\iint_D \left( \frac{\partial}{\partial R} \left( \frac{1}{R} \psi_R \right) - \frac{\lambda^2}{R} \psi_{zz} \right) \delta \psi dR dz = 0 \quad \text{A4.7}$$

with  $\psi = \text{constant}$  along C, for approximation purposes.

The curve C of interest here is the one which bounds the fluid contained between concentric spheres and is closed by the lines  $R=z=0$ . A function which vanishes along this curve is

$$\psi_0(R, z) = R^2 z (1 - R^2 - z^2) \left( 1 - \frac{b/a}{R^2 + z^2} \right)$$

We shall seek the eigenvalues of the equation

$$R \frac{\partial}{\partial R} \left( \frac{1}{R} \psi_R \right) - \lambda^2 \frac{\partial^2 \psi}{\partial z^2} = 0$$

for the region between concentric spheres by applying the condition of the variational problem as given in A4.7, to a trial function

$$\psi(R, z) = \psi_0(R, z) \sum_{n,m} C_{nm} R^{2n} z^{2m}$$

which is constant along the boundary C of the Region D, between the concentric spheres. Since the constants  $C_{nm}^*$  are to be adjusted to satisfy A4.7, we have for the variation of  $\psi$ ,

$$\delta\psi = \psi_0(R, z) \sum_{n,m} \delta C_{nm} R^{2n} z^{2m}$$

The array  $C_{nm}$  is built up in the following triangular manner:

$$\begin{array}{cccc} C_{00} & C_{10} & C_{02} & C_{03} \\ C_{10} & C_{11} & C_{12} & \\ C_{20} & C_{21} & & \\ C_{30} & & & \end{array} \quad \swarrow$$

The first expansion contains one term  $C_{00}$ , the second three terms,  $C_{00}$ ,  $C_{10}$  and  $C_{01}$  and so on for 6, 10, 15 --- terms. This manner of escalation adds an additional factor of the form

$$(1 - A_z z^2 - A_e R^2)$$

to the corresponding product representation as given in Appendix I for the sphere. To avoid confusion in the indices of  $C_{nm}$  we adopt to convention

$$C_{nm} = C_k$$

where for each  $(n,m)$  combination there is a unique  $k$  which

---

\*This  $C_{nm}$  is not related to the  $C_{nm}$  of Appendix II.

simply represents the order in which the  $C_{nm}$  are taken for a particular expansion. For example, the correspondence could be  $(C_{00}, C_{10}, C_{01}, C_{20}, C_{11}, C_{02}, \dots)$  to  $(C_1, C_2, C_3, C_4, C_5, C_6, \dots)$   
 We then write

$$\psi_K(R, z) = \psi_0(R, z) C_K S_K(R^2, z^2)$$

$$\delta\psi_K(R, z) = \psi_0(R, z) \delta C_K S_K(R^2, z^2)$$

where  $S_K(R^2, z^2)$  is the polynomial factor  $R^{2n} z^{2m}$  for the particular choice of  $K$ . In the previous example

$$S_5(R^2, z^2) = R^2 z^2 .$$

The original function, for an expansion of  $N$  terms,

$$\psi(R, z) = \sum_{K=1}^N \psi_K(R, z)$$

and its variation

$$\delta\psi(R, z) = \sum_{K=1}^N \delta\psi_K(R, z)$$

are now put into A4.7.

If we let

$$A_{ij} = \iint_D \frac{\partial}{\partial R} \left( \frac{1}{R} \frac{\partial}{\partial R} (\psi_0 S_j) \right) \psi_0 S_i dR dz$$

and

$$B_{ij} = \iint_D \frac{1}{R} \frac{\partial^2}{\partial z^2} (\psi_0 S_j) \psi_0 S_i dR dz$$

Then equation A4.7 becomes

$$\begin{aligned} & [(A_{11} - \lambda^2 B_{11})C_1 + (A_{12} - \lambda^2 B_{12})C_2 + \dots + (A_{1N} - \lambda^2 B_{1N})C_N] \delta C_1 \\ & + [(A_{21} - \lambda^2 B_{21})C_1 + (A_{22} - \lambda^2 B_{22})C_2 + \dots + (A_{2N} - \lambda^2 B_{2N})C_N] \delta C_2 \\ & + \dots \\ & + [(A_{N1} - \lambda^2 B_{N1})C_1 + (A_{N2} - \lambda^2 B_{N2})C_2 + \dots + (A_{NN} - \lambda^2 B_{NN})C_N] \delta C_N \\ & = 0. \end{aligned}$$

Now since each of the  $\delta C$  are arbitrary, their coefficients must vanish individually and we have the array of linear equations in  $C$ ,

$$[\bar{A} - \lambda^2 \bar{B}] \bar{C} = 0.$$

where  $\bar{A} = \{A_{ij}\}$  ;  $\bar{B} = \{B_{ij}\}$  ,  $\bar{C} = \{C_{ij}\}$  .

For a non-trivial solution vector  $\bar{C}$  we require that the determinant of the coefficient matrix vanish,

$$|\bar{A} - \lambda^2 \bar{B}| = 0. \quad \text{A4.8}$$

For an expansion of  $N$  terms,  $\bar{A}$  and  $\bar{B}$  are  $N \times N$  arrays and the equation A4.8 has  $N$  roots in  $\lambda^2$ . The elements of the  $A, B$  arrays were calculated for  $N=1, 3, 6, 10, 15, 21$  terms for ratios  $b/a = 0.25, 0.35$  and  $0.51$ . Zeros of the determinant were found by locating changes in sign of the determinant for trial values of  $\lambda^2$ .

BIOGRAPHICAL NOTE

The author was born on 23 January 1941 in Toronto, Canada. He attended Ontario Secondary Schools and entered college in the Faculty of Applied Science and Engineering of the University of Toronto in September 1958. He graduated in May 1962 with the degree of Bachelor of Applied Science in Engineering Physics. In the fall of 1962 he enrolled at M.I.T. in the Department of Geology and Geophysics.

He is a member of the M.I.T. chapter of the Society of Sigma Xi.